African Journal of Engineering in Research and Innovation

AJERI Vol 1. No. 2. 2023

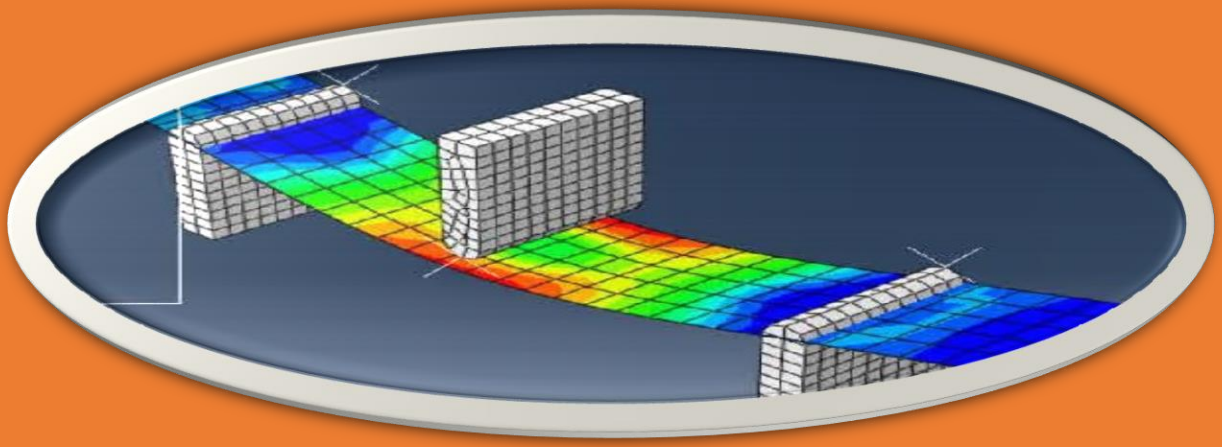

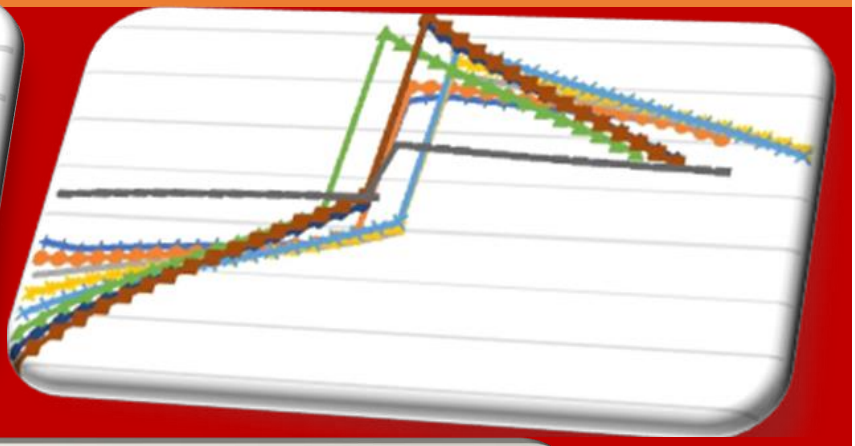

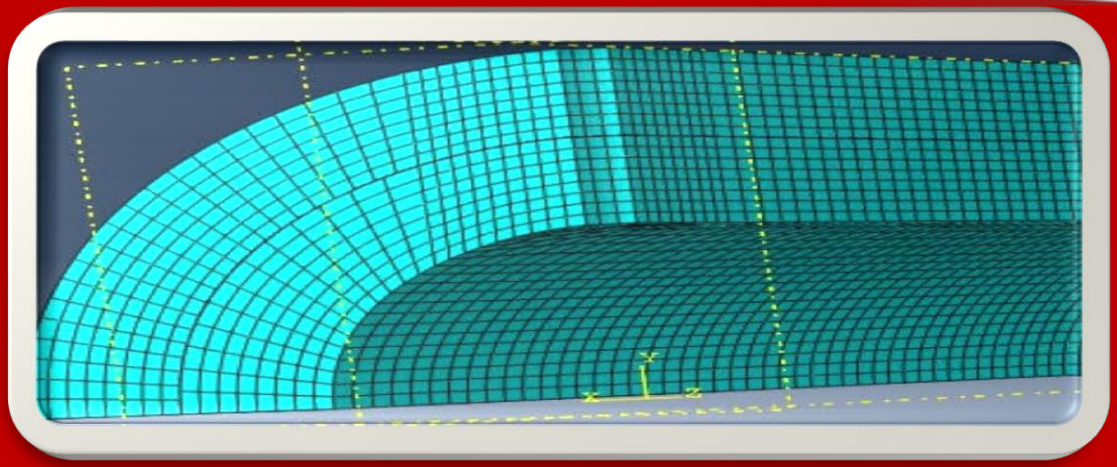

The Institution of Engineers of Kenya

ISSN: 2957- 7780

In partnership with

AJERI

African Journal of Engineering in Research and Innovation

ISSN: 2957- 7780 Volume 1. No 2. 2023

Published by:

The *Institution of Engineers of Kenya*

P.O Box 41346- 00100

City Square Nairobi Kenya

Tel: +254 (20) 2729326, 0721 729363, (020) 2716922

Email: editor@iekenya.org

Website: www.iekenya.org

IEK

African Journal of Engineering Research and Innovation (AJERI), is published by **The *Institution of Engineers of Kenya,*** IEK, as an international forum for publication of high-quality papers in all areas of Engineering

CONTENTS **Pages**

CHARACTERIZATION OF DIATOMACEOUS EARTH TO EVALUATE ITS POTENTIAL AS A RESOURCE FOR GEOPOLYMER CONCRETE DEVELOPMENT

Janet J. Kipsanai *[1], Sofiane Amziane. [2], Paul M. Wambua [3], Saul S. Namango [4]

*[1]*Research Scholar in Mechanical & Production Engineering, Moi University-Kenya*

[2]*Professor of Civil Engineering, Université Clermont Auvergne-France*

[3] *Professor of Materials Engineering, Technical University of Kenya*

[4]*Associate Professor of Chemical & Processing Engineering, Moi University-Kenya*

**Corresponding author: kipsanaij@yahoo.com*

Abstract

Researchers have become interested in cutting-edge geopolymer technology and the creation of geopolymer composites as a means of achieving sustainability in the production of concrete. In this study, the feasibility of using diatomaceous earth from Nakuru, Kenya, as a source for geopolymer concrete was evaluated. The chemical and physical analysis of diatomaceous earth were carried out using standard techniques. Thermogravimetric (TGA) and Differential Scanning Calorimetry (DSC) analyses were performed on the diatomite for thermal characterization. The Sodium silicate/Sodium hydroxide alkaline activated diatomite-based brick specimens were moulded, and their mechanical and physical features were determined using standard test procedures. The diatomaceous earth's chemical composition showed that silica (SiO_2) was the predominant component, with 88.12%. Calcium oxide (CaO) was 4.26% and alumina (Al_2O_3) was 4.25%. There were also trace levels of other oxides such as MgO, K_2O, TiO_2, MnO, Fe_2O_3, and P_20_5. The thermogravimetric analysis showed a loss on ignition of 5.68 % and that its softening point is higher than 950 °C. The particle size analysis and the Atterberg limit test showed that the diatomaceous earth from Nakuru, Kenya, is a cohesive and medium plastic silt, with an average particle size of less than 50.4 µm. The diatomite-based specimens had an average compressive strength of 22.98 MPa, a density of 1.38 g/cm^3 and water absorption of 9.32 %. The chemical composition suggests that it is comparable to Class F pozzolan. The mechanical, physical and durability performance falls within the acceptable limits provided in literature. This research showed that Kenyan diatomite can be successfully employed as a silica source in geopolymer formulations, providing hopeful approaches to utilizing and recycling the resource.

Keywords: Diatomaceous earth, characterization, pozzolan, geopolymer, sustainability

1. Introduction

One of the fundamental issues of our time is meeting the basic requirements of growing populations while ensuring the integrity of vital ecosystems, tackling climate change, and fostering economic productivity and social inclusiveness (Klopp & Petretta, 2017). Building and maintenance are by far the largest emitters of harmful gases like CO_2 and this eco-footprint will only grow with the large population growth expected by 2050 (Rostami et al., 2015). Compared to the industrial and transportation sectors, building and construction consumes more than 40% of world energy and emit about the same amount of CO_2 (Pramanik et al., 2021). As a result, the construction industry is constantly challenged to reduce its environmental impact by incorporating the major dimensions of sustainable development. The simplest way for designers to begin implementing sustainable ideas into construction projects, according to Aghdam et al. (2018), is to carefully select ecological building materials.

To achieve sustainability in the manufacturing of concrete, numerous researchers have developed an interest in cutting-edge geopolymer technology and geopolymer composite production. This is due to the fact that geopolymer production utilizes a variety of wastes as either supplementary cementitious materials (SCM) or precursors in the synthesis of geopolymers, at low temperatures and with minimal energy, while reducing the CO_2 footprint of the cement industry by up to 80% (Duxson et al., 2007; El-Dieb, 2016).

To reduce consumption and dependence on cement, the use of pozzolanic materials has been a major research focus in the field of cement and materials in recent years (Danso H & Adu S, 2019). The most popular geopolymer precursors (aluminosilicate sources) that have been extensively studied thus far include fly ash, ground granulated blast furnace slag, metakaolin, silica fume, and rice husk ash (Elahi et al., 2020; Nodehi & Taghvaee, 2022). Natural or spent diatomaceous earth, also called diatomite, has received very little attention, despite being regarded as one of the geopolymer system components by Payá et al. (2018) among other experts. According to Zahajská et al. (2020), massive accumulations of fossil diatom frustules have reportedly been discovered in numerous lakes located in silica-rich environments, particularly in volcanic and hydrothermally active areas, including Yellowstone Lake in the United States, Lake Myvatn in Iceland, Lake Challa in Tanzania and Kenya, among others. In kenya, Gevera et al. (2018) determined that diatomaceous earth sediments are found in the Nakuru-Elmenteita basin near Kariandusi.

The major end use for processed diatomite nowadays is as a filter aid; uses for filtration include the purification of beer, wine, and other alcoholic beverages, vegetable oil, syrup, pharmaceuticals, motor oil, and swimming pool water (Kogel & Society for Mining, 2006). According to U.S. Geological Survey (2022), around 55% of diatomite is used for filtration purposes. Consequently, spent diatomaceous earth (SDE) has become a significant source of industrial waste for industries like food processing and brewing (Galán-Arboledas et al., 2017; Mateo et al., 2017). For instance, approximately 378.1 million kilograms of SDE are produced annually by the brewing sector (Gong et al., 2019; Thiago et al., 2014). This used diatomite ends up in landfills or is applied to crops as organic fertilizer, both of which squander resources and harm the environment (Galán-Arboledas

et al., 2017). Additionally, the risk of leaching nitrogenous compounds present in the wasted diatomaceous earth could be increased by its use in agriculture. Moreover, due to the significant energy, labor, and cost requirements, the regeneration of SDE may not be a viable option. The use of SDE for more economically viable and environmentally sound applications, such as in geopolymer concrete technology is therefore of great importance.

The goal of this study is to evaluate the potential for using the diatomaceous earth resource to produce geopolymer concrete. A deeper comprehension of SDE's physical, chemical, mechanical, and pozzolanic characteristics is thus necessary for its adoption as a geopolymer resource.

2. Materials and methods

2.1 Materials

The raw diatomaceous Earth and alkaline activators were the main materials employed in this study. In this instance, sodium-based alkali activators were used, specifically a solution of sodium hydroxide and sodium silicate gel ($NaOH/Na_2SiO_3$), as advised by Cong et al. (2021). The materials were collected from sources within Kenya; specifically, diatomaceous earth was acquired from Nakuru, while sodium hydroxide and sodium silicate were bought from one of the outlet suppliers in Eldoret. Figure 1 presents a geological map of Nakuru county in Kenya which hosts the diatomaceous earth reserves (Gevera & Mouri, 2018).

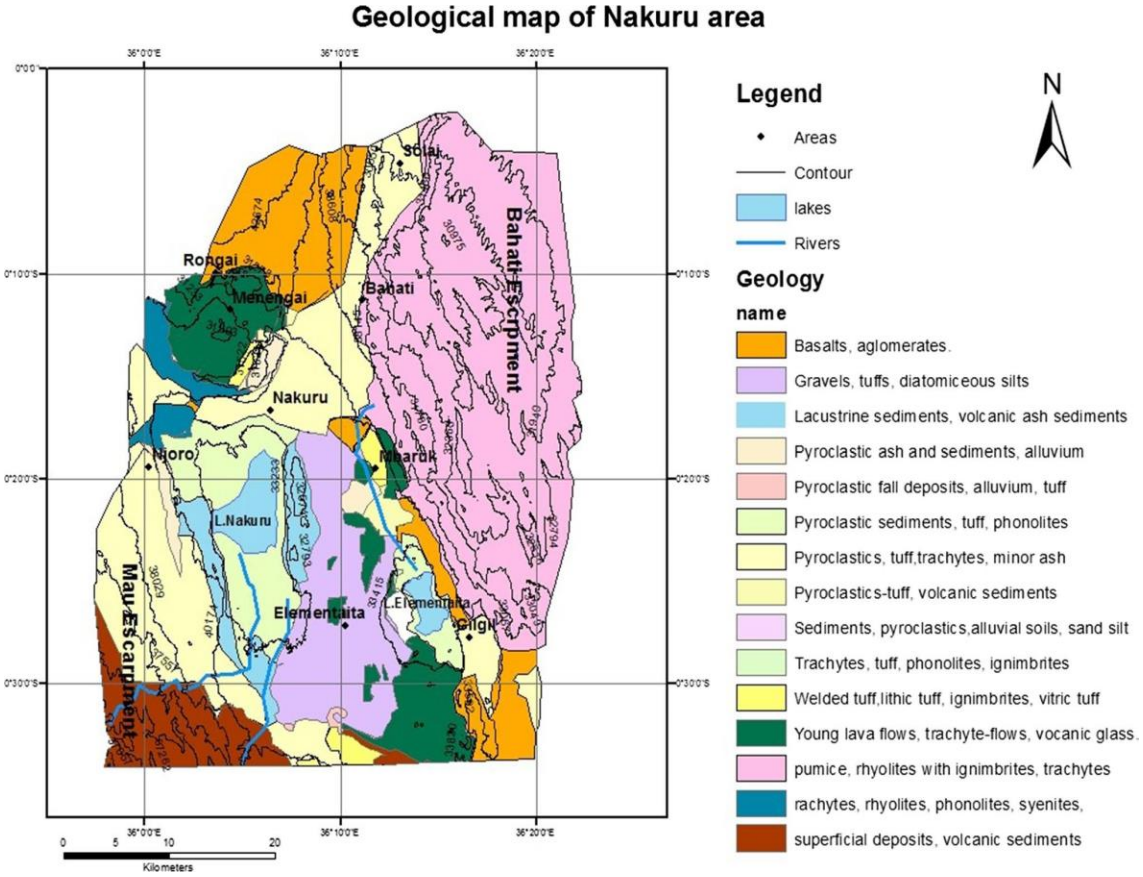

Figure 1. Geological map of Nakuru county-Kenya

2.2 Diatomaceous earth characterization

The diatomaceous earth had already been finely powdered when received. To get rid of all the moisture, it was oven dried at 110°C for 24 hours. The X-Ray fluorescence (XRF) apparatus was used to determine the chemical composition as per ASTM C114-10 (2010). To determine the crystallographic structure of the diatomite for further mineralogical analysis, the X-Ray diffraction (XRD) was employed. The Atterberg limits test, conducted in accordance with ASTM D4318-17 (2017), was used to determine the clayey nature of diatomaceous earth. Utilizing an LS 13 320 Laser Diffraction Particle Size Analyzer and following ASTM B822–17 (2017) guidelines, a particle size distribution analysis was performed. In line with ASTM-D854, (2010) and ASTM D 7348-13, (2013), respectively, the specific gravity and loss on ignition were carried out.

The thermal characterization of diatomaceous earth was performed through the use of Thermogravimetric (TGA) and Differential Scanning Calorimetry (DSC) analysis techniques according to ASTM E1131, (2015). A TGA-550 thermal analyser operating in a nitrogen atmosphere, flowing at a rate of 50 mL/min was employed. The weight change with respect to temperature was computed within a programmed temperature range of 25 °C to 950 °C at a rate of 10 °C/min. The DSC-Q200 machine was employed, operating in a static air environment between -50 °C and 450 °C at a rate of 10 °C/min.

2.3 Geopolymer sample preparation and performance evaluation

According to the insights provided by Mohammed et al. (2021) in their literature review, an alkaline activator consisting of a mixture of Sodium silicate ($Na2SiO_3$) gel and Sodium hydroxide (12M NaOH) solution was used to create the geopolymer specimens. Based on the findings of the literature review conducted by Zhang et al. (2020), the ratio of sodium silicate to sodium hydroxide was maintained at 2.5. 480 grams of NaOH was dissolved in 1000 ml of distilled water to create a 12M NaOH solution. The diatomite and the alkaline activator were mixed at a constant liquid-binder ratio of 0.7 following the design of experiment in Table 1. The geopolymer bricks were shaped in a mould of dimensions 160mm by 40mm by 40mm at a constant compaction pressure of 8MPa as suggested by Danso (2016). Upon demolding, the brick specimens were heat treated at 70°C in an oven for 24 hours and thereafter stored at room temperature for 28 days before performance evaluation.

Table 1: Design of experiment for chemical activation of diatomite

A: Diatomite % wt	B: Alkaline activator	
	Na_2SiO_3 %wt	NaOH %wt
100	50	20

The Mitutoyo ABSOLUTE Digimatic Vernier Caliper (500 series), which has a 0.01 mm precision, was used to measure the dimensions of the brick samples. The compressive strength of the bricks was determined using a 50kN-WP 310 universal Materials testing machine, following the ASTM C109/C109M (2007) standard. According to ASTM-C642, (2013), the bulk density was determined. The water absorption experiment was conducted following ASTM C373-14, (1999).

Compressive strength, density and water absorption experimental tests were carried out since according to Teixeira et al. (2020), compressive strength and durability tests are regarded as key indicators of the viability of masonry.

3. Results and discussion

3.1 Diatomaceous earth characterization

i. Chemical and physical analysis

The diatomaceous earth (DE) chemical analysis results are shown in Table 2.

Table 2: Chemical analysis results for diatomaceous earth

Specimen type	**Chemical content (%)**								
	SiO_2	**Al_2O_3**	**CaO**	**MgO**	**K_2O**	**TiO_2**	**MnO**	**Fe_2O_3**	**P_20_5**
Diatomite (Raw)	88.120	4.254	4.257	0.861	0.673	0.130	0.02	1.528	0.073

The findings of the chemical analysis of DE show that the tested material is an acidic rock with a dominant proportion of SiO_2 (88.12%) and relatively low contents of Al_2O_3 (4.25%), CaO (4.26%), and Fe_2O_3 (1.53%), with the content of each of the remaining oxides being below 1%. According to ASTM C618 (2014), the diatomite could be considered as a Class F normal type of pozzolan or a silicate glass material since its total content of SiO_2, Fe_2O_3, and Al_2O_3 was beyond 70% by weight with less than 10% CaO content. Nyale et al. (2014) clarified that a geopolymer binder is considered siliceous when the three key constituents, SiO_2, Al_2O_3, and Fe_2O_3, total up to 70% or when their total and the reactive calcium oxide is less than 10%. The diatomite's low CaO level is proof that it can be used as a geopolymer precursor. According to Okeyinka et al. (2019), low-calcium binders are best for creating geopolymers because excessive calcium concentrations can slow down the polymerization-setting rate.

This indicates that the diatomite under study is an acidic rock belonging to the opal A + CT category, as described by Stefanou et al. (2022). The diatomite's alumina (Al_2O_3) content revealed that it wasn't clayey because it was lower than the 14–16% range suggested by the literature (Chen et al., 2020; Fragoulis et al., 2004; Stefanou et al., 2022; Yilmaz & Ediz, 2008). There were also trace levels of other oxides such as MgO, K_2O, TiO_2, MnO, Fe_2O_3, and P_20_5.

The XRD analysis (Figure 2) showed that cristobalite was the predominant mineral in the Kenyan sampled diatomaceous earth. With reference to the classification done by Ejigu et al. (2022), the observed diffraction peaks are typical peaks for paracrystalline silica polymorph opal-CT derived from the volcanic environment.

The strongest reflection peak is at about 21.5°, with weaker peaks at around 29°, 32°, 36°, 45°, 57°, and 65°. The resulting diffraction peaks show the presence of α-cristobalite together with variable degrees of stacking disorder, which causes maxima that are linked to tridymite.

The X-ray diffractometry (XRD) mineralogical finding strongly supported Kogel & Society for Mining (2006) and hypothesis that the Kenyan Rift Valley hosts diatomaceous earth deposits which appear to be of lacustrine origin (from lacustrine diatomite diagenesis) pre-dating one or more episodes of faulting and vulcanicity.

The XRD results were also in agreement with the XRF chemical analysis output which showed that the silica (SiO_2) was the predominant chemical compound with a percentage of 88%.

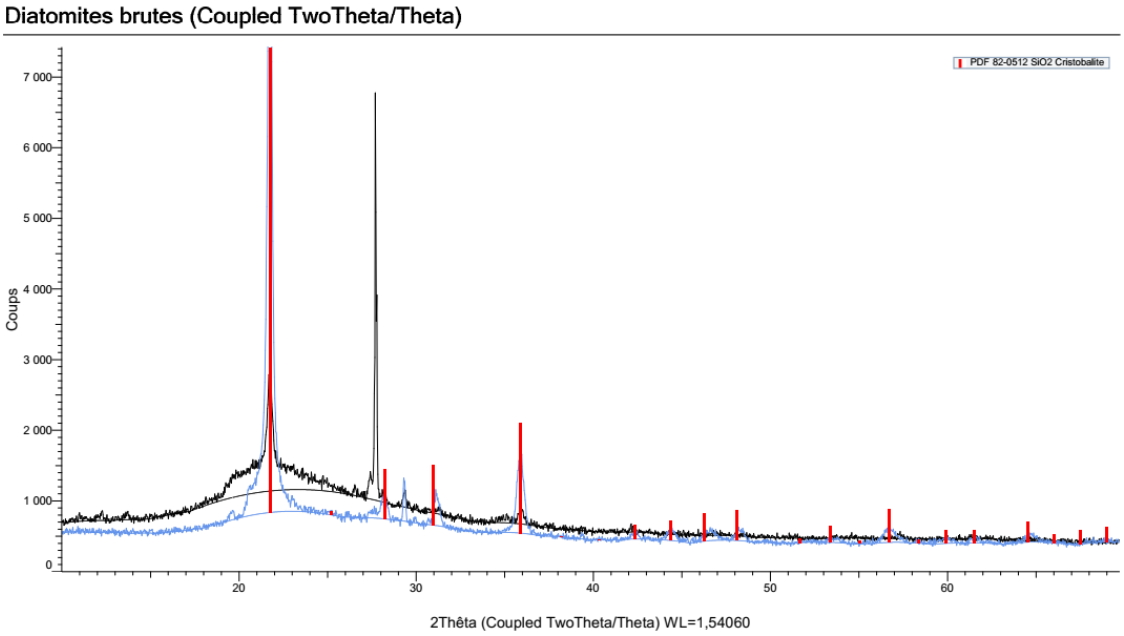

Figure 2. XRD result for diatomaceous earth.

The physical characteristics of the diatomaceous earth used in this study are shown in Table 3.

Table 3: Physical Analysis of diatomaceous earth

Specimen type	Physical property			
	Permeability (mD)	Porosity (%)	Specific gravity	Bulk density (g/cm^3)
Diatomite (Raw)	2.3	40	2.1	1.4

The permeability of the diatomite was determined to be 2.3 mD and the porosity was 40%. The values obtained were within the ranges of 0.1-10 mD for permeability and 35-65% for porosity as provided by Reka et al. (2021). The specific gravity value falls within the acceptable range of 1-2.6 for organic soils as stated in the literature by Roy & Kumar Bhalla (2017).

ii. TGA-DSC thermal characterization of diatomaceous earth

Regarding the diatomite TGA analysis depicted in Figure 3, there was a significant mass loss which may have been caused by the release of both free and bound diatomite as well as any organic stuff that may have been present.

A small weight loss after 200 °C can be attributed to the dehydroxylation of OH-groups and the release of structural water from its impurities and amorphous silica structure to form the amorphous metakaolin, as explained by Ibrahim & Selim (2012) and illustrated by the below chemical reaction equation.

$$Al_2O_3.\ 2SiO_2\ .2H_2O \xrightarrow{Heat} Al_2O_3.\ 2SiO_2 + 2H_2O.$$

The weight loss starts to stabilize as soon as the temperature hits 800 °C, signifying the complete dehydration of the diatomite structure and the emergence of a new silicate substance. The total weight loss (loss on ignition) for the diatomite at 950 °C was 5.682 %. This resulting loss on ignition (LOI) value was still below the maximum value of 6% allowed by ASTM.C618 (2014).

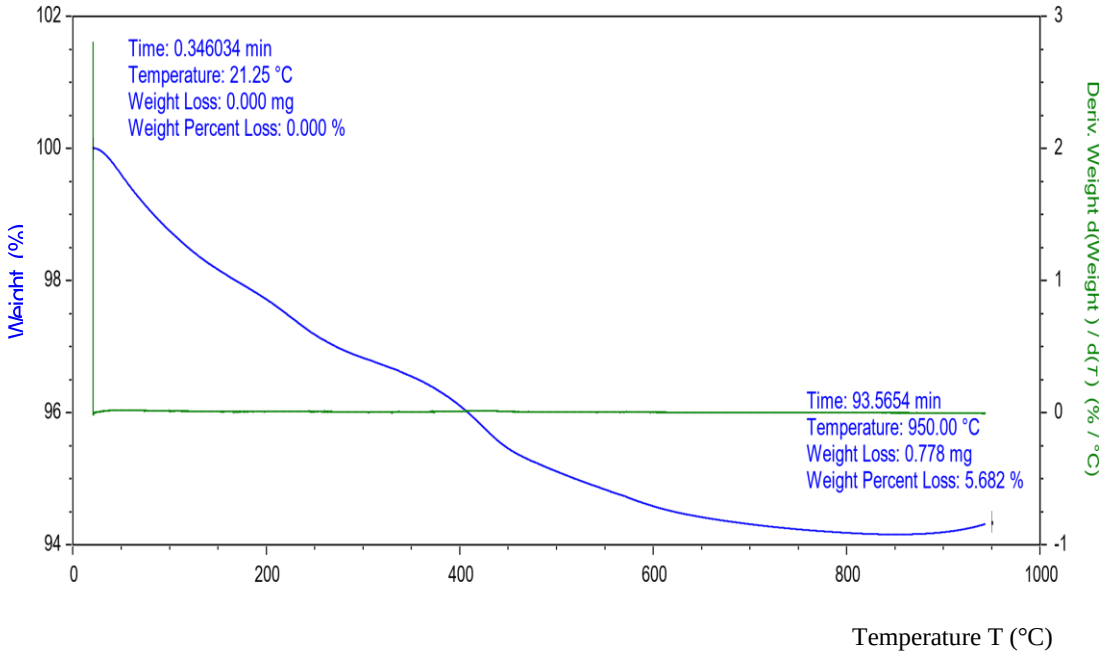

Figure 3. Weight loss analysis of raw diatomite

The DSC thermograms for the diatomite shown in Figure 4 revealed endothermic peaks between 120 °C and 280 °C, which are caused by the dehydration process (water evaporation), as a result of diatomite's high water absorption capacity. These peaks are the consequence of the separation of the opal component and the water that was bound to the diatomite particles.

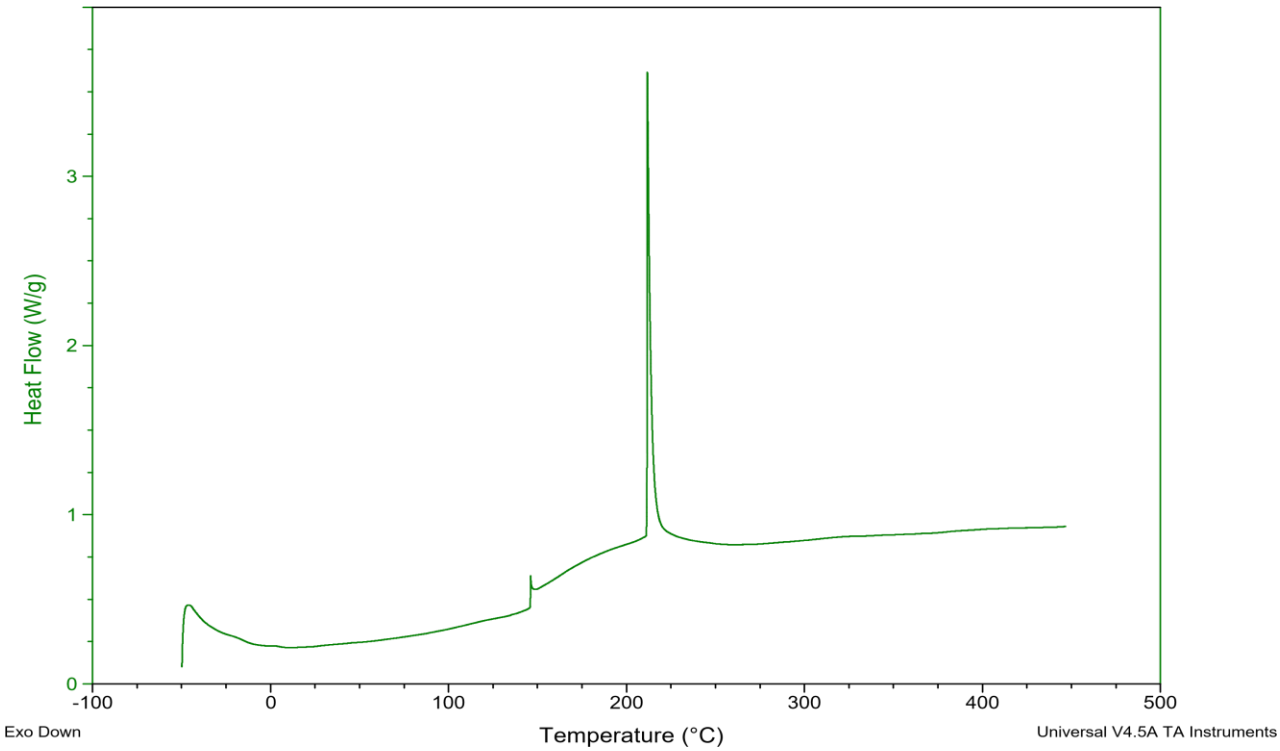

Figure 4. DSC analysis for raw diatomite

It is evident from the TGA experiment that diatomite is a thermally stable raw material and that its melting temperature is greater than 950 °C.

iii. Analysis of diatomaceous earth particle size

The diatomite particle size distribution as obtained from the laser particle analyzer was Dv (10): 7.58 µm, Dv (50): 23 µm, and Dv (90) 50.4 µm. Relating to Osborne's (2013) analysis, the diatomite was found to be more similar to cement, in terms of particle size, since about 90% of its particles were smaller than 50.4 µm.

The particle size distribution of diatomaceous earth depicted in Figure 5 shows that the diatomite is a fine-grained earth material hence suitable for use as geopolymer precursor following the argument by Makusa (2012) that fine-grained granular materials are the easiest to stabilize due to their large surface area to their particle diameter.

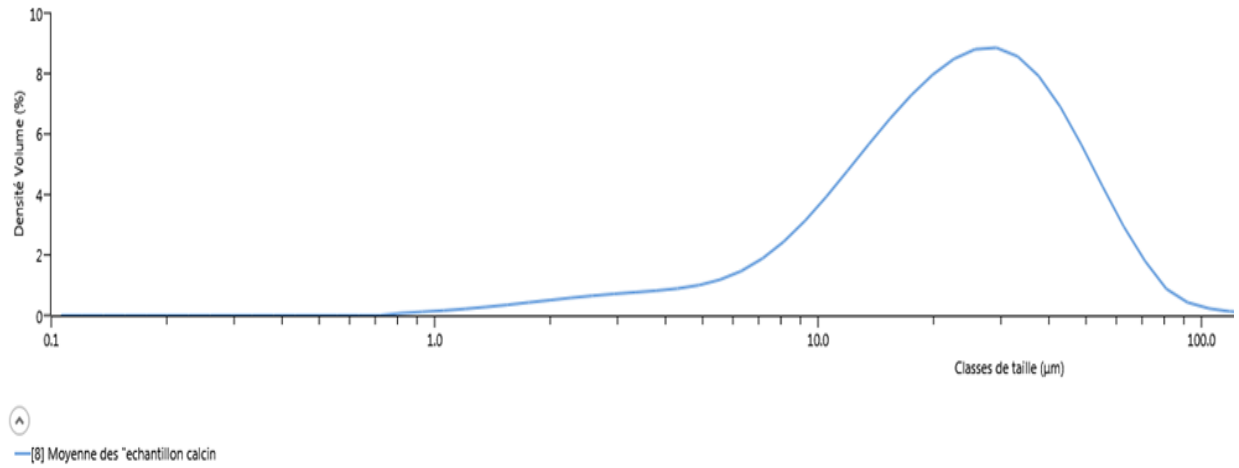

Figure 5. Raw diatomite particle size distribution

iv. The Atterberg limits test

The plastic limit (PL), liquid limit (LL), and plasticity index (PI) were obtained using the Atterberg limit test as described by ASTM D4318-17 (2017). Average values resulting from three (3) trials are presented in Table 4.

Table 4: Atterberg Limits Data

Item details	Raw Diatomite (grams)
Mass of empty can	20
Mass of can and wet soil	35.14
Mass of can and dry soil	30.79
Mass of dry soil	10.79
Mass of pore water	4.35
Water content, w%	40.34
No. of drops (N)	233
Plastic Limit (PL)	40.34
Liquid Limit (LL)	53
Plasticity Index (PI)	12.66

According to the data from the Atterberg limits experiment, the plasticity index for the diatomite was around 13. As suggested by Hall et al. (2012), diatomaceous earth employed in this study generally appears to be favourably good for usage as an earth construction material as its PI, is less than 16%.

Comparing the Atterbergs categorization described by Roy and Kumar Bhalla (2017) with the findings of this study reveals that raw diatomite is a cohesive and medium plastic silt clay.

3.2 Geopolymer performance evaluation

The results for the performance evaluation for the $NaOH/Na_2SiO_3$-activated diatomite geopolymer brick are presented in Table 5.

Table 5: Performance properties of $NaOH/Na_2SiO_3$ activated diatomite

	28^{th}-day properties		
	Compressive Strength (MPa)	Density (g/cm^3)	Water Absorption (%)
Average	**22.98**	**1.38**	**9.32**
min.	21.74	1.33	8.54
max.	24.33	1.43	10.00
std (+)	1.22	0.05	0.78
std (-)	1.36	0.05	0.68

A bar graph of the performance characteristics obtained for the created geopolymer concrete specimens is shown in Figure 6.

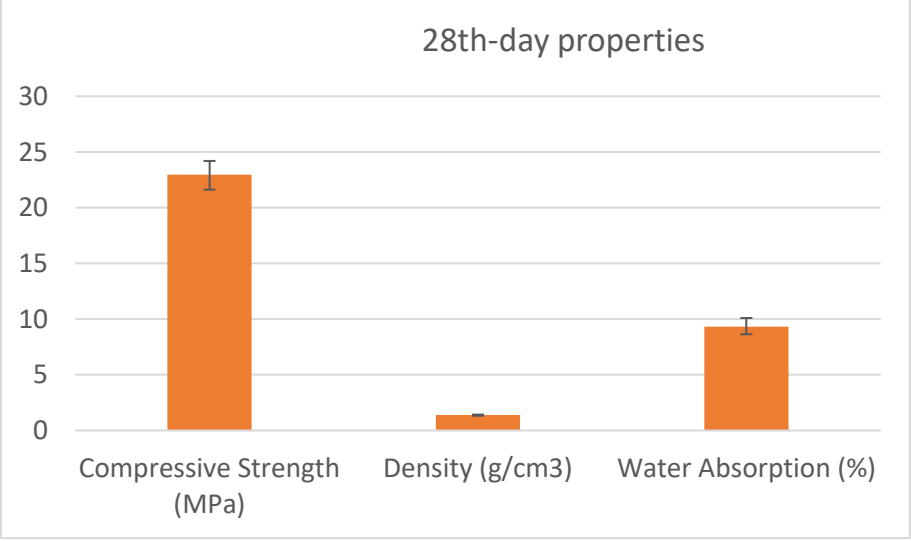

Figure 6: Performance properties of $NaOH/Na_2SiO_3$ activated diatomite

The developed diatomite-based geopolymer's average 28-day compressive strength of 22.98 MPa falls within the permitted range of 8-115 MPa for light, normal, and heavyweight concrete as specified by European Standard EN 206-1 (EN 206-1, 2000).

The $NaOH/Na_2SiO_3$ activated geopolymers had an average density of 1.38 g/cm^3. The density values of the $NaOH/Na_2SiO_3$ activated geopolymer were found to be within the permitted range of 1.2-2 g/cm^3 for lightweight concrete, according to Day et al. (2013). The low relative density and high porosity of diatomaceous earth could have contributed to the development of lightweight specimens. Based on the classification by TS EN 206 (2016), which defines lightweight concrete as having density of between 800 kg/m^3 and 2000 kg/m^3, the produced geopolymer concrete can be categorically referred to as lightweight.

The water absorption for the diatomite-based geopolymer specimens was satisfactory based on both the Australian and Malaysian standards as provided by Ahmad et al. (2017). This is because the average water absorption value attained was less than the preset maximum limit of 20%.

4. Conclusion

This research sought to evaluate the viability of using diatomaceous earth from Nakuru, Kenya, as a resource for geopolymer concrete. It was determined that the diatomite under examination is an acidic rock falling within the opal CT category, according to the chemical composition, which revealed silica (SiO_2) to be the major component, accounting for 88.12 percent of the sample. Therefore, the siliceous nature of Kenyan diatomaceous earth is of a rather high grade, comparable to a silicate glass material or a typical Class F kind of pozzolan. The Kenyan diatomaceous earth samples tested may have originated as biogenic silica opal-A before dissolving or re-forming as opal-CT as a result of thermal alteration of the rock caused by the high heat flow rates created in the rift zones by the penetration of dacite sills as a mechanism of the volcano-sedimentary succession.

The Atterberg limit examination and particle size analysis revealed that diatomaceous earth is a fine, cohesive, and medium silt material. Additionally, the diatomite is a material that is thermally stable and has a melting point greater than 950 °C, according to the TGA experiment. Moreover, significant diatomite loss on ignition (LOI), as determined by TGA, revealed that the material is porous, with low thermal conductivity and high thermal insulation capacity.

Importantly, the Kenyan diatomaceous earth can be successfully employed as a silica source in geopolymer concrete formulations, fostering the production of sustainable concrete.

Acknowledgments

The authors acknowledge the facilitation of research resources by Moi University and Université Clermont Auvergne, France.

Funding

This research did not receive any specific grant from funding agencies in the public, commercial, or not-for-profit sectors.

References

Aghdam, K. A., Rad, A. F., Shakeri, H., & Sardroud, J. M. (2018). Approaching green buildings using eco-efficient construction materials : a review of the state-of-the-art. *Journal of Construction Engineering and Project Management*, *8*(3), 1–23.

Ahmad, S., Iqbal, Y., & Muhammad, R. (2017). Effects of coal and wheat husk additives on the physical, thermal and mechanical properties of clay bricks. *Boletin de La Sociedad Espanola de Ceramica y Vidrio*, *56*(3), 131–138. https://doi.org/10.1016/j.bsecv.2017.02.001

ASTM. (1999). ASTM C373-14 Standard Test Method for Water Absorption, Bulk Density, Apparent Porosity, and Apparent Specific Gravity of Fired Whiteware Products. *Astm C373-88*, *88*(Reapproved).

ASTM. (2014). Astm C618. *Annual Book of ASTM Standards*, *C*.

ASTM B822-17. (2017). Standard test method for particle size distribution of metal powders and related compounds by light scattering. *ASTM International, West Conshohocken, PA*.

ASTM C109/C109M, A. (2007). Compressive Strength of Hydraulic Cement Mortars (Using 2-in . or [50-mm] Cube Specimens) 1. *American Society for Testing and Material*.

ASTM D 7348-13. (2013). Standard Test Methods for Loss on Ignition (LOI) of Solid Combustion Residues. *ASTM International*, *i*.

ASTM E1131. (2015). Standard Test Method for Compositional Analysis by Thermogravimetry. *ASTM International*, *08*(Reapproved 2014).

ASTM International. (2010). ASTM C114-10 - Standard Test Methods for Chemical Analysis of Hydraulic Cement. *Book of Standards Volume: 04.01*.

ASTM International. (2017). ASTM D4318-17. *Standard Test Methods for Liquid Limit, Plastic Limit, and Plasticity Index of Soils*.

ASTM-C642. (2013). ASTM C642-13 Standard Test Method for Density, Absorption, and Voids in Hardened Concrete. *Annual Book of ASTM Standards*, *3*.

ASTM-D854. (2010). Standard Test for Specific Gravity of Soil Solids by Water Pycnometer. In *ASTM International* (Issue March).

Chen, F., Miao, Y., Ma, L., Zhan, F., Wang, W., Chen, N., & Xie, Q. (2020). Optimization of pore structure of a clayey diatomite. In *Particulate Science and Technology* (Vol. 38, Issue 5). https://doi.org/10.1080/02726351.2019.1567635

Cong, P., & Cheng, Y. (2021). Advances in geopolymer materials: A comprehensive review. *Journal of Traffic and Transportation Engineering (English Edition)*, *8*(3), 283–314. https://doi.org/10.1016/j.jtte.2021.03.004

Danso, H. (2016). Influence of Compacting Rate on the Properties of Compressed Earth Blocks. *Advances in Materials Science and Engineering*, *2016*. https://doi.org/10.1155/2016/8780368

Danso H, & Adu S. (2019). Characterization of Compressed Earth Blocks Stabilized with Clay Pozzolana. *Journal of Civil & Environmental Engineering*, *9*(1), 1–6. https://doi.org/10.4172/2165-784X.1000331

Day, K. W., Aldred, J., & Hudson, B. (2013). Concrete mix design, quality control and specification, fourth edition. In *Concrete Mix Design, Quality Control and Specification, Fourth Edition*. https://doi.org/10.1201/b15624

Duxson, P., Provis, J. L., Lukey, G. C., & van Deventer, J. S. J. (2007). The role of inorganic polymer technology in the development of "green concrete." *Cement and Concrete Research*, *37*(12). https://doi.org/10.1016/j.cemconres.2007.08.018

Ejigu, A. A., Ketemu, D. G., Endalew, S. A., & Assen, W. Y. (2022). Characterization of Natural Precious Opal Using Modern Spectroscopic Techniques in Ethiopia: The Case from Delanta, South Wollo. *Journal of Spectroscopy*, *2022*. https://doi.org/10.1155/2022/3194151

Elahi, M. M. A., Hossain, M. M., Karim, M. R., Zain, M. F. M., & Shearer, C. (2020). A review on alkali-activated binders: Materials composition and fresh properties of concrete. *Construction and Building Materials*, *260*(November). https://doi.org/10.1016/j.conbuildmat.2020.119788

El-Dieb, A. S. (2016). Cementless concrete for sustainable construction. *MOJ Civil Engineering*, *1*(2). https://doi.org/10.15406/mojce.2016.01.00008

EN 206-1. (2000). *En 206-1*. Performance-Based Specifications and Control of Concrete Durability. Concrete. Part 1, Specification, Performance, Production and Conformity.

Fragoulis, D., Stamatakis, M. G., Chaniotakis, E., & Columbus, G. (2004). Characterization of lightweight aggregates produced with clayey diatomite rocks originating from Greece. *Materials Characterization*, *53*(2–4), 307–316. https://doi.org/10.1016/j.matchar.2004.05.004

Galán-Arboledas, R. J., Cotes-Palomino, M. T., Bueno, S., & Martínez-García, C. (2017). Evaluation of spent diatomite incorporation in clay based materials for lightweight bricks processing. *Construction and Building Materials*, *144*, 327–337. https://doi.org/10.1016/j.conbuildmat.2017.03.202

Gevera, P., & Mouri, H. (2018). Natural occurrence of potentially harmful fluoride contamination in groundwater: an example from Nakuru County, the Kenyan Rift Valley. *Environmental Earth Sciences*, *77*(10). https://doi.org/10.1007/s12665-018-7466-7

Gong, X., Tian, W., Wang, L., Bai, J., Qiao, K., & Zhao, J. (2019). Biological regeneration of brewery spent diatomite and its reuse in basic dye and chromium (III) ions removal. *Process Safety and Environmental Protection*, *128*. https://doi.org/10.1016/j.psep.2019.05.024

Hall, M. R., Najim, K. B., & Keikhaei Dehdezi, P. (2012). Soil stabilisation and earth construction: Materials, properties and techniques. In *Modern Earth Buildings: Materials, Engineering, Constructions and Applications*. https://doi.org/10.1533/9780857096166.2.222

Ibrahim, S. S., & Selim, A. Q. (2012). Heat treatment of natural diatomite. *Physicochemical Problems of Mineral Processing*, *48*(2), 413–424. https://doi.org/10.5277/ppmp120208

Klopp, J. M., & Petretta, D. L. (2017). The urban sustainable development goal: Indicators, complexity and the politics of measuring cities. *Cities*, *63*. https://doi.org/10.1016/j.cities.2016.12.019

Kogel, J. E., & Society for Mining, M. (2006). *Industrial minerals & rocks : commodities, markets, and uses.* Society for Mining, Metallurgy, and Exploration.

Makusa, G. P. (2012). Soil Stabilization Methods and Materials in Engineering Practice. *J0urnal*, *1*, 1–35.

Mateo, S., Cuevas, M., la Rubia, M. D., & Eliche-Quesada, D. (2017). Preliminary study of the use of spent diatomaceous earth from the brewing industry in clay matrix bricks. *Advances in Applied Ceramics*, *116*(2), 77–84. https://doi.org/10.1080/17436753.2016.1221019

Mohammed, A. A., Ahmed, H. U., & Mosavi, A. (2021). Survey of mechanical properties of geopolymer concrete: A comprehensive review and data analysis. In *Materials* (Vol. 14, Issue 16). https://doi.org/10.3390/ma14164690

Nodehi, M., & Taghvaee, V. M. (2022). Alkali-Activated Materials and Geopolymer: a Review of Common Precursors and Activators Addressing Circular Economy. *Circular Economy and Sustainability*, *2*(1). https://doi.org/10.1007/s43615-021-00029-w

Nyale, S. M., Eze, C. P., Akinyeye, R. O., Gitari, W. M., Akinyemi, S. A., Fatoba, O. O., & Petrik, L. F. (2014). The leaching behaviour and geochemical fractionation of trace elements in hydraulically disposed weathered coal fly ash. *Journal of Environmental Science and Health - Part A Toxic/Hazardous Substances and Environmental Engineering*, *49*(2). https://doi.org/10.1080/10934529.2013.838929

Okeyinka, O. M., Oloke, D. A., Adebisi, W. A., & Ayininuola, G. M. (2019). Investigation into the applicability of brewery sludge residue-ash as a base material for geopolymer concrete. *Construction and Building Materials*, *223*. https://doi.org/10.1016/j.conbuildmat.2019.06.214

Osborne, D. (2013). The Coal Handbook: Towards Cleaner Production. In *The Coal Handbook: Towards Cleaner Production* (Vol. 2). https://doi.org/10.1533/9781782421177

Payá, J., Agrela, F., Rosales, J., Morales, M. M., & Borrachero, M. V. (2018). Application of alkali-activated industrial waste. In *New Trends in Eco-efficient and Recycled Concrete*. https://doi.org/10.1016/B978-0-08-102480-5.00013-0

Pramanik, P. K. D., Mukherjee, B., Pal, S., Pal, T., & Singh, S. P. (2021). Green smart building: Requisites, architecture, challenges, and use cases. In *Research Anthology on Environmental and Societal Well-Being Considerations in Buildings and Architecture* (Issue January). https://doi.org/10.4018/978-1-7998-9032-4.ch002

Reka, A. A., Pavlovski, B., Fazlija, E., Berisha, A., & Pacarizi, M. (2021). *Diatomaceous Earth : Characterization , thermal modi fi cation , and application*. 451–461.

Rostami, R., Khoshnava, S. M., Rostami, R., & Lamit, H. (2015). Green and sustainability policy, practice and management in construction sector, a case study of Malaysia. *Research Journal of Applied Sciences, Engineering and Technology*, *9*(3). https://doi.org/10.19026/rjaset.9.1393

Roy, S., & Kumar Bhalla, S. (2017). Role of Geotechnical Properties of Soil on Civil Engineering Structures. *Resources and Environment*, *7*(4).

Stefanou, E., Kantiranis, N., Chatzicharalambous, K., Mytiglaki, C., Stamatakis, M., & Georgiadis, G. (2022). Diatomaceous Silica in Environmental Applications: A Case Study from the Lacustrine Deposit of Limnos Island, Aegean Sea, Greece. *Minerals*, *12*(5). https://doi.org/10.3390/min12050523

Teixeira, E. R., Machado, G., De Adilson, P., Guarnier, C., Fernandes, J., Silva, S. M., & Mateus, R. (2020). Mechanical and thermal performance characterisation of compressed earth blocks. *Energies*, *13*(11). https://doi.org/10.3390/en13112978

Thiago, R. dos S. M., Pedro, P. M. de M., & Eliana, F. C. S. (2014). Solid wastes in brewing process: A review. *Journal of Brewing and Distilling*, *5*(1). https://doi.org/10.5897/jbd2014.0043

TS EN 206. (2016). EN 206:2013 Concrete Concrete - Specification, performance, production and conformity ©. In *National Standards Authority of Ireland* (Issue May).

U.S. Geological Survey. (2022). Mineral commodity summaries January 2022. *U.S. Geological Survey*, *703*.

Yilmaz, B., & Ediz, N. (2008). The use of raw and calcined diatomite in cement production. *Cement and Concrete Composites*, *30*(3). https://doi.org/10.1016/j.cemconcomp.2007.08.003

Zahajská, P., Opfergelt, S., Fritz, S. C., Stadmark, J., & Conley, D. J. (2020). What is diatomite? In *Quaternary Research (United States)* (Vol. 96, pp. 48–52). Cambridge University Press. https://doi.org/10.1017/qua.2020.14

Zhang, P., Wang, K., Li, Q., Wang, J., & Ling, Y. (2020). Fabrication and engineering properties of concretes based on geopolymers/alkali-activated binders - A review. *Journal of Cleaner Production*, *258*. https://doi.org/10.1016/j.jclepro.2020.120896

BEHAVIOUR OF SHRINKAGE PRESSURE ON THICK COMPOUND CYLINDER WITH A CROSS BORE

Naftali Kiplagat[1], Leonard Masu[2], and Patrick Nziu[3]

[1] Moi University, School of Engineering, Department of Manufacturing Industrial & Textile Engineering, Eldoret, P. O. Box 3900 Eldoret, KENYA. ORCID: 0000-0003-1203-645X

[2] Technical University of Kenya, Faculty of Engineering and the Built Environment, School of Mechanical and Manufacturing Engineering, Department of Mechanical and Mechatronic Engineering, Haile Selassie Avenue, P.O. Box 52428, Nairobi, 00200, ORCID: 0000-0002-8544-6321

[3] Moi University, School of Engineering, Department of Manufacturing Industrial & Textile Engineering, Eldoret, P. O. Box 3900 Eldoret, KENYA. ORCID: 0000-0002-5899-0700

Abstract

Thick compound cylinders are usually manufactured when two or more cylinders of different diameters with some interferences are shrunk into each other. Therefore, this shrinking process generates residual stress distribution in the walls of the compound cylinders and subsequently improves the performance of the cylinder against the working pressure. The openings, commonly referred to as cross bores, are usually drilled into the wall of the plain thick cylinder These openings are used to provide for openings that are needed to fit instrumentation accessories for essential operations, however, these openings create points of stress concentrations. The effects of shrinkage pressure on hoop stresses and Stress Concentration Factor (SCF) on a cross bored thick-walled compound cylinder were studied to determine the optimal stress conditions. Finite Element Analysis (FEA) modeling software, Abaqus version 2019, was used to generate numerical solutions. A total of 11 different part models were created and analyzed in this work. The generated FEA results from these models were validated using analytical solutions developed from Lame's theory. Further, it was observed that shrinkage pressure affects hoop stress distribution along the transverse edge of a radial circular cross bore on a thick-walled compound cylinder. The analyses of the effects of shrinkage pressure ranging from 4.4733 to 223.662 MPa on SCF, established that a shrinkage pressure of 89.464 MPa generated the minimum SCF magnitude of 3.01 which was then considered optimum.

Keywords: Hoop Stress, Shrinkage Pressure, Stress Concentration Factors, High-Pressure Vessels, Compound cylinders, Finite Element Analysis.

1. Introduction

Tanks, vessels, and, pipelines that carry, store, or receive fluids are referred to as pressure vessels (Khobragade and Hiwase, 2017). These vessels can also be closed containers that are designed in such a way that the vessels can hold fluids which can be gases or liquids with pressure significantly different from atmospheric pressure (Kadam *et al.*, 2018). During the design of pressure vessels, various shapes can be adopted and these shapes can be either cylindrical or spherical (Thattil and Pany, 2017). Besides, cylindrical pressure vessels can be classified according to their thicknesses which may either be thin or thick-walled (Bahoum *et al.*, 2017). Therefore, cylinders are considered to be thick-walled if the internal pressure exerted by the fluids is greater than $1/6^{th}$ of the permissible stress or mainly if the wall thickness is more than $1/10^{th}$ of its internal radius (Phalguna, 2017). Pressure vessels can either be subjected to high pressure or temperature, however, in most applications, a combination high-pressure and temperature is a normal occurrence in the industry. Because of this, it is important to design pressure vessels to be within a safe working limit and also cope with the high pressures and temperatures (Digvijay and Jewargis, 2015). Pressure vessels in the form of cylinders can be used in different industries such as space depths, nuclear power plants, thermal power plants, fluid supply systems and processes, and chemical industry (Hyder and Asif, 2008).

In practice, high-pressure cylindrical vessels have openings of various shapes and sizes at different positions in the main shell (Gupta and Vora, 2014). Most of these sidewall openings in high-pressure vessels have different shapes and can either be cylindrical or elliptical in cross-section (Makulsawatudom *et al.*, 2004). Hence, for different practical purposes, many arrangements of the openings may be deployed and generally acceptable terminologies describing different types of openings have been proposed. If a pressure vessel has one opening on one of the sides of a vessel, then the opening is referred to as a side hole. While two holes which are symmetrically opposed about an axial plane of symmetry are referred to as cross holes or cross bores. In this scenario, when the bores are projected, the bores go through the main bore of the vessel therefore becoming coincident (Makulsawatudom *et al.*, 2004). If the cross-bore is diametrically opposed, it is referred to as a radial cross bore. Also, if the cross bores are positioned off the radial line of the cylinder, then they are called offset cross bores. The openings, commonly referred to as cross bores, are usually drilled into the wall of the plain thick cylinder (Masu, 1998). These openings are sometimes used to provide for openings that are needed to fit instrumentation accessories for

essential operations (Nziu and Masu, 2019b). These accessories include, inter alia, gas inlets, internal pressure, temperature meters, safety and relief valves, bursting discs, flow circuit meters, lubrication, and inspection holes (Kihiu and Masu, 1995). Therefore, during the design of pressure vessels, provision for openings is inevitable (Nziu and Masu, 2019c). However, drilling of these cross bores results in the generation of high stress regions in the pressure cylinder. Also, geometric discontinuities can change the stress distribution in cylinder walls by the introduction of such features (cross bores) (Kharat and Kulkarni, 2013). These high-stress concentration fields can be measured and are called Stress Concentration Factors (SCF).

These SCFs which are dimensionless (Babu *et al.*, 1970) can be computed analytically, experimentally, or numerically (Nziu, 2018). The experimental method can use different techniques such as strain gauge, grid, photo-elasticity, and brittle coating among others. When conducting work using the experimental technique, prototypes are designed and developed for performing the tests. However, the application of prototypes makes experimental techniques expensive (Masu, 1994). Analytical methods use the theory of elasticity (Zhang *et al.*, 2012) to calculate the stresses of different geometrical configurations. Finally, numerical methods use packages like Finite Element (FE) or boundary integral equation to perform stress analysis (Masu, 1998). FEA numerical technique has been broadly used for stress calculations compared to both analytical and experimental techniques (Kharat and Kulkarni, 2013). The reason is FEA's capability to achieve simulation and provide correct outcomes (Zhang *et al.*, 2012) compared to other techniques. The FEA technique is comparatively cheap, more convenient, and its usage quite easy (Kharat and Kulkarni, 2013).

When pressure vessels are subjected to high pressures, high values of stress concentration are attained and these highly stressed regions become sources of failure (Nabhani, 2012) and hence decreased operating life of the vessels (Choi *et al.*, 2012). Cylinders being used as pressure vessels can fail and lead to loss of life, pose health hazards, and cause destruction of property (Kharat and Kulkarni, 2013). However, these disastrous failures can be avoided using various techniques. For example, when designing and manufacturing cylindrical pressure vessels, design codes are available to be used (Kihiu and Masu, 1995). These design codes, however, only avail sets of wall thickness and their matching hoop stresses that are less than the permissible working stresses without any comprehensive stress analysis (Kihiu *et al.*, 2004). Hence, over-designing using high safety factors is common (Masu, 1997) which in turn lead to the substantive manufacturing budgets

for producing pressure cylinders. Similarly, different processes and techniques have been developed to increase strength of cylinders, this include, shakedown, autofrettage, composite overwrapped cylinders, thick cylinders, and compound cylinders.

Thick-walled cylinders with end enclosures are used as high-pressure vessels to store large amounts of fluids at extreme temperatures and pressures (Nziu and Masu, 2019a). Subsequently, in the traditional design of thick-walled cylindrical pressure vessels, in the event the internal fluid pressure reaches the permissible working stress limit of the cylinder material, the thickness of the cylinder consequently approaches infinite value. However, to circumvent this problem, compound cylinders are deployed (Patil, 2013). Compound cylinders are usually manufactured when two or more cylinders (Bahoum *et al.*, 2017) of different diameters with some interference are shrunk onto each other. Therefore, this shrinking process generates residual stresses in the walls of the compound cylinders and subsequently improve the performance of the cylinder against the working pressure (Kumaresan and Chocklingam, 2018). Compound cylinders, therefore, increase pressure carrying capacity and enables uniform distribution of hoop stress (Miraje and Patil, 2011).

To minimize the associated Stress Concentration Factor (SCF) in compound cylinders, the optimal geometrical configuration becomes important. Therefore, the stress concentration of cross-bored high-pressure vessels is dependent on some major design parameters which include and are not limited to cross bore shrinkage pressure, size, shape, location, and obliquity angle. This paper focuses on one geometrical design parameter- shrinkage pressure.

Consequently, according to Lames's theory (Hearn, 1997) the method for the solution of compound cylinder constructed using similar materials is to break the problem into three separate components; (i) Shrinkage pressure on the inner cylinder; (ii) Shrinkage pressure on the outer cylinder; (iii) Internal pressure only on the complete cylinder. The resulting stresses are then summed up. Shrinkage pressure is a function of the amount of interference and unless the shrinkage pressure is known, stresses cannot therefore be computed (Patil, 2013). Also, shrinkage pressure affects SCF (Reghunath and Sammon, 2014) and therefore plays a critical role in the analysis and optimization of the SCF (Miraje and Patil, 2011). Therefore, the objective of this study is to analyze the behavior of shrinkage pressure on cross bored thick compound cylinders and hence recommend the optimum shrinkage pressure that will generate minimum SCF which can be suitable in the design of high-pressure vessels.

2. Methodology

2.1 Compound cylinder

Two variable parameters that are the sleeve sizes and shrinkage pressure were investigated. These parameters are briefly described hereunder.

a) Sizes of the compound cylinder

A compound cylinder of two thick cylinders was studied. The compound cylinder consisted of two cylinders, that is, the inner sleeve and outer sleeves as shown in Fig. 1

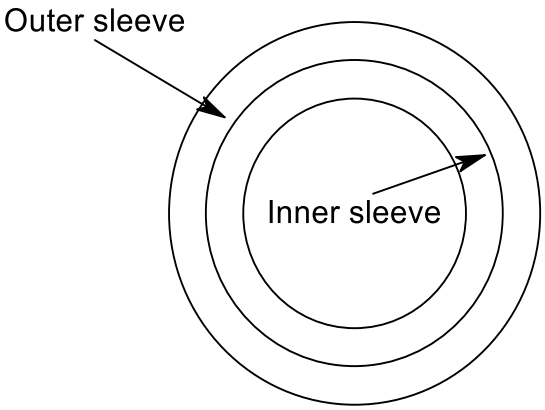

Fig. 1 Compound cylinder

The inner sleeve had an inner radius of 0.05 m and an outer radius of 0.075 m, while the outer sleeve had an inner radius of 0.075 m and an outer radius of 0.1 m. The dimensions of the compound cylinder are shown in Fig. 2. The choice of this compound is that it is a commonly used size for compound cylinder design.

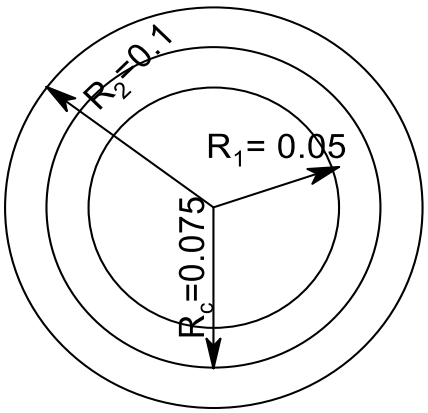

Fig. 2 Dimensions of the compound cylinder

2.2 Shrinkage pressure determination

Shrinkage pressure is developed because of interference or shrinkage allowance. Therefore, to analyze the effect of shrinkage allowance on compound cylinders, interference fits ranging from 0.01 to 0.5 mm were used. These shrinkage allowances were adopted from a study by Amin et al (2014). Hand calculations using theoretical analytical formulae (Hearn, 1997) were used to calculate the corresponding shrinkage pressure that ranged from 4.4733 MPa to 222.662 MPa. The various shrinkage pressures calculated were applied to both outer surface of the inner sleeve (Fig.3 (a)) and the inner surface of the outer sleeve (Fig. 3 (b)).

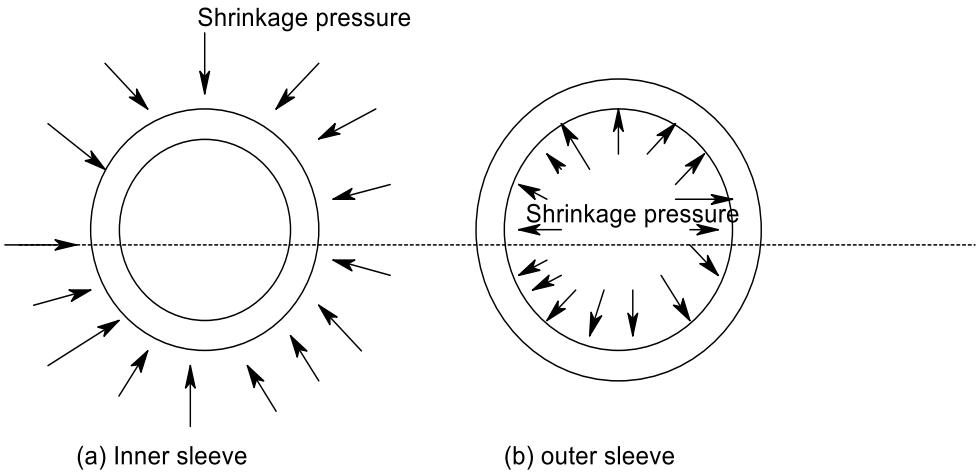

Fig. 3 Shrinkage pressure subjected on the surface of the inner and outer sleeves

The cross bored compound cylinder was subjected to an internal pressure of 1 MPa as shown in Fig. 4at both the main bore and the cross bore.

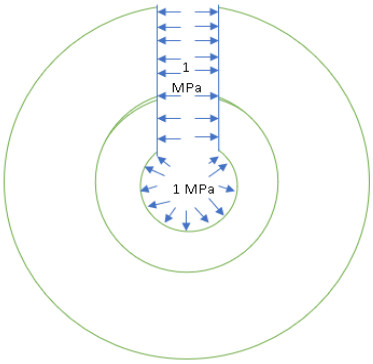

Fig. 4 Internal pressure of 1 MPa applied to a radial cross bored thick-walled monobloc cylinder

2.3 Analysis of Shrinkage pressure

The analyses of these shrinkage pressures were done on cross-bored thick-walled compound cylinders having a radial cross bore size ratio of 0.1 i.e., a cross bore radius of 0.005 m. The choice of this particular cross bore size was done arbitrarily from the list of selected cross bore size ratios from previous literature published. The size of the compound cylinder analyzed was that indicated in section 2.3.1. The model was then subjected to 11 different shrinkage pressures of 4.4733, 5.5915, 11.183, 22.366, 33.549, 44.732, 134.198, 178.93, 223.662 MPa. Hence, the effects of the shrinkage pressure on hoop stress and SCF were studied on the selected circular cross bore at a radial position to establish the optimum pressure. This study used a numerical technique to analyze the compound cylinder. Hence, the finite element method was deployed using Abaqus software, and the generated results were validated analytically.

2.4 Three-Dimensional Finite Element Analysis

Finite Element Analysis (FEA) methods have been deployed by researchers to compare analytical and experimental results (Kharat and Kulkarni, 2013) since they can be used for simulation. Using FEA, the program develops an equation that governs the behavior of each element while considering the connectivity of the elements to other elements by nodes. The program solves simultaneous equations to obtain stress distribution for a model. Abaqus software version 2019 was used in this study due to its availability and capability to simulate stress analysis problems. For this work, 11 different parts were created and analyzed and a standard procedure for modeling has been described in subsequent sections.

2.4.1 Model Creation

The models were created by sketching a quarter profile of a compound cylinder as shown in Fig. 3. A three-dimensional deformable solid body comprising of two cylinders i.e., the inner sleeve and the outer sleeve was created. Hence, the inner sleeve of the model had internal and external radii of 0.05 m and 0.075 m, respectively. While the outer sleeve had internal and external radii of 0.075 m and 0.1 m, respectively.

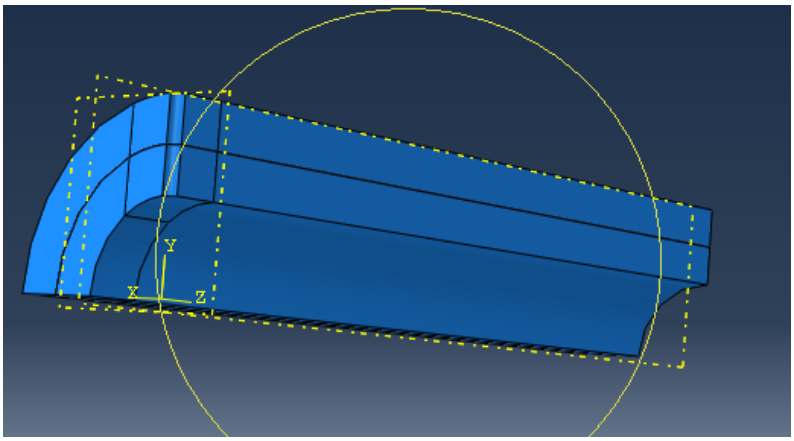

Fig. 5 Compound cylinder: Part profile: Cross Bore Ratio; 0.1

2.4.2 Material definition

A steel material was used in this study and its properties are shown in Table 1.

Table 1 Material properties

Material	**Young's Modulus of elasticity (E)**	**Poisson's ratio (ν)**
steel	207 GPa	0.29

The chosen material used was similar to the one used in the technical literature of compound pressure vessels (Amin *et al.*, 2014).

2.4.3 Section properties assignment and model assembly

After inserting the required material properties, sections had to be created from the section manager module for purposes of assigning properties to the desired sections of Fig. 5. Therefore, both the inner and outer steel section properties were created and defined as both solid and homogeneous. Further, both the inner and outer sleeves were combined to be one assembly of a compound cylinder. Hence, a single assembly of both instances which were independent mesh types of inner and outer sleeves was created. Usually, the single assembly contained all the geometries in the finite element model.

2.4.4 Analysis step creation

Abaqus step menu allows one to create a step, select and define an analysis procedure used during the step and manage the existing step. The initial step was followed by other analyses steps that allow one or more analyses to be taken. For the purposes of this simulation to be carried out, an interference and pressure step were created in the step manage module. The steps created in this

module were useful during the loading module. Hence, the interference step was used during the analysis of the shrinkage pressure of both the inner and outer sleeves. While the pressure step was used for the analysis of the internal pressure of the compound cylinder. Thus, the interference and pressure steps were done separately, and their corresponding results were superimposed. Further, field output requests of the main and cross bore were created.

2.4.5 Application of boundary conditions

Symmetry type boundary conditions were applied at the cut section of the cylinder during the initial step and propagated through the interference and pressure steps. This was to prevent any rigid movement of the model and was created using the boundary condition manager. Subsequently, for all the boundary conditions of both the inner and outer sleeves, symmetry/antisymmetry/Encastre type was used. Therefore, the resultant model displayed in Fig. 5 shows the fixed support on the model for all the planes.

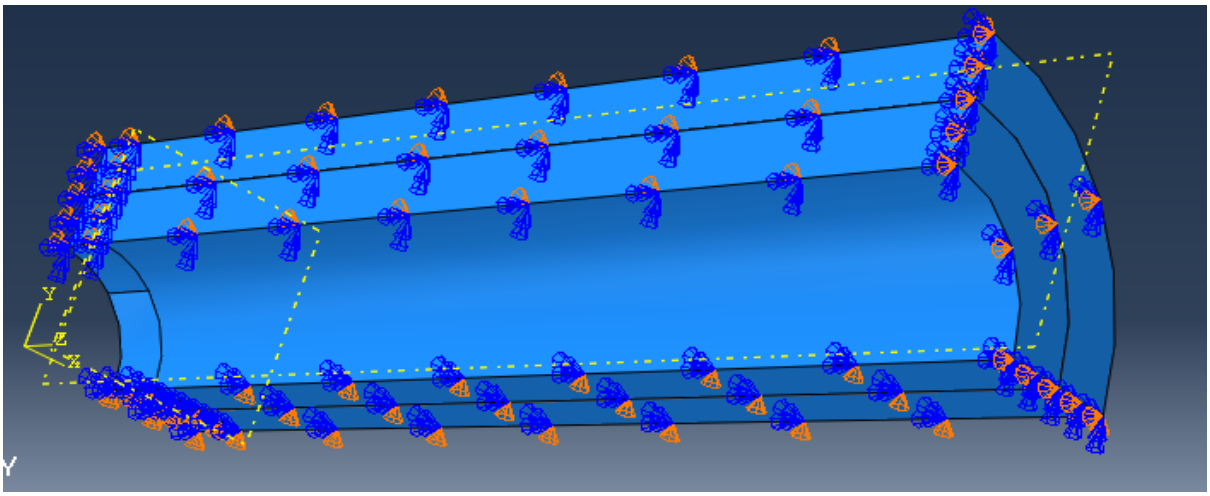

Fig. 5 Boundary conditions for X, Y, and Z planes

2.4.6 Loading Module

The application of the loading module was done in two stages. Namely, the internal pressure for the whole model and that due to shrinkage pressure. However, it is important to note that, the internal pressure was only applied in the pressure step that was created at the step manager in section 2.4.4. Further, the shrinkage pressure for both the inner and outer sleeves was only applicable in the interference step and became inactive in the pressure step.

2.4.6.1 Internal pressure

The internal pressure of 1 MPa introduced at the pressure step was created by the loading manager. This pressure magnitude being the most common pressure used in pressure vessels (Gerdeen and Smith, 1972). Therefore, during modeling, the internal pressure was only subjected to the model during the pressure step. Shrinkage pressure did not affect the model during this step because the load had been deactivated. The generated results in this stage are therefore tensile in nature.

2.4.6.2 Shrinkage Pressure

In addition, shrinkage pressures were subjected to the external surface of the inner sleeve and the internal surface of the outer sleeve. The various shrinkage pressure in section 2.2 was used. Also, this pressure was introduced during the interference step and made inactive during the pressure step.

2.4.6.3 Loading module summary

During the loading module, three models were subjected to different loads. First, the internal surface of the whole model was subjected to a positive internal pressure hence giving results in tension. Secondly, the outer surface of the inner sleeve was subjected to a negative shrinkage pressure giving results in compression, therefore, it was considered as negative. Finally, the inner surface of the outer sleeve was subjected to a positive shrinkage pressure also giving results in tension, therefore, it was considered as positive.

2.4.7 Meshing the model

Complete meshing was done on the compound cylinder model in three stages namely, assigning element type, seeding the instance, and finally meshing the model. Firstly, in this study and according to Abaqus software documentation guidelines, only second-order hexahedral and tetrahedral elements are recommended for stress analysis. Therefore, one of the element types used was C3D20R, that is, a 20-node quadratic brick, reduced integration. Also, second-order C3D10 tetrahedral elements with 10 nodes were used. In this study, cylinders with small cross bore used hexahedral while models with larger cross bore used tetrahedral elements.

2.4.8 Validation of the FEA results

Principal stresses generated by plain compound cylinders were analyzed and compared for validation using analytical and FEA. Firstly, for the analytical solution, calculations using Lame's

theory were performed and results plotted. Secondly, for the FEA model, principal stresses generated at the regions far away from the cross bore (see Fig.4) were used and plotted as well. Because, according to the Saint Venant principle, stresses far away from the cross bore should give results approximately equal to stresses of compound cylinders without cross bores (plain compound cylinders). Also, for the model, results were probed for every point hence, the point of coincidence of the inner and outer cylinders' results was also taken and considered the same.

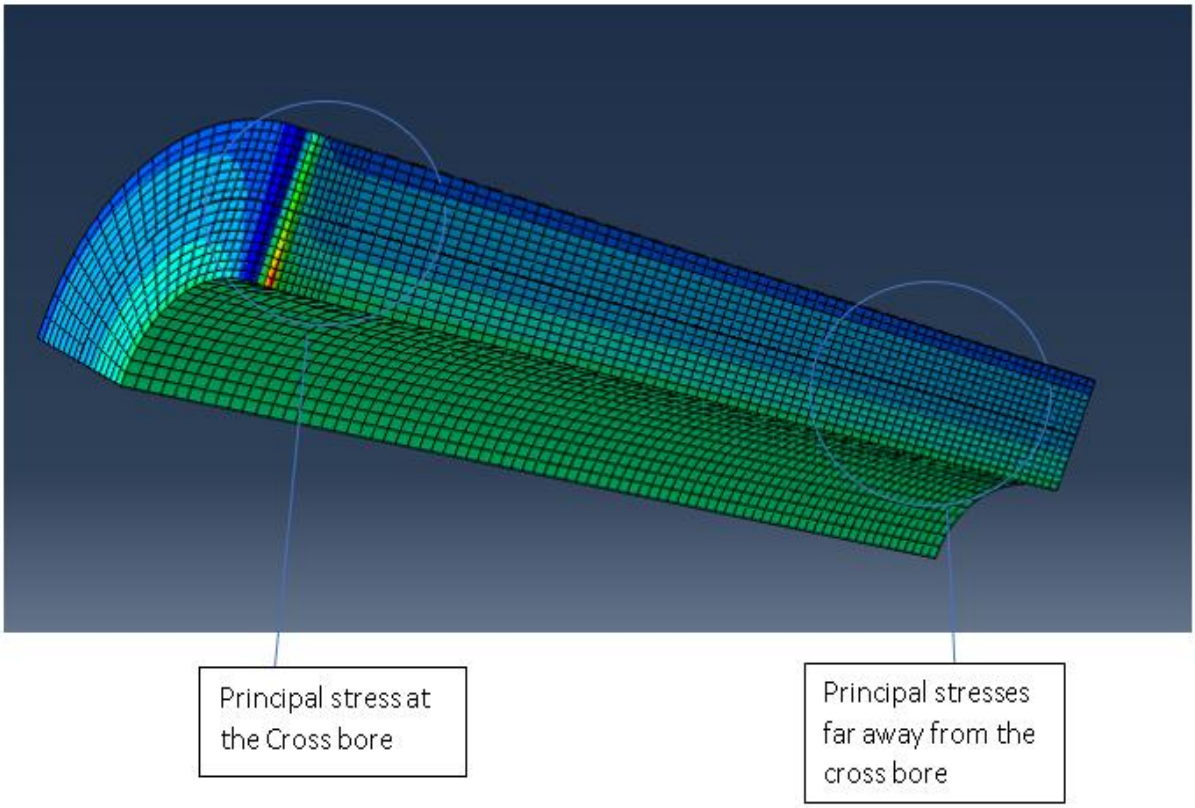

Fig. 4 Validation of data

3. Results and Discussion

The comparison of FEA results was performed and presented under the following subheadings.

3.1 Comparison of finite element and analytical results

Fig. 5 is presented to show the comparison of the FEA results and analytical results.

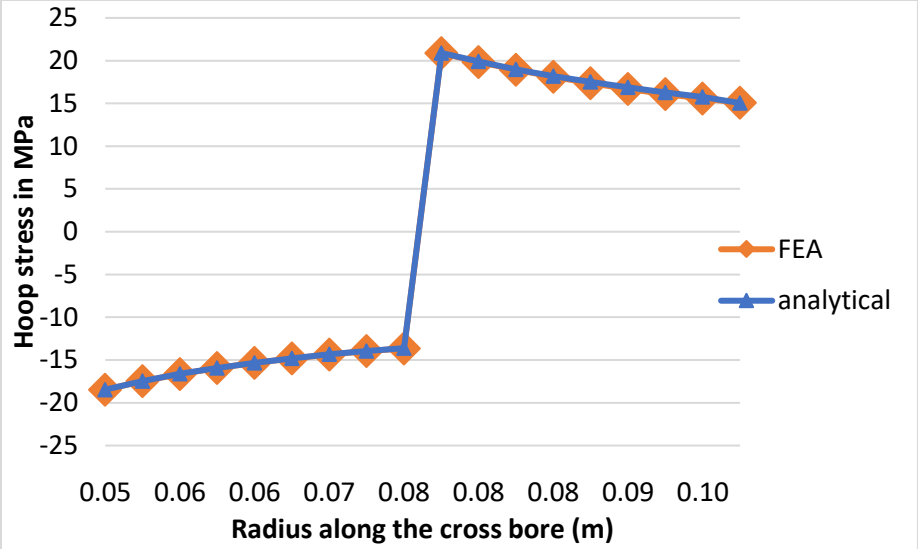

Fig. 5 curves for both analytical and numerical data

Fig. 5 showed an insignificant difference between both analytical and numerical analysis results. Therefore, the results from the cross-bore sections of the compound cylinder followed a similar trajectory; hence the expected results were considered almost accurate with an acceptable margin of error of 5%. Thus, the models were considered validated.

3.2 Shrinkage pressure effects in plain and cross bored compound cylinders

The study generated and analyzed results of hoop stresses along the transverse A-A edge of the cross bore of 0.1 at the radial position under different shrinkage pressures. The transverse edge A-A (at radial position) as shown in Fig. 6, is the radius along the cross bore from the inner to the outer cylinder. The FEA results are then discussed in the following sub-sections.

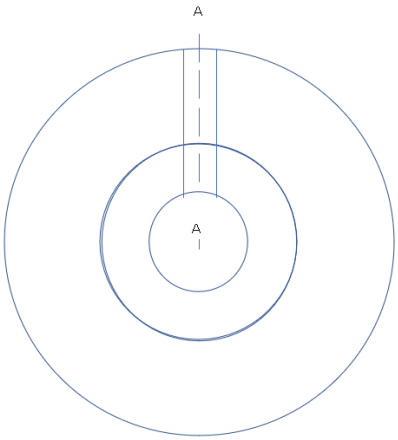

Fig. 6 Cross bore transverse edge A-A.

3.2.1 Effects of shrinkage pressure on hoop stress distribution in plain and compound cylinders

Figures 7 (a) to (k) show the effects of various shrinkage pressures on the hoop stress along the cross-bore radius on cross bored and plain compound cylinders.

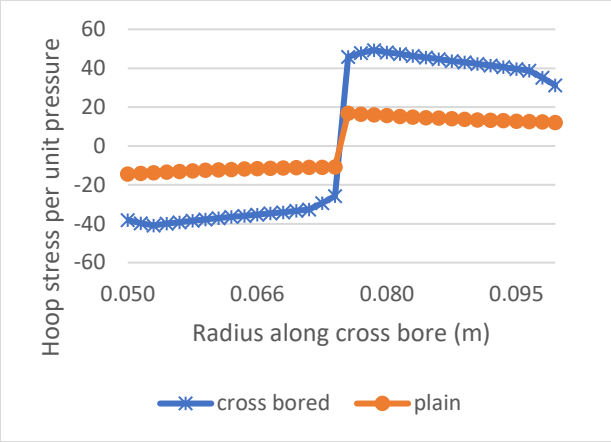

(a) Shrinkage pressure- 4.4733 MPa

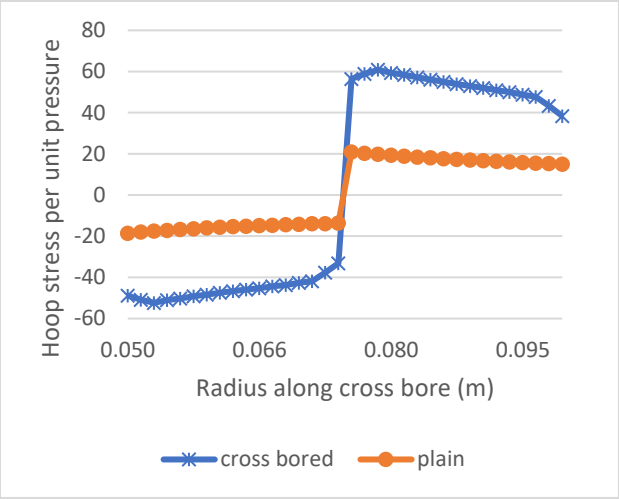

(b) Shrinkage pressure -5.5915 MPa

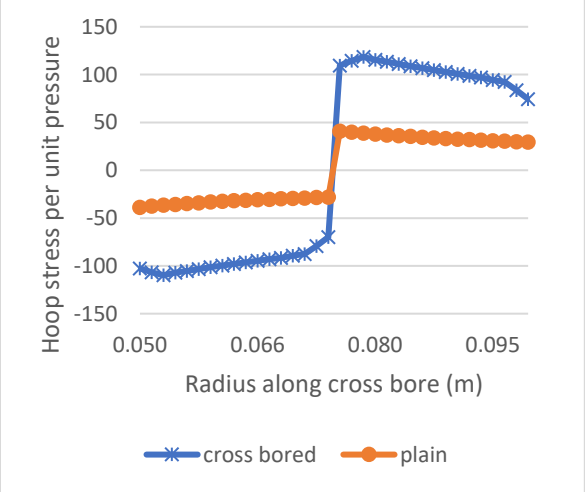

(c) Shrinkage pressure- 11.183 MPa

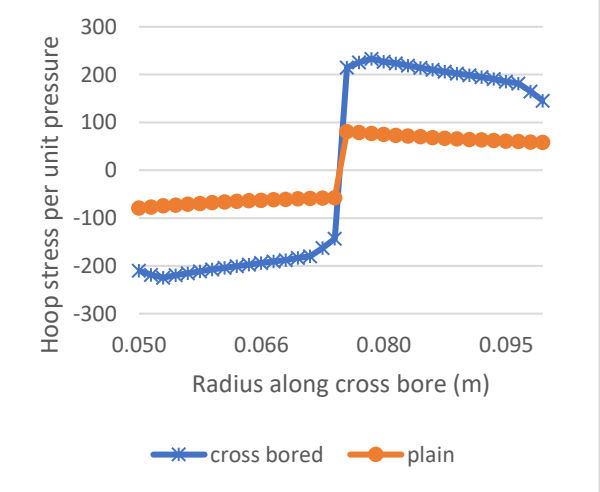

(d) Shrinkage pressure- 22.366 MPa

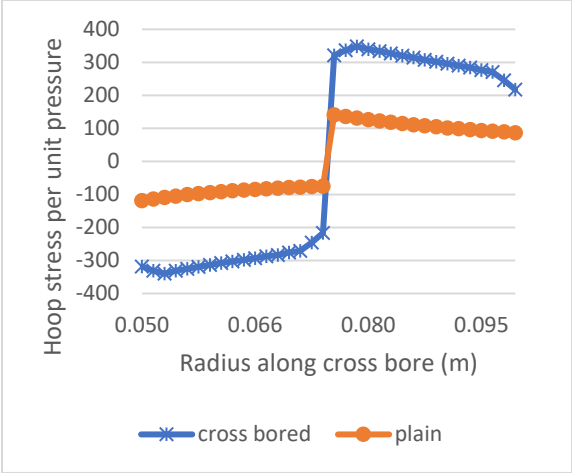

(e)Shrinkage pressure- 33.549 MPa

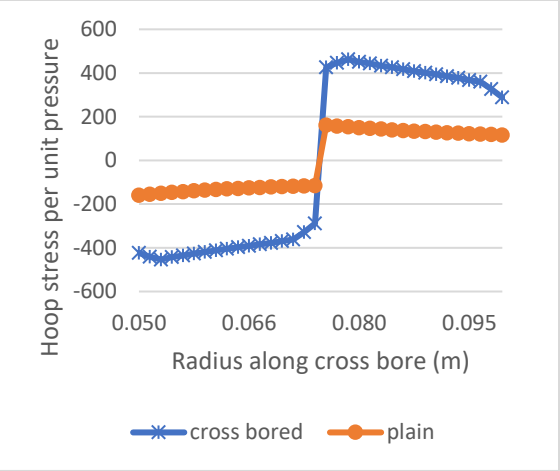

(f) Shrinkage pressure- 44.732 MPa

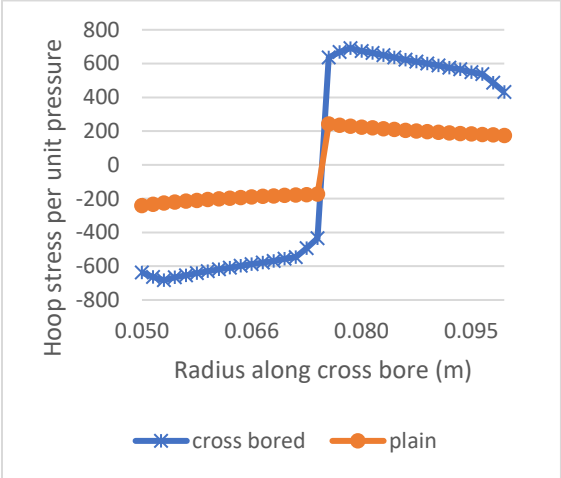

(g) Shrinkage pressure- 67.098 MPa

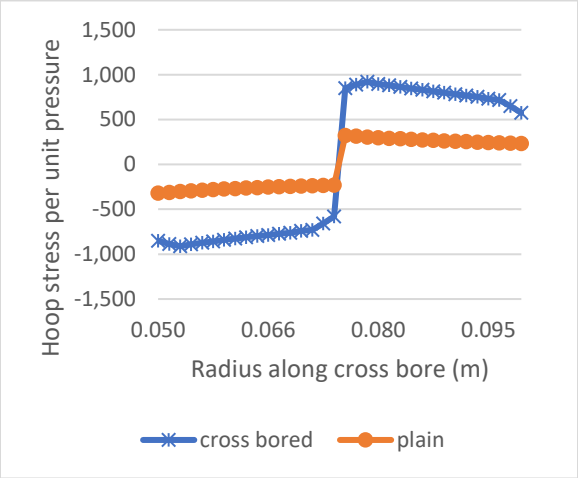

(h) Shrinkage pressure- 89.864 MPa

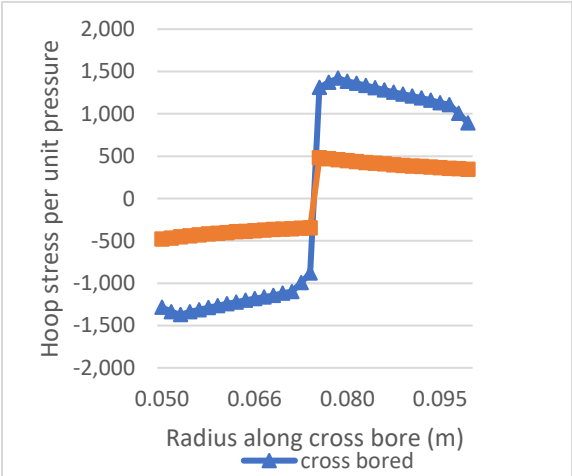

(i) Shrinkage pressure -134.198 MPa

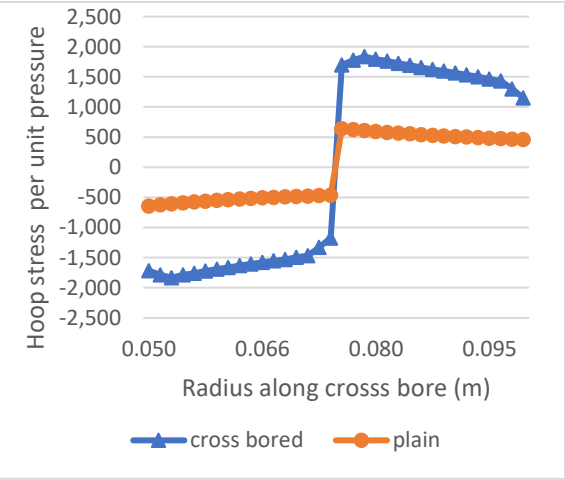

(j) Shrinkage pressure -178.93 MPa

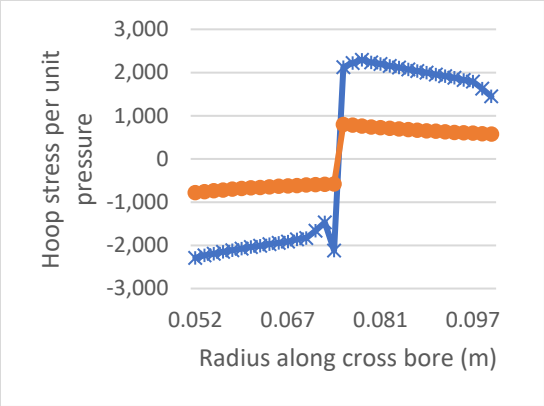

(k) Shrinkage pressure – 113.662 MPa

Fig. 7 (a)-(k) Effects of shrinkage pressure on hoop stress along the transverse edge

From Figures 7(a) to (k), it is observed that shrinkage pressure affects the behavior of hoop stress along the cross bore, hence, the difference between the maximum and minimum hoop stresses becomes more pronounced as the shrinkage pressure increases. Also, it is observed that there is a sudden jump in stresses at the interface of the inner and outer jacket of the compound cylinder. Further, stresses developed in the inner cylinder of the compound cylinder reduced slightly from the cross bore before the stress magnitudes started to increase. However, this decrease in stress becomes more pronounced as the shrinkage pressure increases.

3.2.3 Effects of shrinkage pressure on hoop stress distribution along the transverse edge of a radial circular cross bore

Figure 8 shows the effect of shrinkage pressure on hoop stress along the transverse edge of the circular cross bore at the radial position. Hence the hoop stress per unit pressure was plotted against the transverse edge.

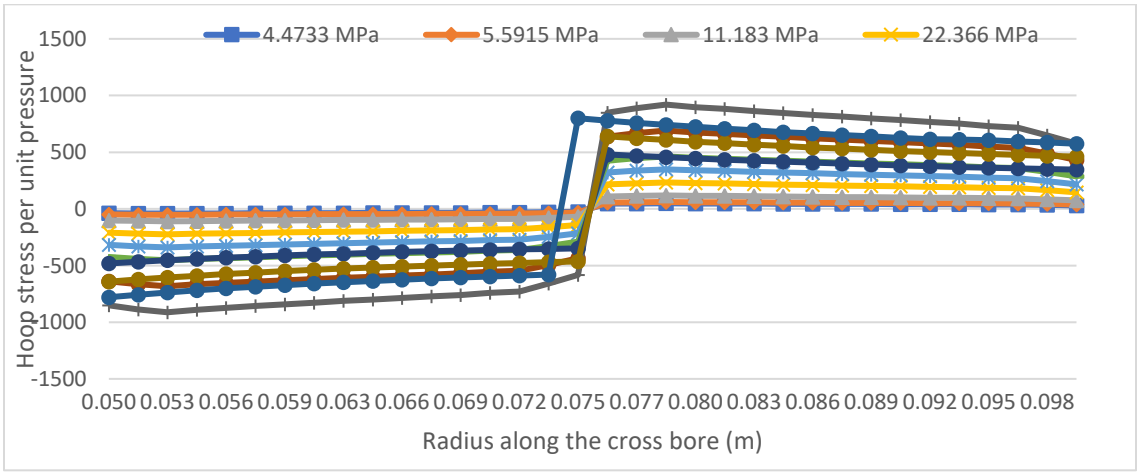

Figure 8. Hoop stress behaviour along the cross bore with change in shrinkage pressure

In Figure 8 the hoop stress distribution along the radius of the cross bore exhibits a pattern that is similar on all shrinkage pressures. For the inner cylinder, the hoop stress increases with an increase in shrinkage pressure. Similarly, for the outer cylinder, the maximum hoop stress is seen to develop in the outer cylinder and located slightly away from the cross-bore intersection. Also, the hoop stresses of the outer cylinder of the compound cylinder reduced as the radius increased.

In general, these behaviors of the hoop stresses can be attributed to the nature of the compound cylinders. With shrinkage pressure higher than the internal pressure, the stresses developed are expected to be lower for the internal cylinder than the outer cylinder. Also, the decrease of the hoop stresses on the outer cylinder along the cross bore radius is related to the increase of cylinder thickness. Further, a sudden increase of stress at the interface of the inner and outer cylinders is caused by the compressive radial stresses.

The behavior of the hoop stresses is consistent with what has been published by Amin *et al*, (2014) and, Miraje and Patil(2011). Similar behavior and pattern of hoop stresses along a compound cylinder have been reported by Amin *et al* (2014). The sudden stress changes at the interface of inner and outer cylinders were also reported by Reghunath and Sammon (2014).

3.3 Optimization of the shrinkage pressure

The optimization of shrinkage pressure was obtained after analyzing the results of 11 models having seven different shrinkage pressures. Also, because there was no change of geometry of the cross bore, only change in shrinkage pressure, all the 11 models were created and analyzed using the identical number of meshes having 33,504 elements. The magnitude of the maximum hoop stress was recorded after the variation of various shrinkage pressures in the model. Hoop stress concentration factors were then computed based on the maximum hoop stress in the cylinder and its corresponding location in the plain cylinder.

3.3.1 Effects of shrinkage pressure on maximum hoop stresses

Figure 9 shows the effects of shrinkage pressure on hoop stresses on both plain and cross bored compound cylinders which were analyzed at the same radial position. The maximum hoop stresses of both cross bored and plain compound cylinders were generated and analyzed.

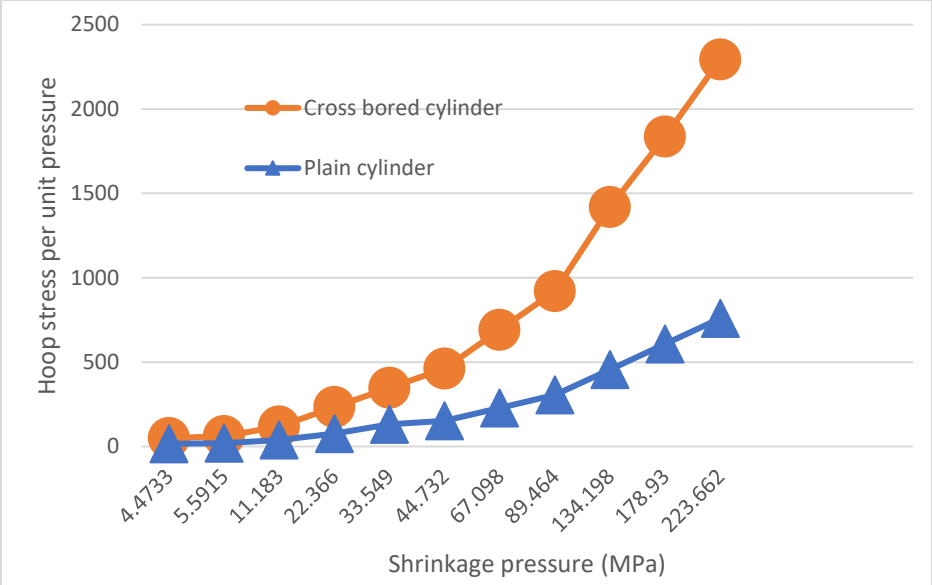

Figure 9. Maximum hoop stress vs shrinkage pressure

It was observed that the maximum hoop stress of each model increased with an increase in shrinkage pressure. It was also observed that differences in the stresses of cross bored and plain cylinder became bigger as the shrinkage pressure increased. This phenomenon can be explained by the fact that when cross bores are introduced to a plain compound cylinder, the cross bore reduces the strength of the compound cylinder. Subsequently, there is reduced pressure carrying capacity that can be carried by the vessel/cylinder before it yields. The observed results are consistent with the work done by Miraje and Patil (2011) and Amin *et al.* (2014).

3.3.2 Effects of shrinkage pressure on Stress Concentration Factor

Figure 10 shows the SCF of various shrinkage pressures subjected to a compound cylinder with a cross bore with a constant cross bore size and main bore diameter.

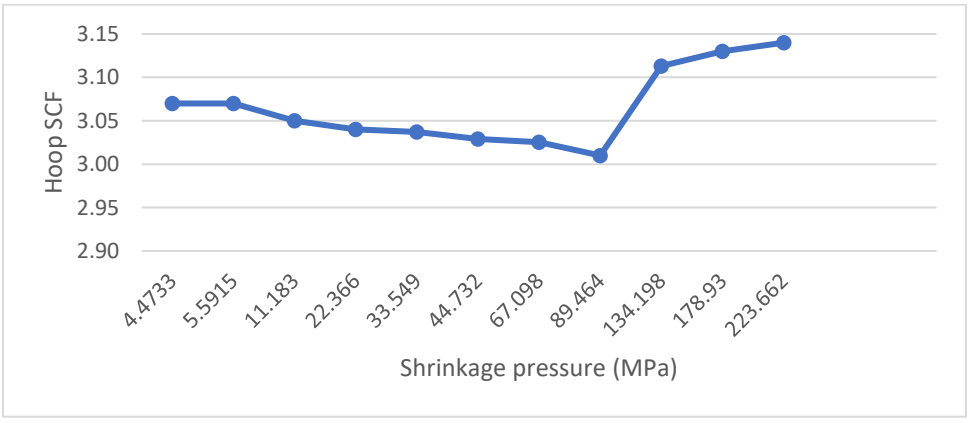

Figure 10. SCF vs Shrinkage pressure

The hoop SCF generally reduces with an increase in shrinkage pressure. However, it was observed that a minimum SCF was achieved when the shrinkage pressure of 89.464 MPa was introduced at the interference of the inner and outer cylinders. , it can be noted that no other shrinkage pressures were considered between 67.098 MPa and 134.198 MPa. Therefore, it is observed that interference fits have effects on stress patterns. The minimum SCF value was generated as a result of the shrinkage pressure presence on the cylinder and occurred at the same point as all other SCFs generated.

4. Conclusion

Three-Dimensional FE analysis was done on a cross bored thick-walled compound cylinder and was validated using theoretical analysis. The effect of shrinkage pressure on hoop stress as a geometric design parameter was studied. From the results of this study, the following points may be concluded.

- The numerical solution used in this study complemented the analytical solutions available in the literature. Therefore, the numerical results gave fairly accurate results of hoop stress of all the models created and analyzed and were within acceptable margin of error of 5%.
- Shrinkage pressure affected the hoop stress distribution and SCF. With shrinkage pressure higher than the internal pressure, the stresses developed are expected to be lower for the internal cylinder than the outer cylinder. Also, the decrease of the hoop stresses on the outer cylinder along the cross bore radius is related to the increase of cylinder thickness. Further, a sudden increase of stress at the interface of the inner and outer cylinders is caused by the compressive radial stresses.
- After analyzing 11 different shrinkage pressures ranging from 4.4733 to 223.662 MPa, the SCF varied from 3.01 to 3.14 meaning a variation of 4.3% variation.
- The shrinkage pressure of 89.464 MPa was considered the most optimum because it gave the minimum SCF magnitude of 3.01.

Abbreviation

SCF: Stress Concentration Factor; FEA: Finite Element Analysis

Acknowledgment

This research work is supported by the Vaal University of Technology. The authors wish to thank the Department of Mechanical Engineering at the Vaal University of Technology for facilitating this work.

Availability of data and material

All cited articles in this review article are available upon request.

Authors' contributions

All authors jointly contributed to the development of this journal article.

Competing interests

The authors declare that they have no competing interests.

REFERENCES

Amin, M.T., Rahman, A. and Ali, M. (2014), "Optimum Design of Compound Pressure Vessel", *Global Journal Research Inc. (US)*, Vol. 13, pp. 18–23.

Babu, R.N., Ramana, K. V. and Rao, K.M. (1970), "Determination of Stress Concentration Factors of a Steam Turbine Rotor Using Finite Element Analysis", *Journal of Mechanical Engineering*, Vol. 40 No. 2, pp. 137–141.

Bahoum, K., Diany, M. and Mabrouki, M. (2017), "Stress analysis of compound cylinders subjected to thermo-mechanical loads", *Journal of Mechanical Science and Technology*, Vol. 31 No. 4, pp. 1805–1811.

Choi, W., Fujiyama, K., Kim, B. and Song, G. (2012), "Development of thermal stress concentration factors for life assessment of turbine casings", *International Journal of Pressure Vessels and Piping*, Vol. 98, pp. 1–7.

Digvijay, K. and Jewargis, S. (2015), "Stress Analysis of Pressure Vessel with Different Type of End Connections by FEA", *International Journal of Innovative Research in Science, Engineering and Technology*, Vol. 4 No. 5, pp. 2769–2775.

Gerdeen, J.C. and Smith, R.E. (1972), "Experimental determination of stress-concentration factors in thick-walled cylinders with crossholes and sideholes", *Experimental Mechanics*, Vol. 12 No. 11, pp. 530–536.

Gupta, S.R. and Vora, C.P. (2014), "A Review Paper on Pressure Vessel Design and Analysis", *International Research Journal of Engineering and Technology*, Vol. 3 No. 3, pp. 295–300.

Hearn, E. (1997), *MECHANICS OF MATERIALS 1*, edited by HEARN, E.J.B.T.-M. of M. 1 (Third E., 3rd ed., Butterworth-Heinemann, Oxford, available at:https://doi.org/https://doi.org/10.1016/B978-0-7506-3265-2.50024-4.

Hyder, M.J. and Asif, M. (2008), "Optimization of location and size of opening in a pressure vessel cylinder using ANSYS", *Engineering Failure Analysis*, Vol. 15 No. 1, pp. 1–19.

Kadam, R., Jagadale, S. and Karande, R. (2018), "a Review on Stress Concentration Factor of Composite Pressure Vessel", *International Journal of Advance Research in Science and Enginerring*, Vol. 7 No. 1, pp. 969–974.

Kharat, A. and Kulkarni, V. (2013), "Stress Concentration at Openings in Pressure Vessels–A Review", *Int. j. Innov. Res. Sci. Eng. Technol.*, Vol. 2 No. 3, pp. 670–678.

Khobragade, R.R. and Hiwase, V. (2017), "Design & Analysis of Pressure Vessel with Hemispherical & Flat Circular End", *IJIRST-International Journal for Innovative Research in Science & Technology|*, Vol. 4 No. 1, available at: www.ijirst.org.

Kihiu, J. and Masu, L. (1995), "The effect of chamfer and size on the stress distributions in a thick-walled cylinder with a cross bore under internal pressure", *Jomo Kenyatta University of Agriculture and Technology. Digital Repository*, Vol. 2 No. February, pp. 73–78.

Kihiu, J., Rading, G. and Mutuli, S. (2004), "Overstraining of flush plain cross-bored cylinders", *Proceedings of The Institution of Mechanical Engineers Part C-Journal of Mechanical Engineering Science*, Vol. 218, pp. 143–153.

Kumaresan, M. and Chocklingam. (2018), "Stress Analysis in Compound Cylinder and Autofrettaged Cylinders", *International Journal of Engineering Research and Technology*, Vol. 7 No. 4.

Makulsawatudom, P., Mackenzie, D. and Hamilton, R. (2004), "Stress concentration at crossholes in thick cylindrical vessels", *The Journal of Strain Analysis for Engineering Design*, IMECHE, Vol. 39 No. 5, pp. 471–481.

Masu, L.M. (1994), "Stress and fatigue behavior model for a pressure vessel containing cross bore", *East African Journal of Engineering*, Vol. 1 No. 2.

Masu, L.M. (1997), "Cross bore configuration and size effects on the stress distribution in thick-walled cylinders", *International Journal of Pressure Vessels and Piping*, Vol. 72 No. 2, pp. 171–176.

Masu, L.M. (1998), "Numerical analysis of cylinders containing circular offset cross-bores", *International Journal of Pressure Vessels and Piping*, Vol. 75 No. 3, pp. 191–196.

Miraje, A. and Patil, S. (2011), "Minimization of material volume of three layer compound cylinder having same materials subjected to internal pressure", *International Journal of Engineering, Science and Technology*, Vol. 3 No. 8.

Nabhani, F. (2012), "Reduction of Stresses in Cylindrical Pressure Vessels Using Finite Element Analysis", in Ladokun, T. (Ed.), , IntechOpen, Rijeka, p. Ch. 15.

Nziu, P. and Masu, L. (2019a), "Elastic Strength of High Pressure Vessels with a Radial Circular Cross Bore", *International Journal of Mechanical and Production Engineering Research and Development*, Vol. 9, pp. 1275–1284.

Nziu, P.K. (2018), *Optimal Geometric Configuration of a Cross Bore in High Pressure Vessels. In Doctorate Thesis*, Vaal University of Technology.

Nziu, P.K. and Masu, L.M. (2019b), "Cross bore size and wall thickness effects on elastic pressurised thick cylinders", *International Journal of Mechanical and Materials Engineering*, Vol. 14 No. 1, p. 4.

Nziu, P.K. and Masu, L.M. (2019c), "Cross bore geometry configuration effects on stress concentration in high-pressure vessels: a review", *International Journal of Mechanical and Materials Engineering*, Vol. 14 No. 1, p. 6.

Patil, A. (2013), "Finite element analysis of optimized compound cylinder", *Journal of Mechanical Engineering Research*, Vol. 5 No. 5, pp. 90–96.

Phalguna, N. (2017), "Stress and Failure Analysis of Thick Walled Cylinder with Oblique Hole",

International Journal of Engineering Research And, Vol. V6.

Reghunath, R. and Sammon, K. (2014), "Analysis of Internally Pressurised Thick Walled Cylinders", *Journal of Basic and Applied Engineering Research*, Vol. 1 No. 2, pp. 83–89.

Thattil, M. and Pany, C. (2017), "Design and Analysis of Pressure Vessel with different end domes.", *International Journal of Science, Engineering and Technology Research (IJSETR) Volume 06,, Issue 08 August 2017,, ISSN: 2278 - 7798*.

Zhang, Q., Wang, Z.W., Tang, C.Y., Hu, D.P., Liu, P.Q. and Xia, L.Z. (2012), "Analytical solution of the thermo-mechanical stresses in a multilayered composite pressure vessel considering the influence of the closed ends", *International Journal of Pressure Vessels and Piping*, Vol. 98, pp. 102–110.

EFFECT OF AIR MASS FLOW RATES ON DRYING RATE OF PRETREATED OYSTER MUSHROOMS IN A CONVECTIONAL HOT AIR DRYER

Wilberforce Okwara[1, *], Mercy Mboya[1], Daudi Nyaanga[1], Musa Njue[1]

[1]Department of Agricultural Engineering, Egerton University, Nakuru, Kenya

[*]Corresponding author, email: okwaramayabi@gmail.com

Abstract

Mushrooms have been considered an alternative to provide better nutrition and medicinal attributes despite having a very short shelf life of 1-3 days. Water loss is an important physiological process that affects shelf life. Postharvest processes to extend this period has posed a challenge worldwide. Thus, the broad objective of this study was to evaluate the effect of various air mass flow rates (0.005, 0.023 and 0.033 kg/s) on the drying rates of pretreated oyster mushroom in a convectional hot air dryer. Convective hot air-drying method was used in a fabricated cabinet dryer to monitor the drying rate. Air mass flow rate was varied by changing speed of the blower. Weight of the samples were recorded at an interval of 15 minutes for three hours. Anemometer was used to measure the velocity of air which was used for calculating mass flow rate. Further, mushroom powder was subjected to organoleptic test since quality is a key concern to the consumers. The results indicated that the drying rate was highest at air mass flow rate of 0.033 kg/s. Value of 0.005 kg/s took long to dry making the conditions uneconomical. This knowledge about convectional hot-air drying as an affordable method of preservation to enhance shelf life to up to one year, will not only reduce wastage after harvesting but also help farmers achieve optimum efficiency towards realization of Sustainable Development Goal Number #2 to end hunger and achieve food security.

Keywords: Mass Flow Rate, Drying Rate, Pretreated Mushroom, Convectional Hot Air Dryer

1. Introduction

Mushroom has been consumed by man as an edible macro fungus with a distinctive fruiting body since ancient times. Patel et al. (2012) in a study reported that initially, mushrooms were only consumed for their pleasant flavor, however, nowadays they are consumed due to their nutritional and medicinal contribution (Toledo et al., 2013). More than 140,000 species of mushrooms, however, not all species are edible, most common types of edible mushrooms include oyster, button and shiitake. (Teklit, 2015). According to Sánchez (2010), oyster (*Pleurotus spp.)* is the second most cultivated edible mushroom worldwide after *Agaricus bisporus* (button). Mushrooms have high water content, 87-95% (w.b), which makes them highly perishable with extremely short shelf life of three days (Arumuganathan et al., 2009). One of the major challenges faced by small scale farmers is preservation of mushrooms.

Drying has been proven as the long-term solution for mushroom preservation. Yapar et al. (1990) classified drying methods into four as solar drying, freeze drying, microwave drying and convectional hot air drying. Solar drying is the commonly used method. Unfortunately, the final products of this method are of poor quality, unhygienic and the yields are low due to losses during drying. Freeze drying works on the principle of sublimation. Materials are cooled by a freezer through mechanical refrigeration with freezing temperatures between −50°C and −80°C (Shukla, 2011).

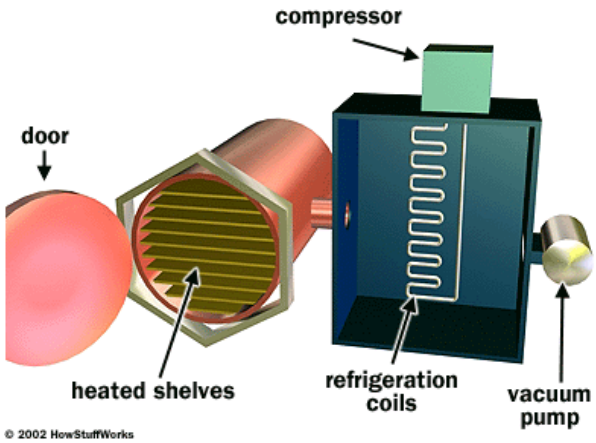

Figure 2.1: *Freezing dryer*

Sutar & Prasad (2008) reported that microwave drying involves converting electromagnetic energy direct to kinetic energy of water molecules. This method however, causes destruction of tissues and has non uniform heating as indicated by Motevali et al. (2011).

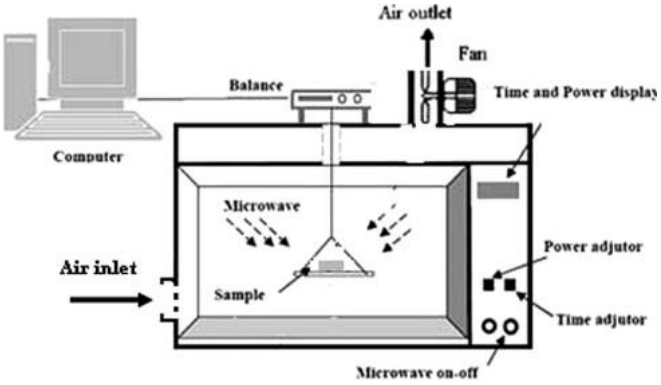

Figure 2.2: *Microwave dryer*

Arumuganathan et al. (2010) studied convectional hot air drying and reported to be comparatively simple, efficient and economical method. Also, this method, dehydration rate is directly related to air temperature and mass flow rate in the process (Natalia *et al.*, 2018).

Drying is the most inexpensive method to increase shelf life of mushrooms (Yapar et al., 1990). According to Walde et al. (2006), fungus can be contained for more than one year if stored in an airtight condition. Various drying conditions affect quality of mushrooms produced (Waluyo et al., 2019). These include type of dryer used and air mass flow rates. Due to the low density of mushrooms, convectional hot air drying has been considered inexpensive and effective way. Although it is slower than vacuum, drying mushrooms from 7.5% to 2% moisture content is faster than fluidized bed or microwave oven. Also, it has the advantage of being easy to operate than vacuum drying. Thus, the purpose of this study was to determine the effect of air mass flow rates on drying of pretreated mushrooms in a convectional hot air dryer.

2. Materials and Methods

2.1 Research Site

The study was done at the Faculty of Engineering and Technology, Department of Agricultural Engineering at the Energy Laboratory; Egerton University, Njoro, Nakuru County (Latitude 0°22’30.0” S Longitude 35°55’30.0” E). Laboratory tests for analysis of mushrooms were carried out at Egerton University’s Food Science and Engineering Processing Laboratories.

2.2 Sample Acquisition and Preparation

Fully matured oyster mushrooms were procured from a farm at Njokerio, Njoro Sub-County in Nakuru County and kept in a refrigerator (4°C) prior to the experiments. For sample preparation, the mushrooms of approximately same size were selected and washed. Then, the stalks were separated from the caps and chopped into size of 4 cm. Upon drying in presence of hot air browning reaction is activated so a sample of 50 g was pretreated by blanching. This was done by dipping the slices to hot water (80°C), heated by electric heater (**), for four minutes and dipping the slices immediately into a bath of ice water for the same amount of time. Triplicate samples were used to determine the moisture content (dry basis) using average weight values measured and recorded at an interval of 15 minutes. A digital weighing balance (***) was used to measure weight and the cabinet dryer was started about 30 minutes before starting the experiments so as to achieve steady-state conditions.

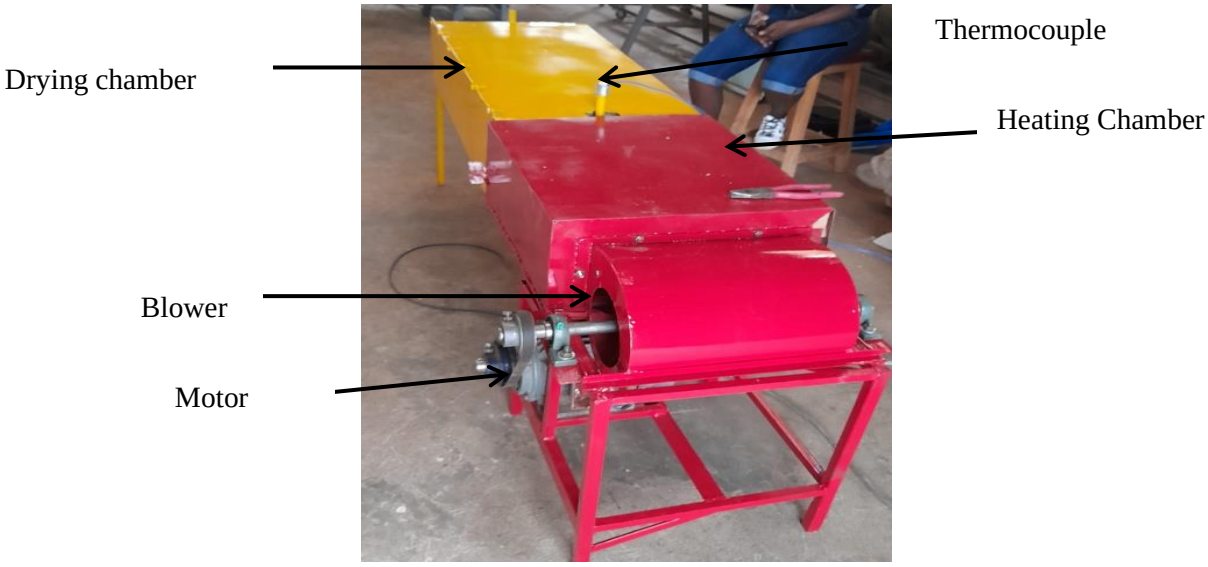

Figure 2.3: *Convectional Hot Air Dryer*

2.3 Sample Preparation

Mushroom slices weighing about 50 ± 1 g were spread on the tray. The drying experiments were conducted at 0.005, 0.023 and 0.033 kg/s air mass flow rates. The air flow rate was varied by changing speed of the blower. Weight of the samples were recorded at an interval of 15 minutes

for three hours. An anemometer (***) was used to measure the velocity of air which was used for calculating mass flow rate while a PID controller was used to vary the temperatures.

2.4 Performance Evaluation

The performance of resulting mushrooms from the cabinet dryer was assessed and determined using equations 2.1, 2.2 and 2.3, as used by Waluyo et al. (2019).

The mass flow rate of air was calculated as follows:

$$\dot{m} = \rho \times A \times V \quad (2.1)$$

Where;

$\dot{m}$ = Air mass flow rate (kg/s)

ρ = Density of air (1.225 kg/s)

A = Surface area (m^2) which was given by $0.38\ m \times 0.1\ m = 0.038\ m^2$

V = Velocity of air (m/s). The velocities used were 0.1, 0.5 and 0.7 m/s.

The moisture content was calculated on dry-basis equation:

$$X_t = \frac{W_t - W_d}{Wd} \quad (2.2)$$

Where;

X_t= Moisture content at time t (g water/g dry solids)

W_t= Weight of the wet material at time t (g)

W_d= Dry solids weight (g)

The drying rate was calculated using the following equation:

$$DR = -\frac{dX}{dt} = -\frac{X_{i-1} - X_i}{t_i - t_{i-1}} \quad (2.3)$$

Where;

Xi= Moisture fraction (g of water/g of dry solid) at i^{th} time interval

$\frac{dy}{dt} =$ Drying rate (g of water g of dry solids/min)

X_{i-1} = Previous value of moisture content (g of water/ g of dry solids)

X_i= Initial moisture content (**)

t_i= Initial time (min)

t_{i-1}= Previous time (min)

2.5 Organoleptic Test

Organoleptic tests conducted was adopted from a study by Dhingra and Jood (2001), with two samples codes A (sample without mushroom powder) and B (sample with oyster mushroom powder). The parameters tested included savory flavors, aroma, color and texture. The assessment conducted was by observing the sample and filling out the questionnaire with a numerical assessment in each parameter, this was carried out on 35 random panelists. The level of the user's preference was expressed on a hedonic scale that distinguished some product offered.

2.6 Data Analysis

Statistical analysis software (SAS) and analysis of variance (ANOVA) was used to analyze data at a 5% significance level. The levels of significant difference between the factors were determined using F-test. MS Excel and graphs were used.

3. Results and Discussion

3.1 Effect of Air Mass Flow Rates on the Drying Rate of Mushroom

Values of drying rates of mushrooms at 0.005, 0.023 and 0.033 kg/s flow rates at different times were tabulated and presented as shown in Table 3.1.

Table 3.1: *Experimental Output of Moisture Content and Drying rates at Different Flow Rates*

Time	**Average Weight (g)**	**0.005 kg/s**		**0.023 kg/s**		**0.033 kg/s**	
		M.C **g.water/ g.drymatter**	**Drying Rate g/min**	***M.C*** **g.water/ g.drymatter**	**Drying Rate g/min**	***M.C*** **g.water/ g.drymatter**	**Drying Rate g/min**
0	50.0	525.0	0.0^{a}	525.0	0.0^{a}	525.0	0.0^{a}
15	45.5	468.8	4.8^{b}	433.3	5.3^{b}	290.0	7.7^{e}
30	40.2	402.5	4.4^{b}	333.3	4.6^{b}	216.3	4.9^{b}
45	35.3	341.3	4.1^{b}	238.3	4.3^{b}	143.6	4.8^{b}
60	33.0	312.5	2.5^{c}	183.3	3.7^{b}	100.0	4.1^{b}
75	30.0	275.0	2.5^{c}	138.9	2.7^{c}	65.0	3.3^{b}

90	27.0	237.5	2.1^{c}	100.0	2.5^{c}	25.0	2.7^{c}
105	24.5	206.3	1.5^{d}	75.0	1.6^{d}	16.3	1.3^{d}
120	22.2	177.5	1.2^{d}	53.3	1.3^{d}	6.3	0.6^{a}
135	19.2	140.0	0.8^{a}	33.3	1.0^{d}	2.5	0.3^{a}
150	17.5	118.8	0.5^{a}	8.3	0.7^{a}	0.0	0.0^{a}
165	15.2	90.0	0.4^{a}	5.6	0.4^{a}	0.0	0.0^{a}
180	13.7	71.3	0.1^{a}	2.8	0.2^{a}	0.0	0.0^{a}

**M.C = moisture content*

Means within a column with the different superscript letters across column are statistically different (p >0.05)

Table 3.1 shows values increasing with an increase in air mass flow rate. However, values decreased with time. At a lower air flow rate, 0.005 kg/s, there may be insufficient air circulation throughout the length of the drying chamber which reduces the amount of moisture removed from mushroom and increases the drying time and hence, the energy consumption. As the air flow rate increases, it increases diffusion of hot air into each sample. So that the water content in the sample can be reduced faster and shorten the drying time. In Figure 3.1, the fastest drying time was achieved at the highest air flow rate of 0.033 kg/s for both oyster mushrooms.

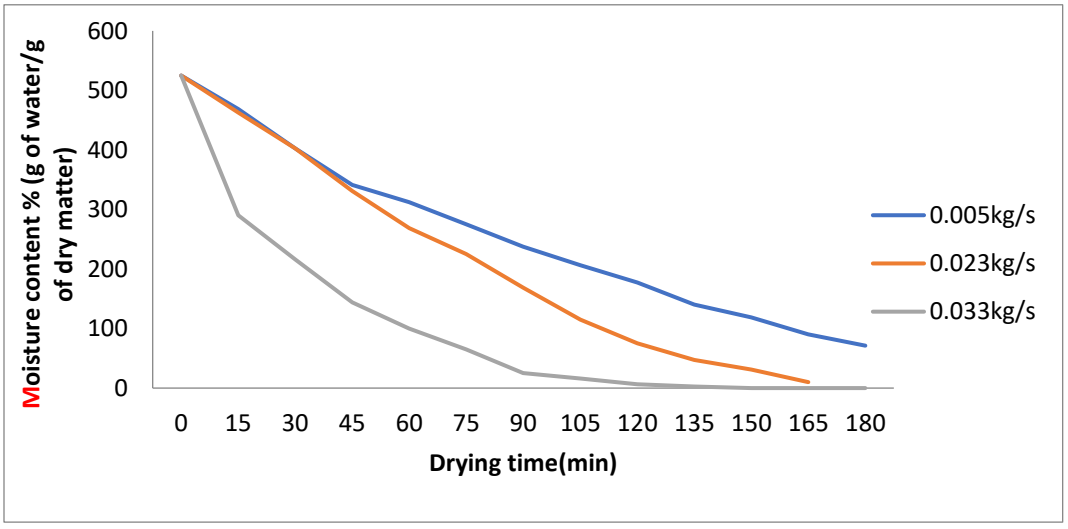

Figure 3.1: *Effect of Different Air Flow Rate on Drying Rate*

From both Table and Figure 3.1, towards the end of the drying process, both moisture contents with varying flow rates experience almost the same value. According to Waluyo et al. (2019) this happens because relative humidity in the drying air used has the same value. From Table 3.1, air flow is not evenly distributed. A study by Singh et al. (2007) on drying characteristics of mushroom slices in a cabinet dryer showed that air mass flow rate has significant effect on the moisture removal ($p < 0.05$). Figure 3.2 shows the fluctuating drying rate of mushrooms at different mass flow rates from Table 3.1.

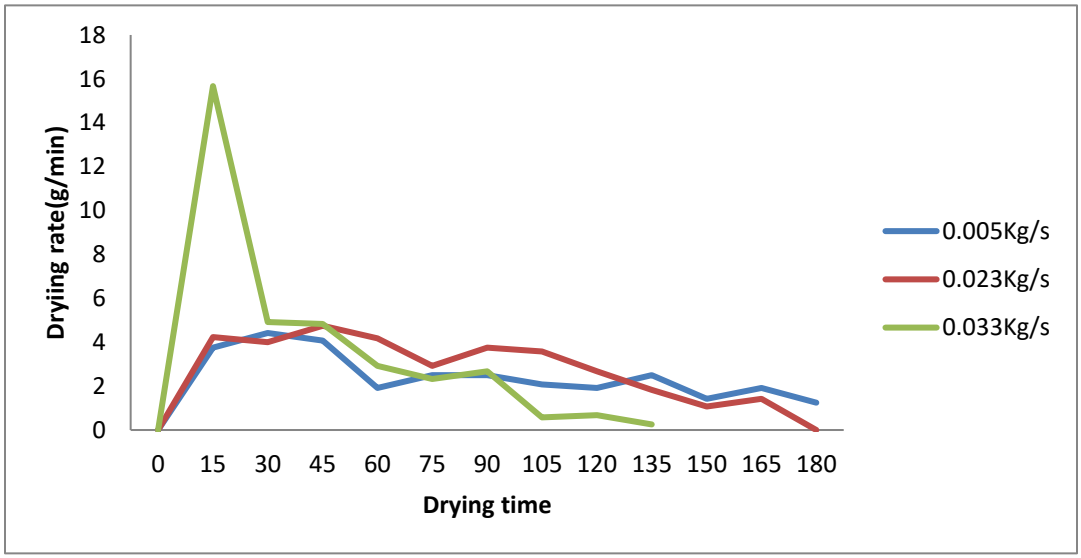

Figure 3.2: *A Graph of Drying Rate against Drying Time of Oyster Mushroom.*

At high air mass flow rate, more air is pumped into the cabinet that resulted in more heat delivery to the drying unit, thus, air mass flow rate is directly related to drying rate. The results from this study agree with the findings of Ahmad (2011) and Colak & Hepbasli (2007) who reported an increasing drying rate with increasing air mass flow rate. Also, a study by Doshi et al. (2017) concluded that increase in air mass flow rate results into an increase in the efficiency of the dryer. However, Ekka et al. (2020) reported that increase beyond optimum has no effect on heat gain and therefore no effect on the drying rate

3.2. Organoleptic Test

Organoleptic test results are presented in Table 3.2. The results of the assessment of savory flavors in various samples given, sample A obtained the highest score of 54.3%. For aroma, color and

texture, sample B obtained the best value (65.7, 57.1 and 68.6%, respectively) compared to sample A. (very preferred).

Table 3.2: *Organoleptic test of mushroom powder*

	Parameters			
Sample	**Savory Test (%)**	**Aroma (%)**	**Color (%)**	**Texture (%)**
A	54.3	34.3	42.9	31.4
B	45.7	65.7	57.1	68.6

4. Conclusions

At a constant air temperature, the study conclusively established that drying rate is directly related to mass flow rate. ***. However, extremely high mass flow rate has no effect on the drying rate. Also, at low air mass flow rate, the air blown into the drying chamber is minimal resulting to reduced heat and mass transfer. Thus, considering the three mass flow rates, 0.033 kg/s value yielded good quality products. Further, apart from savory test, mushrooms were preferred for their aroma, color and texture.

Acknowledgements

We acknowledge Egerton University through the Faculty of Engineering and Technology, Department of Agricultural Engineering for providing laboratory space, equipment and technical assistance. Our sincere gratitude goes to Prof. D. Nyaanga and Dr. M. Njue who helped us develop the idea on food security and financed the research study.

References

Ahmad. (2011). Dependence of the effective diffusion coefficient of moisture with thickness and temperature in convective drying of sliced materials. A study on slices of banana, cassava and pumpkin — ScienceDirect. https://www.sciencedirect.com/science/article/abs/pii/S0260877410004462

Arumuganathan, T., Ramarathinam, M., Chandrasekaran, I., Rai, R., & Kamal, S. (2010). Texture and quality parameters of oyster mushroom as influenced by drying methods. International Agrophysics, 24, 339–342.

Colak, N., & Hepbasli, A. (2007). Performance analysis of drying of green olive in a tray dryer. Journal of Food Engineering, 80(4), 1188–1193. https://doi.org/10.1016/j.jfoodeng.2006.09.017

Correia, A., Loro, A., Zanatta, S., Spoto, M., & Vieira, T. (2015). Effect of Temperature, Time, and Material Thickness on the Dehydration Process of Tomato. International Journal of Food Science, 2015, 1–7. https://doi.org/10.1155/2015/970724

Dhingra, S & Jood, S. (2001). Organoleptic and nutritional evaluation of wheat breads supplemented with soybean and barley flour. Food Chemistry, 77(2001), 479–488

Doshi, M. Y., Jain, A., & Patil, K. N. (2017). Performance Analysis of Solar Air Dryer for Multi Crop Drying Effect of Varying Air Mass Flow Rate. SSRN Electronic Journal. https://doi.org/10.2139/ssrn.3101275

Doymaz, İ. (2004). Convective air drying characteristics of thin layer carrots. Journal of Food Engineering, 61(3), 359–364. https://doi.org/10.1016/S0260-8774(03)00142-0

Ekka, J. P., Bala, K., Muthukumar, P., & Kanaujiya, D. K. (2020). Performance analysis of a forced convection mixed mode horizontal solar cabinet dryer for drying of black ginger (Kaempferia parviflora) using two successive air mass flow rates. Renewable Energy, 152, 55–66. https://doi.org/10.1016/j.renene.2020.01.035

Motevali, A., Minaei, S., Khoshtaghaza, M. H., & Amirnejat, H. (2011). Comparison of energy consumption and specific energy requirements of different methods for drying mushroom slices. Energy, 36(11), 6433–6441. https://doi.org/10.1016/j.energy.2011.09.024

Natalia, S. V., Mauricio, C., Hugo, A. M.-C., & Hugo, F. L. (2018). Drying uniformity analysis in a tray dryer: An experimental and simulation approach. Advance Journal of Food Science and Technology, 15(S), 233–238.

Patel, Y., Naraian, R., & Singh, V. K. (2012). Medicinal properties of Pleurotus species (oyster mushroom): A review. World Journal of Fungal and Plant Biology, 3(1), 1–12.

Raj, J., Ansari, M. I. A., Rai, P., & Prasad, G. (2013). Optimization of drying conditions of button mushroom (Agaricusbisporous). Journal of Research, 25, 36–40.

Sánchez, C. (2010). Cultivation of Pleurotus ostreatus and other edible mushrooms. Applied Microbiology and Biotechnology, 85(5), 1321–1337.

Shukla, S. (2011). Condenser temperature Correspondence to Author: 2(12).

Singh, S. K., Narain, M., & Kumbhar, B. K. (2007). Drying kinetics of button mushroom in fluidized bed. Journal of Agricultural Engineering, 44(1), 69–75.

Sutar, P. P., & Prasad, S. (2008). Microwave drying technology-recent developments and R&D needs in India. Proceedings of the 42nd ISAE Annual Convention, 1–3.

Walde SG, Velu V, Jyothirmayi T and Math RG 2006 *J. Food Eng.* **74** 108-15

Waluyo *et al* 2019 *IOP Conf. Ser.: Mater. Sci. Eng.* **633** 012045

Yapar, S. Ş. Helvaci & S. Peker (1990) Drying Behavior of Mushroom Slices, Drying Technology: An International Journal, 8:1, 77-99, DOI: 10.1080/07373939008959865

Teklit, G. A. (2015). Chemical composition and nutritional value of the most widely used mushrooms cultivated in Mekelle Tigray Ethiopia. Journal of Nutrition & Food Sciences, 5(5), 1.

Toledo, R. C. C., Carvalho, M. A., Lima, L. C. O., Vilas-Boas, E. V. de B., & Dias, E. S. (2013). Measurement of β-glucan and other nutritional characteristics in distinct strains of Agaricus subrufescens mushrooms. African Journal of Biotechnology, 12(43), 6203–6209. https://doi.org/10.4314/ajb.v12i43

HARMONIZATION OF ENERGY METERS PARAMETERS: CASE STUDY KENYA POWER

Charles Ndung'u[1*]; Kahoro Wachira[2]

[1]Sales Department, Kenya Power, Author Email: charlesndungu@kplc.co.ke

[2]Network Department, Kenya Power, Author Email: engkahorowachira@gmail.com

[*]Corresponding Author

Abstract

Complains of electricity bill discrepancies, mainly from large power end users, are common phenomenon whenever there is a new model/type of energy meter that retrofits the old energy meter. Energy meter retrofitting often occurs when there is need for advancement of metering technologies, as it has been observed in recent time, for example smart meter, prepaid meter and advanced meter infrastructure (AMI) or when present meter fails (become faulty). It is noted that new energy meters do sometimes have different parameterizations from the previous installed energy meter due to the fact that they may be embedded with different measuring methods and folding (sampling) frequency. It is pertinent to mention that energy meter, also commonly referred as cash register, is the main source of revenue for an electricity distributing and retailing company. This paper provides profound way, that is, harmonization of sampling rate, meter register resolution and computation of power factor (PF) to reduce perennial complains from power end users after energy meter's retrofitting. It is observed that lack of standardization of metering parameters aforementioned has a myriad of negative effects on energy meter measurement. The results obtained from analyzed dataset obtained from sampled large power customers' energy meters who had lodged complains due to electricity bill 'anomalies' after the former meter was retrofitted, is evidence that there is need for the three aforementioned parameters to be standardized in meter specifications. This paper advises electricity retailing company to have the three parameters clearly specified in energy meter specifications to ensure uniformity in energy meter measurement from various types/models of energy meter procured from different suppliers.

Key words: Energy meter, apparent power, power factor, parameterization, meter resolution

1.0 Introduction

Electrical energy is the main enabler to a country's economic development. For this reason, the demand for the energy has risen in recent time, that is, increases day by day due to the rapid industrial growth and improvement of living standards of the modern societies. Furthermore, it also contributed by rapid population growth as stated in [1]. To measure accurately the electrical power consumed by end power users, an electrical energy meter is installed at point of common coupling (PCC) of power consumers. It is noteworthy mentioning that electrical energy meter forms a link between the distribution or retailing utilities and power consumers. In this regard, having an accurate meter over a wide range of loads and ambient conditions for a long period of time cannot be emphasized.

Electricity as a source of energy has been in existence over a century and has evolved tremendously over this period. The electro-mechanical energy meters, that uses Ferrari principle, were the first energy meter to be deployed to measure electrical energy consumed by power end users. In the

advent of static (solid) and microprocessor energy meters in early 1970, electro-mechanical meters have recently been retrofitted by many electrical distribution companies. There are several reasons that have accelerated the retrofitting of electro-mechanical energy meters to static (digital) energy meters, which among them include;

i. No moving parts in electronic energy meter hence tampering is difficulty or not possible
ii. Microprocessors introduces multi-rate tariffs and anti-fraud measures such as sending of alarm events
iii. Can easily be linked to communication network for automatic meter readings, demand management among other functionalities
iv. High accuracy with high precisions thus suitable for bulk metering
v. Easy to read (light emitting diode (LED) display) and calibrate, no linearity problem, programmable and light weight.

This study explores digital electrical meter concept and versatile parameters that should be harmonized by power retailing utilities, taking Kenya Power as a case study. The subsequent section gives similar studies that have been carried out on energy metering relevant to this research study.

2.0 Objectives of the study

The main objective of this study is to explore impacts of retrofitting energy meter both to power end users and distribution electricity companies.

The specific objectives are as outlined below;

i. To establish energy meter divergence parameters and their impacts in energy measurement
ii. To identify the mitigation measures to avert perennial complains after energy meter retrofitting

3.0 Literature review

Digital energy meters have evolved immensely over the time. The smart and prepaid meters are the recent energy meters generation. As stated by Thanesis et al [2], smart meters deliver significant benefits to both consumers and power utilities. They are, further known to sustain energy management and increases security of energy supply.

In this content, digital meters are made up of three main function blocks: input transducers, signal processors and output transducers. Figure 1 shows a systematic diagram of a typical modern digital energy meter [3].

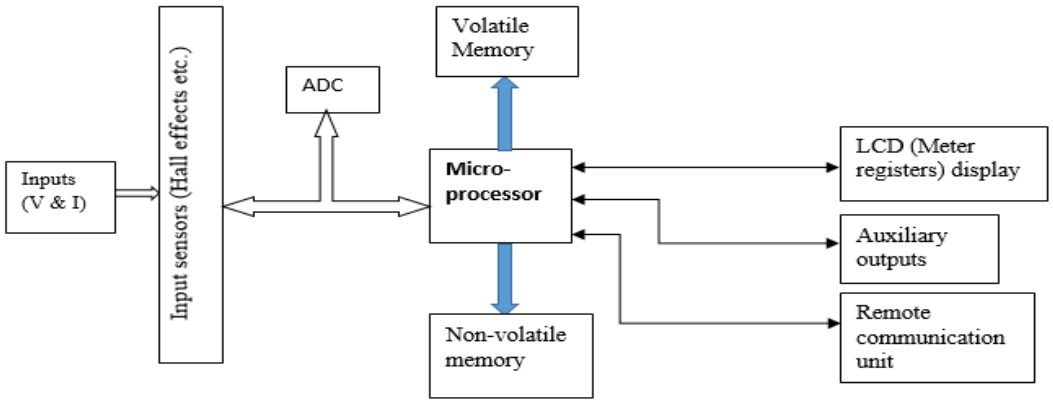

Figure 1: Typical structure of a modern digital energy meter

Blondel theory states that total power can be measured with one less Wattmeter than the number of wires in the system, that is, number of Wattmeter = M - 1, where M, is the number of wires [4]. There are two categories of energy meters; single phase and three phase meter. The latter are mainly installed at large power end users and for bulk metering such as at power generation stations and primary substations. On the other hand, single phase meters are installed at small commercial and domestic consumers' premises. Three phase electricity energy meters are further subdivided into low voltage and high voltage connected meter. The latter uses both current and voltage transformation, also referred as non-self-contained energy meter, which can be wired as three phase, three wire or three phase, four wire configuration. A systematic diagram of wiring of three phase, four wire configuration is as shown in Figure 2 [5].

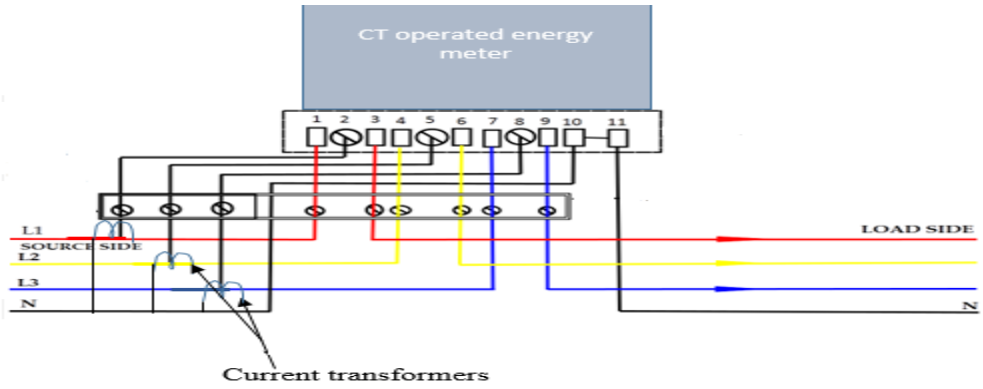

Figure 2: Wiring of a three phase, four wire energy meter for large power consumers

Three phase meters have intrinsic features that need to be standardized to ensure harmonization of parameters (demand, energy, PF etc) measured by the energy meter. This is because, currently, there is proliferation of different types of energy meter in the market that measure power parameters differently. According to Michel et al [3], the concept of apparent power (AP) and power factor as measure of system power delivery capability are over a century old but are yet to be defined in one general, rigorous, precious and acceptable ways. The Authors further stated that the computation of instantaneous power (vi) and average energy ($\int vi\ dt$) measured over a selected period, is widely acceptable globally. Many studies have shown that a system that is not balanced (voltage and/or current) and contains non-sinusoidal (harmonic pollution) waveforms, apparent power and effective power factor are different for various meter types/models. Therefore, need to unify energy meter measurands cannot be underestimated. By so doing, it averts consumer complains after energy meter retrofitting. This study explores these inherent divergence energy meter parameters in-depth. The parameters explored include; sampling rate, meter register resolution and computation of power factor. The subsection under elaborates each of this parameter.

3.1 Intrinsic energy meter parameters

The inherent energy meter parameters under the consideration and how they affect the energy meter measurements are described hereunder.

(a) Meter sampling rate

Electronic meters perform discrete sampling of instantaneous voltage and current values. It is therefore possible to discriminate fundamental, dc and harmonic components in the system as shown in Figure 2 [4].

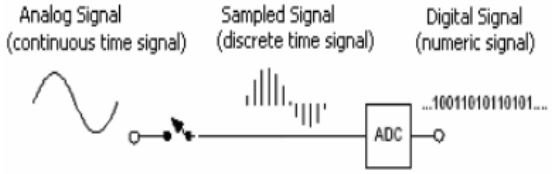

Figure 2: Analog to Digital Converter

As it can easily be seen in Figure 2, continuous (analog) signals are converted into discrete (numeric) signals by use of an analog to digital converter (ADC).
Nyquist (folding) frequency determines the highest harmonic frequency that can be measured (sampled). The basic rule of sampling theory states that the sampling rate must be at least twice the highest frequency content of the signal [6]. The Nyquist frequency for the maximum frequency to be sampled is given by equation (1);

$$N_s \geq 2F_{max} \quad (1)$$

Where, N_s is the sampling frequency, and F_{max} is the desired maximum frequency to be sampled.

For power triangle method ($S = \sqrt{(P^2 + Q^2}$), where S is the apparent power (AP), P is the real power and Q is the reactive power, input signals (V_{rms} and I_{rms}) are sampled as per equation 2 and 3, respectively.

$$V_{rms} = \sqrt{\frac{1}{N}\sum_{n=1}^{N} v_n^2} \quad (2)$$

$$I_{rms} = \sqrt{\frac{1}{N}\sum_{n=1}^{N} i_n^2} \quad (3)$$

Where; V_{rms} is the root square Voltage, I_{rms} is the root square Current, v_n is the instantaneous voltage, i_n is the instantaneous current, N is the maximum sampling rate, and n is the least sampling rate
This therefore implies that the higher the sampling frequency, the higher the apparent power sampled (V_{rms}* I_{rms}) as more harmonic energies are recorded by the meter, hence low effective PF (Eqn. 5) recorded by the energy meter. Another method deployed by some meter manufacturers is as shown in equation (4).

$$S^2 = v_1^2 i_1^2 + v_1^2\left(\sum_{h=2}^{hmax} i_h^2\right) + i_1^2\left(\sum_{h=2}^{hmax} v_h^2\right) + \left(\sum_{h=2}^{hmax} i_h^2\right)\left(\sum_{h=2}^{hmax} v_h^2\right) \quad (4)$$

Where; S is the apparent power, and h is the harmonic order

A closer look at equation (4) reveals that an energy meter with high sampling rate records high apparent power compared with an energy meter sampling input signals at low folding frequency. It's for this reason that power utility opt to define the maximum harmonic order that energy meter need to capture, by defining the sampling rate supplier design the meter, for uniformity in AP and PF measurement.

(b) Meter register resolution

This defines the minimum steps the register display increment, that is, the smallest units that energy meter can display. There are incidences that likely to cause significant decline in energy consumptions for large power users which include but not limited to; Depletion of raw materials, Loss of market shares hence low sale/demand of product/s, Political interferences and Change of adventure/business. As result, the aforementioned reasons may cause large power consumer's monthly energy and demand to drop marginally. If energy meter resolution is not harmonized, as noted in [12], can cause measurement discrepancies as explained in subsection of this paper.

(c) Power factor computation

Power factor, as per IEEE 1459-2010, is defined as the ratio between the energy transmitted to the load over maximum energy that could be transmitted where the line losses are kept the same [3]. It is usually computed as per equation (5) as a ratio of real power and apparent power.

$$\text{PF} = \frac{P}{S} \qquad (5)$$

Where; P is active power and S is apparent power
The reference [12], define the power factor as ratio of active power to maximum apparent power. Noteworthy to mention is that apparently power can be computed either by use of Arithmetic or vector (geometric) methods as explicitly detailed in [2 and 3]. Further, the apparent power highly depends with computation method of reactive power. There are several methods that can be used in computation of reactive power, which are namely: current displacement method of 90^o, voltage displacement method of 90^o, voltage displacement method by derivative and voltage displacement method by integration. It can also be computed using Fourier series method that calculates all the harmonic orders and fundamental frequency energies. Power utility may choose to bill a displacement power, that is, cos θ between voltage and current or effective PF that is computed as ratio of month consumed energy and apparent energy ($\frac{\text{kWh}}{\text{kVAh}}$). When utility consider the former PF, there is still need to ensure the measurement quadrants are well defined in the meter specification. The energy meter quadrants are as shown in Figure 3.

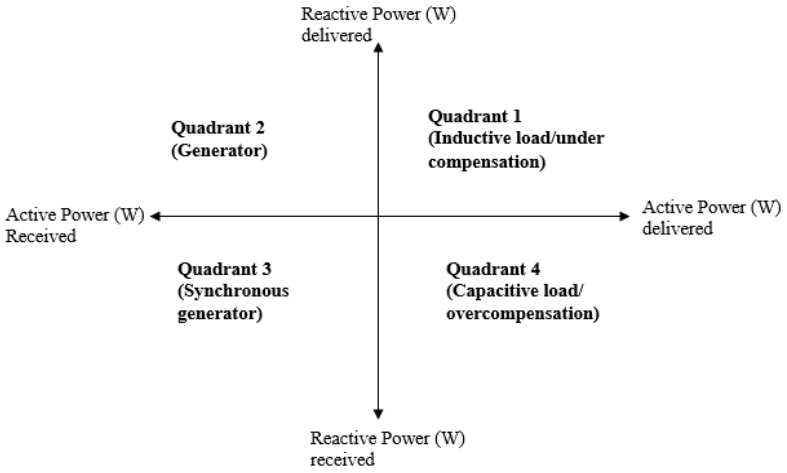

Figure 3: Energy meter measurement quadrants

As it can vividly be seen in Figure 3, meter measuring only in quadrants 1 and 2, records a unity power factor when power end user over-compensates the reactive power. Over-compensation of reactive power is known to increase grid voltage profile and technical losses.

4.0 Research Methodology

This research study involved analyses of large power consumers' data collected from sampled energy meters installed at large power consumers that had lodged complaints of billing discrepancies after meter retrofitting as well as data obtained from power quality logger. It is pertinent to note that large power meters data gathered were online data and billing system for online and non-online large power meters, respectively. The data logger was installed at site for fortnight at sampling data rate of 5 minutes.

5.0 Data Gathered Analyses and Discussion

The dataset obtained from energy meters installed at same PCC is shown in Table 1.

Table 1: Two different meters type installed at same PCC captured monthly PF

kVA	kW	Computed PF	Type of meter
151	149	0.987	Type A
1044	946	0.906	
964	946	0.981	
996	986	0.99	
1029	1012	0.983	
947	940	0.993	
968	965	0.997	
1140	963	0.845	Type B
1200	960	0.8	
1180	980	0.831	
1220	1000	0.82	
140	100	0.714	
120	80	0.667	

It is clearly seen that meter type A captured good PF while type B meter recorded poor power factor. This is assumed is due to dissimilar computation method of reactive power that could be different in the two energy meters. It is further noted that meter type A has good demand (kVA) resolution compared to energy meter type B. It is noteworthy mentioning that the two meters demand were read at different months, but installed at same common point of connection. Meter A was read manually while meter B was remotely read.

The failure of not specifying the meter resolution can vividly be seen in Table 2. One can easily note that the smallest demand increment for this particular energy meter, (where primary voltage is 66 kV), is 120 kVA. It can easily be assumed, from Table 2, that the consumer was non-operational for several months, hence zero demand. However, this is not the case as it was contributed by the minimum step increment in demand register, that is, 120 kVA. When the

demand was less than 120 kVA, meter records 0 kVA. Furthermore, it is also possible that the large power end user demand could have been 239 kVA, however, the meter records the maximum demand as 120 kVA. The premise is loss of the revenue to the company. This was noted for all large power users with primary voltage of 66 kV and above.

Table 2: An energy meter recorded maximum monthly demand

Billing Date	Apparent Demand(kVA)
2021-05-01	120
2021-06-01	0
2021-07-01	120
2021-08-01	120
2021-09-01	120
2021-10-01	0
2021-11-01	0
2021-12-01	0
2022-01-01	0
2022-02-01	120
2022-03-01	0

Another complain of poor power factor, after energy retrofitting, reported by a large power end, with maximum active demand of 60 kW, user was examined. After thorough investigation, it was established to be caused by high current harmonic pollution at customer PCC. The large power consumer was noted to have many non-linear loads; computers, printer and photocopiers. The total current harmonic distortion levels at customer site were as depicted in Table 3 as per power quality logger captured data.

Table 3: Harmonic pollution at customer premises

	THDi (L1)	THDi (L2)	THDi (L3)
Avg (%)	23.30	18.99	23.22
Max (%)	70.09	61.17	69.70

As per the results obtained from a power quality analyzer, the displacement power factor was above 0.9, however, the effective PF was noted to be less than 0.9 which was computed factoring harmonic energies, caused power factor surcharge as stipulated [11]. It was inferred, after data analyses that the two meters had different sampling rates. This is an evidence that shows that specifying the Nyquist sampling rate in the energy meter specification is paramount to unify apparent power measurement.

6.0 Conclusion

This paper has explicitly explored the key energy meter parameters that the distribution and retail utility need to have them clearly documented in energy specification. This is to avert perennial complains or loss of revenue after retrofitting the energy meter due to various reasons stated in this paper. The intrinsic parameters discussed are meter sampling rate, energy meter resolution and computation of power factor. Evidences on how each of the parameters has contributed negatively to large power customer and power utility are presented in this paper.

7.0 Recommendations

From the study carried out, the author recommends that power utilities to clearly specify the aforementioned parameters (sampling rate, meter resolution and power factor computation) in meter specification. This is because currently there is influx of the many suppliers of the energy meters in the market that have different computation methods of apparent power that may have adverse effects after meter retrofitting. In so doing, there is likely to have seamless transition after retrofitting energy meter type/model, hence reducing complains from large power end users.

References

[1] Guilherme L. X., Gabriel M., Eduardo T., Hélio R. J. da Silva, Lara L. B., Raphael F. B. de Oliveira, Rodrigo N. C. & José R. M. Jr. (2020). 'An update on the performance of reactive energy meters under non-sinusoidal conditions', *Springer – Verlag*, German , Vol. 3.

[2] Thanesis V. (2019, March 18-20). '*Anomaly detection in smart meters'*, CIRED [14th conference] Slovenian electrical power engineers.

[3] *IEEE 1459-2010*: *IEEE standard definitions for the measurement of electric power quantities under sinusoidal, non-sinusoidal, balanced or unbalanced conditions*

[4] Capisca C. (2007, October 13-15). *Digital sampling method in the measurements of electrical power and energy'*, [conference proceedings paper]. 9th WSEAS Int. Conf. on Mathematical Methods and Computational Techniques in Electrical Engineering, Arcachon

[5] Ndung'u C., Nderu J., & Ngoo L., (2013). *'Mitigating of harmonic distortions and low power factor in unbalanced three phase system using fuzzy logic controller*,' [MSC Thesis JKUAT].

[6] M. Melengret and C. Gaunti, (2020). 'Active currents, power factor and apparent power for practical power delivery systems', Article DOI: 10.1109/ACCESS.2020.3010638

[7] The Energy Act. (2019). *No. 1*

[8] S. Electronic, Power, Test and Measurement, (2020) '*How to measure electrical power'*.

[9] Ndungu C. (2021, September 16 - 17), '*Analysis and evaluation of ct transformation error for non self-contained smart meters installed in smart cities*,' [conference paper], Energies, Southampton, UK

[10] Bhattarai P. (2016). *'Powers and Compensation in Three-Phase Systems with Nonsinusoidal and Asymmetrical Voltages and Currents'*, [PhD Dissention Louisiana State University and Agricultural and Mechanical College]

[11] Kenya Gazette Notice. (2018). *Vol CXX –NO.91*.

[12] KPLC specifications. (2014). *Outdoor large powering metering solution*.

EFFECTS OF PLY THICKNESS ON BURSTING STRENGTH IN OVERWRAPPED COMPOSITE HIGH-PRESSURE VESSELS

Nathan Mukala Numbi[1], Leonard Masu[2], and Patrick Nziu[3]

[1] Vaal University of Technology, Faculty of Engineering and Technology, Department of Industrial Engineering & Operational Management and Mechanical Engineering, Vanderbijpark, Andries Potgieter Blvd, 1911, South Africa ORCID: 0000-0002-9900-5295

[2] Technical University of Kenya, Faculty of engineering and the built environment, School of Mechanical and manufacturing engineering, Department of Mechanical and Mechatronic Engineering, Haile Selassie Avenue, P.O. Box 52428, Nairobi, 00200, Nairobi, Kenya. ORCID: 0000-0002-8544-6321

[3] Moi University, School of engineering, Department of Manufacturing Industrial & Textile Engineering, Eldoret, P. O. Box 3900 Eldoret, KENYA. ORCID: 0000-0002-5899-0700

Corresponding author email address: numbinathan@gmail.com

Abstract

This study investigated the effects of ply thickness on bursting strength in composite pressure vessels using analytical method. In this work, different range of ply thicknesses were analyzed to establish a more superior sustainable composite pressure vessel.

The analytical method was carried out using the Tsai-Wu failure theorem. The developed analytical equations were solved with Matlab 2016 software to determine the composite ply thickness. A total of 28 generated parts were created on two different profiles using different sizes of the vessel liner so as to determine the degree of resistance to bursting failure. Subsequently, the structural integrity of ply imparted into the design was analyzed at an optimal angle of 55º, oriented in both the negative and positive directions. The best ply thickness range was thereafter determined using a first ply failure approach. Additionally, the identified superior range of pressure vessel constituent was numerically validated using Abaqus/CAE software, to have a degree of reassurance on the results generated from Hashin failure criteria.

The generated results revealed no significant change in vessel strength between plies oriented in positive direction and those in the negative direction at different sizes of ply thickness. The validation of analytical results through numerical approach, yielded a comparable margin of error not exceeding 4 %. Based on the first ply failure theorem, it was therefore concluded that the

criteria closest to the Tsai Wu value of 1, that was recorded on the 5th and 6th models in both profiles, showed a considerable improvement in the structural design of the vessel.

The replacement of a single material cylinder with that of composite, can therefore be generated through a combination of liner and the best size thickness of both the ply and the shell, as in the case of carbon fibre laminate.

1. Introduction

A pressure vessel is a container manufactured with the purpose of holding liquid or gas at a pressure different from atmospheric environmental pressure (Nohan & Yaprapragada, 2000). Its purpose of storing high pressure, has an important influence on its design strength, playing a major role in preventing dangerous premature failure occurring on a vessel. Critical factors influencing its strength characteristic reside in the vessel structural integrity that gives the ability to sustain pressurized substance exerting a toll on the vessel surface. The effects of this pressure on the surface of the vessel may be resisted as long as its structure is made sufficiently reliable.

Depending on the sector in which the pressure vessel will be used, emphasis is made on the manufacturing material. Numerous pressure vessels are made of forged steel and rolled into a cylindrical or spherical storage container and their parts welded together (Choi, 2016).

To avoid challenges associated with steel materials, pressure vessels could be made of composites which is a combination of materials differing in their composition. The individual materials retain their identity when combined, as they do not dissolve or merge completely (Nohan & Yaprapragada, 2000). The overwrapped composite pressure vessels consist of an outer layer of continuous ply to carry the pressure load and an inner layer on which the outer layer is wrapped over to contain the liquid from leaking or minimizing the leakage (Nohan & Yaprapragada, 2000).

Extensive research has been done on composite pressure vessels since 1998 with intention of improving on the adversity encountered by cylindrical pressure vessels made of metallic material. Therefore, the development of composite materials to enhance vessel efficiency has exhibited high specific strength and a high specific modulus (Yarrapragada, 2012).

Numerous plies are considered as constituent for a composite, depending on the advantages they bring to the vessel. The most common material used in composites is carbon fibre, as it occupies

a large volume fraction in the composite and hence withstands the major portion of the load acting on it (Hendlmeier, et al., 2019).

The carbon ply is incorporated as a composite material for pressure vessels due to its high modulus and high strength properties (Yarrapragada, 2012). In addition, it has the advantage of having a low coefficient of thermal expansion and high fatigue strength. It is due to these benefits the carbon ply brings to the composite, which makes it a suitable material to deal with the effects of bursting failure of the vessel created by a strength reduction of its structural integrity (Alexander, et al., 2013).

Therefore, the design of an efficient and reliable pressure vessel with a high resistance to burst failure was generated by developing an improved overwrapping composite vessel. This design was constituted by a ply shelling a metallic liner to deal with strength reduction thus preventing its damage.

2. Methodology

This section entails determination of allowable ply thickness required in the generation of an improved overwrapped composite pressure vessel sustainable to bursting failure. A total of 28 geometrical parts were generated for two common industrial profiles designed in the form of a composite pressure vessel. With regard to strength optimization, these generated part-profiles were used to determine the effect of ply thickness oriented in the negative and positive direction. The analytical method was carried out using Tsai-Wu failure theory with generated equations solved using MATLAB software version 2016 in order to determine the mean thickness of composite pressure vessel and perform strength analysis. Afterwards, the analytical method was validated numerically by Finite Element Analysis using Abaqus software version 2016.

This section, therefore, covers the approach adopted in the reinforcement of the cylinder with the capability to resist failure due to bursting. Conversely, the reinforcement could be achieved by increasing the wall thickness to resist the load applied to the body structure. Hence, this designed approach (of composite pressure vessel) should improve strength comparatively to the stainless-steel vessel.

2.1 Selection of geometric sizes of stainless-steel pressure vessels commonly used in the industry to be studied

Two industrial vessel profiles (see figure 1) were used to determine the impact of ply thickness of a conceived composite pressure vessel. Except for wall thickness, each of the geometrical dimensions of the two profiles considered in this study were those from common industrial vessel dimensions (Daniel & Ishai, 2006) made from stainless steel material.

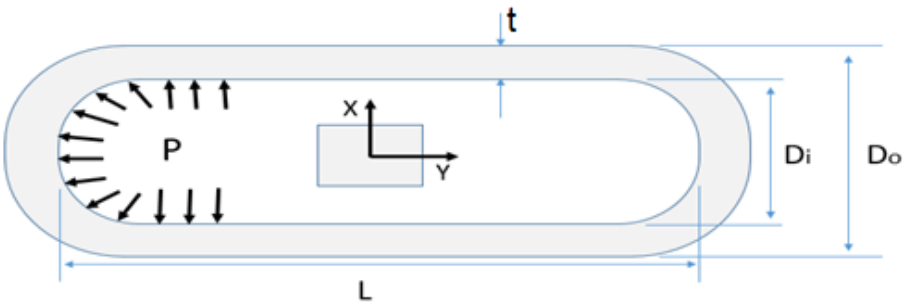

Figure 1: Stainless steel pressure vessel profile

Where:

t = Thickness of stainless-steel pressure vessel

D_i = Inner diameter of stainless-steel pressure vessel

D_o = Outer diameter of stainless-steel pressure vessel

P = Internal pressure

The stainless-steel pressure vessel was chosen to be of length L and internal diameter D_i on which an internal pressure P was exerted. The respective magnitudes were taken as depicted in Table 1.

Table 1: Stainless steel pressure vessel profiles (Daniel & Ishai, 2006)

Cross-section description	Profile 1	Profile 2
Vessel length	0.203 m	0.406 m
Inner diameter D_i	200 mm	400 mm
Thickness t	6.7 mm	13.4 mm
Internal pressure	8 MPa	8 MPa

Equation 1 shows the Von Misses theorem, which was used to calculate the expression for the allowable thickness as illustrated in Equation 2. For more clarity, the derivation process of this equation is shown in Appendix A. Therefore, with a predetermined pressure, inner diameter and length dimension, the allowable wall thickness t required to withstand the applied pressure on a stainless steel vessel was generated from Equation 2 (Kamal, et al., 2016). The Von-Mises theory approach adopted was purposely used to generate sustainable stainless steel wall thickness t (see table 3.1) for profiles 1 and 2.

The purpose of this specific approach was to emphasize the importance of ply as constituent. Besides, exhibiting the strength aspect through a comparison of sustainable stainless-steel vessels and that of composite pressure vessels.

$$\sigma_{max}{}^2+\sigma_{min}{}^2-\sigma_{max}\sigma_{min}=\left(\frac{S_{yt}}{S}\right)^2 \quad (1)$$

Where:

σ_{min} = Minimum principal stress

σ_{max} = Maximum principal stress

S_{yt} = Tensile yield strength of stainless steel

$$t=\frac{\sqrt{3}PD_iS}{4S_{yt}} \quad (2)$$

Where:

t = Stainless steel allowable wall thickness

P = Internal pressure

D_i = inner dimeter of stainless steel pressure vessel

S = Safety factor (S = 2)

Upon application of Equation 2 on the two industrial stainless steel pressure vessels with material properties shown in Table 2, calculated allowable structural wall thickness of 0.0134 m

and 0.0067 m for a required pressure of 8 MPa were generated. This determined allowable thickness was therefore the base upon which the variation range of the composite pressure vessel models were generated for this study.

Table 2: Properties of stainless steel (Daniel & Ishai, 2006)

Properties	Value
Young's modulus, E	193 GPa
Density, ρ	7750 kg/m^2
Poisson's ratio, v	0.27
Tensile yield strength, S_{yt}	207 MPa
Tensile ultimate strength, S_{ut}	586 MPa

2.2 Conversion of the geometric sizes of a selected stainless steel pressure vessels to equivalent overwrapped pressure vessels

With selected stainless steel pressure vessel requiring improvement strength resistance to bursting failure, reinforcement was done through conversion of the vessel structure. These 2 profiles were transformed from stainless steel cylinder to composites pressure vessel by conversion of wall thickness from metallic to composite as seen in Figure 2.

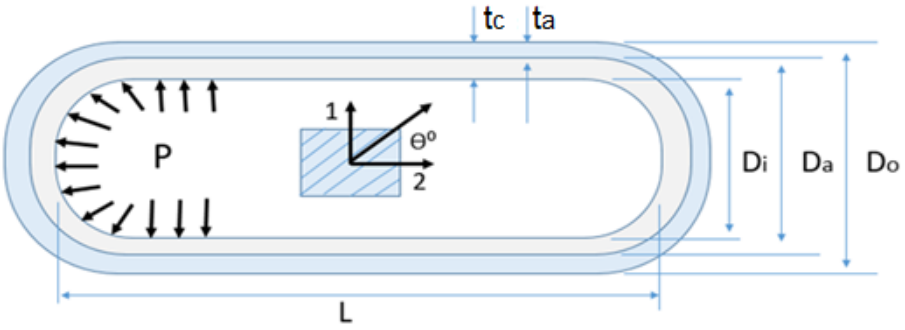

Figure 2: Composite pressure vessel profile

Where:

t_c = Thickness of composite pressure vessel

t_a = Carbon ply shell thickness

D_i = Inner diameter of composite pressure vessel

D_a = Inner diameter of carbon ply shell

D_o = Outer diameter of carbon ply shell

Θ^0 = ply angle orientation

P = internal pressure

2.3 Determination of the suitable range of liner thickness of composite pressure vessel

The allowable thickness determined for the two profiles, being 0.0067 m and 0.0134 m (structural wall aimed for improvement), were the base references, upon which the thicknesses of the composite pressure vessels were generated. Hence, taking the liner of the composite as a variable factor of the study, the determined thickness (stainless steel vessel) were halved. One portion was considered as a structural liner and the other one was replaced by a sustainable overwrapping composite shell.

The size variation of the liner for profile 1 ranged from 0.00335 m as a minimum and 0.00670 m as a maximum. While that of profile 2 ranged from 0.0067 m to 0.0134 m for minimum and maximum size, respectively. The increment between parts for the liner variation was therefore taken as 0.000558 m and 0.001117 m for profiles 1 and 2, respectively. These increments were calculated from equation 3 (Sonnen., 2004).

$$i = \frac{t_{max} - t_{min}}{n-1} \quad (3)$$

Where

i = Increment

t_{max} = Maximum liner thickness

t_{min} = Minimum liner thickness

n = Number of parts

A total number of 28 geometrical part profiles were developed in this research. Additionally, the angle of orientation adopted on all parts was kept at an optimal value of 55º (Hannus & Majak, 2003). This ply thickness determination was performed in both positive and negative directions for the two profiles as shown in Table 3.

Table 3: Liner geometrical thickness for ply portion of composite pressure vessel

Part Number	Orientation angel (º)	Profile 1 (mm)		Profile 2 (mm)	
		Positive	Negative	Positive	Negative
1	55	3.35	3.35	6.700	6.700
2	55	3.908	3.908	7.817	7.817
3	55	4.467	4.467	8.933	8.933
4	55	5.025	5.025	10.050	10.050
5	55	5.583	5.583	11.167	11.167
6	55	6.142	6.142	12.283	12.283
7	55	6.700	6.700	13.400	13.400

2.4 Determination of ply thickness of composite pressure vessel

The determination of ply thickness was done as per the following steps with the aim of generating a single-ply thickness with the strength properties required for an optimal design.

2.4.1 Analytical method

The analytical approach adopted in the study was “ply failure” due to a single layer of fibre (as ply) overwrapping the vessel. Hence, for such analysis, the stress generated in the structure was solely from the liner due to the mechanical load applied in the internal surface as pressure. Therefore, with the use of Matlab software version 2016 as a tool in this analytical process, the internal pressure effect expressed in the form of stresses were converted from the global to the principal axis fully depicting the required ply thickness.

For more clarity on the process adopted on this section, the steps adopted are shown in Figure 3. These steps led to the determination of the ply thickness for the numerous parts of profiles 1 and 2 investigated.

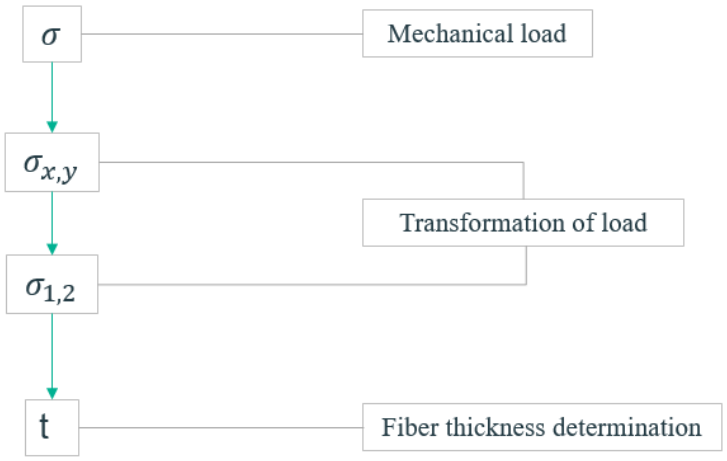

Figure 3: Steps for determining allowable ply thickness

2.4.1.1 Mechanical load application

The pressure applied on the internal surface of the vessel was used in this section, as the mechanical load acting on the entire composite constituted of liner and a single ply. The stress generated from this load of magnitude 8 MPa exerting pressure in the internal surface, was determined from Equations 4 and 5.

$$\sigma_x = \sigma_a = \frac{PD_i}{4\,t} \quad (4)$$

$$\sigma_y = \sigma_h = \frac{PD_i}{2t} \quad (5)$$

Where:

σ_a = Axial stress

σ_h = Hoop stress

P = Internal pressure

t = liner thickness

The stresses used in this step were determined as depicted from internal radius r and a thickness t corresponding to the different liner thickness as shown in Table 3. Eventually, these generated stresses used on the internal surface of the single ply led to the determination of the said lamina ply.

Therefore, considering the first model of profile 1 with a radius of 0.2 m and liner thickness of 3.35 mm, the stresses used for this particular case were 238 MPa and 477.6 MPa, in the longitudinal and hoop directions, respectively.

2.4.1.2 Transformation of load from global to principal axes

The stresses used in the analyses and generation of the allowable ply thickness were of a longitudinal and hoop nature. The radial stress on the other hand, also expressed in the global axes system was neglected in this analysis as the designed vessel was thin-walled high pressure vessel (Daniel & Ishai, 2006).

The analysis leading to the ply thickness generation was done on the principal axes as ply lamination was influenced by the optimal angle of orientation taken as 55º. Therefore, the stresses applied as mechanical load of a longitudinal and hoop stress nature were converted with the transformation relationship of Equation 6, by substituting angle θ by 55º in case of positive and negative directions, of the models.

$$T=\begin{bmatrix} C^2 & S^2 & 2CS \\ S^2 & C^2 & -2CS \\ -CS & CS & C^2-S^2 \end{bmatrix}, C=cos\theta\ , S=sin\theta \quad (6)$$

With the transformation relation determined, the respective models' principal stresses were then generated from Equation 7 for analysis to be conducted on and the directional load effect exhibited. Through this step, the use of Matlab software was beneficial in the analytical process of conversion from global to the principal axes with a higher accuracy level when compared to the length of time that hand calculations would take with the possibility of errors being apparent.

$$\begin{Bmatrix} \sigma_1 \\ \sigma_2 \\ \tau_6 \end{Bmatrix} = T \begin{Bmatrix} \sigma_x \\ \sigma_y \\ \tau_s \end{Bmatrix} \quad (7)$$

2.4.1.3 Calculation of ply thickness

The principal stresses generated from the transformed load applied on the global axes through ply thickness determination were considered influential to the single-ply dimension. Therefore, the principal stresses σ_1 and σ_2 were used to determine the corresponding ply thickness to the numerous geometrical liner thickness of profiles 1 and 2.

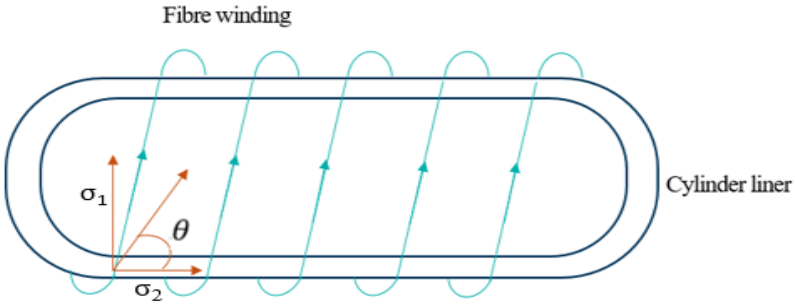

Figure 4: Helical winding of ply over the cylinder liner

As displayed in Figure 4, the ply were aligned at an angle θ . The optimal angle for this study was 55º. The analysis took into account the helical pattern of lamination with principal stress σ_1 in order to generate thickness t_1 through this sequence. With the hoop pattern on the other hand, a thickness, t_2 was generated with the application of principal stress σ_2 (Takalkar., 2016).

Therefore, with internal pressure P of 8 MPa and a radius r of 0.1 m and 0.2 m; respectively for the 1st and 2nd profiles, the calculation of thickness in the helical direction wound in the cylinder and the dome part was given by using Equation 8 (Takalkar., 2016).

$$t_1 = \frac{Pr}{2\sigma_1 cos^2\theta} \quad (8)$$

In the hoop direction, the ply thickness around the cylinder was also determined by the use of Equation 9 (Takalkar, et al., 2016).

$$t_2 = \frac{Pr}{2\sigma_2}(2 - tan^2\theta) \quad (9)$$

The ply thickness t_f given in Equation 10 (Shafique & Khan, 2010), was generated by the combination of the individual directional thickness t_1 and t_1 with consideration of the volume

fraction v_f of magnitude 0.0063. This developed analytical equation was solved using Matlab software version 2016 due to its availability and ability to solve matrices problems.

$$t_f = \frac{t_1}{v_f} + \frac{t_2}{v_f} \quad (10)$$

2.4.1.4 Determination of sustainable range of ply thickness

With the consideration of a single ply overwrapping the vessel liner, an expected failure of the composite occurred due to the unsustainability of the vessel. The Tsai-Wu failure criteria of Equation 11 (Daniel & Ishai, 2006), was used to determine the range at which the thickness of ply generated for models of profiles 1 and 2 were less susceptible to failure and, hence considered as optimal.

$$f_1\,\sigma_1 + f_2\,\sigma_2 + f_{11}\,\sigma_1^2 + f_{22}\,\sigma_2^2 + f_{66}\,\tau_6^2 + 2f_{12}\,\sigma_1\,\sigma_2 = 1 \quad (11)$$

The principal stresses (σ_1, σ_2& τ_2) used in the equation of Tsai-Wu were the ones generated from the different models on the transformation step. In addition, the different coefficients used in the Tsai-Wu criteria were calculated using Equation 12 (Daniel & Ishai, 2006), taking into account the value of ply strength property from Table 5.

$$f_1 = \frac{1}{F_{1t}} - \frac{1}{F_{1c}}\ ,\ f_2 = \frac{1}{F_{2t}} - \frac{1}{F_{2c}}\ ,\ f_{11} = \frac{1}{F_{1t}F_{1c}}\ ,\ f_{22} = \frac{1}{F_{2t}F_{2c}}\ , \quad (12)$$

$$f_{66} = \frac{1}{F_6^2}\ , f_{12} = -\frac{1}{2}\sqrt{f_{11}f_{22}}$$

The properties of carbon ply used in this study are tabulated in table 5

Table 5: Property of carbon fibre (Daniel & Ishai, 2006; Eisenmann & Elahi, 2007)

Properties	Value
Density, ρ	1540 kg/m^3
Longitudinal modulus, E_1	147 GPa
Transverse modulus, E_2	10.3 GPa
In-plane shear modulus, G_{12}	7 GPa
Out-of-plane shear modulus, G_{13}	7 GPa
In-plane Poisson's ratio, v_{12}	0.27

Out-of-plane Poisson's ratio, v_{23}	0.54
Out-of-plane Poisson's ratio, v_{13}	0.27
Fibre volume fraction, v_f	0.0063
Longitudinal tensile strength, F_{1t}	2280 MPa
Transverse tensile strength, F_{2t}	57 MPa
Transverse shear strength, F_5	65 MPa
In-plane shear strength, F_6	71 MPa
Longitudinal compressive strength, F_{1c}	1725 MPa
Transverse compressive strength, F_{2c}	2280 MPa

Therefore, the failure criteria of these numerous models were compared to the sustainable Tsai-Wu criteria of a value of 1. The value closer to 1, represented sustainability, and was considered optimal from this failure criteria. Therefore, it yielded the range of plies that were less susceptible to bursting failure on profiles 1 and 2 (Kim & Chol, 2001).

2.4.2 Numerical method

The generated ply thickness from the previous method was numerically validated in this study for the two selected profiles thicknesses. Therefore, the approach adopted for this numerical validation was made through Finite Element Analysis using Abaqus 2016 software as a tool for the design of numerous models generated from the variation of the composite liner on both profiles.

In summary, this validation method was done with a view of emphasizing the effect of the ply thickness on the composite, based upon the "first ply" failure analysis (failure criteria of single ply layer based on Tsai-Wu sustainability equation). Hence, through comparison of data of the simulated models to the one numerically generated, validation depicted the failure criteria for all considered ply thicknesses and confirmed the one least susceptible to bursting being closer to the Tsai-Wu criteria of value 1. The following eight modelling steps of Abaqus software were followed.

2.4.2.1 Part creation

The Abaqus/CAE software adopted for this study was used to create the vessel part within the software. No part was exported for the modelling process as Abaqus can adopt and analyze a part created in different software. The part module was used within Abaqus. The dialogue box "create

part" was selected, and Abaqus opened the option allowing the description of the created part. The modelling space which was used for this study was kept at 3D default and deformation type. This study selected the base feature for a shell shape with extrusion type. The approximation size was increased to 600 mm to accommodate the design dimensions. The units used were millimeters. The first part had dimensions of 203 mm length and 200 mm diameter, whereas the second part had measurements of 406 mm length and 400 mm diameter.

Note: with creation of part in millimeters as per Abaqus default unit, stresses and pressures were kept in MPa throughout the modelling and simulation (MPa = N/mm^2).

2.4.2.2 Property module

Upon selecting the property on the module toolbar, Abaqus allowed the assignment of material property by clicking on the "create material" option. Therefore, for the single ply material under mechanical elasticity, elastic material behavior was selected. The type of elasticity was set to "Engineering Constraints" with carbon ply property imparted from table 5. On the other hand, the liner material was created with mechanical elasticity set to isotropic with Young's modulus of 193 GPa and Poisson's ratio of 0.27.

With the task of validation being based on the failure criteria, the Hashim criteria option in Abaqus software was used to compare with criteria 1 of Tsai Wu's. Furthermore, under the mechanical option, the damage for fibre-Reinforcement Composite was selected and filled with properties of ply as shown in Table 5.

On the site bar, the "create composite layup" was used next with the initial ply set at 2 for this task, to account for the liner and the single ply with element type set at the conventional shell. The layup orientation was set up to discrete (for undefined normal and primary axis option), with its definition done by editing the surface after clicking on the composite surface. With this performed, orientation was done for the normal axis. Therefore, the primary axis direction definition was done by clicking on the closest edge of the composite.

The layup was followed by the region selected on the composite surface, as displayed in Figure 5. The materials created were then assigned to the liner and the ply with their respective thickness. For instance, in the case of the first model of profile1, dimensions of 3.35 mm of liner and 0.1594

mm of ply were used. The directions of constituents were finally imparted in the rotation angle column with 0º for liner and 55º for the ply.

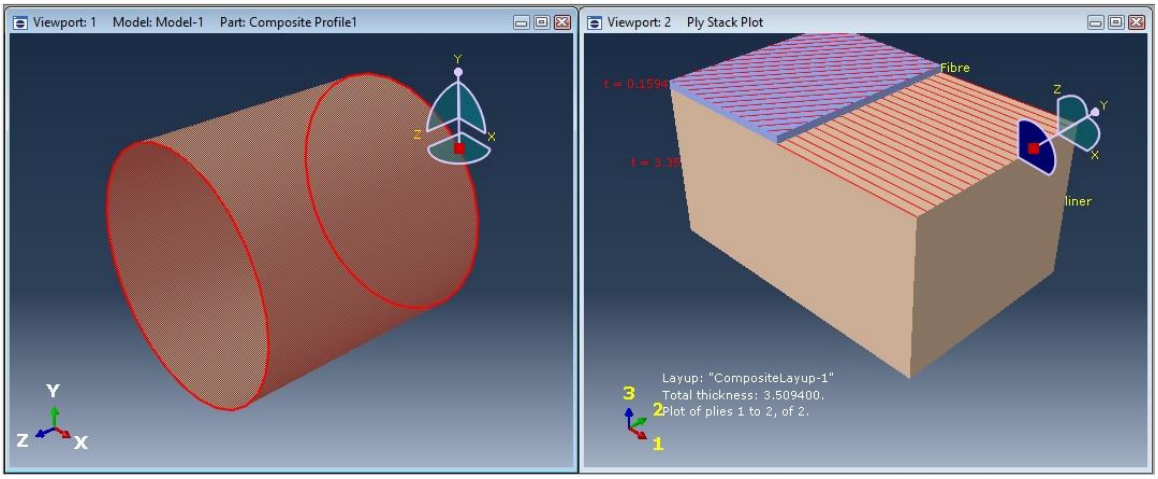

Figure 5: Composite lay up

2.4.2.3 Assembly module

Under the assembly part module, the instance type was kept to “dependent” (the default setting for the application of the original part mesh to the entire dependent instances of the part). This setting was selected as the entire model was designed as a single composite though made of different constituents. Therefore, the whole vessel was considered as a part in the same coordinate (allowing the meshing of the part only once).

2.4.2.4 Step module

In Abaqus software, the initial step is usually already created and cannot be modified. For this section, internal pressure, endcap, and boundary condition needed to be considered. Therefore, additional steps were made on static general, which were assigned to the load process and later on the boundary condition of the part.

The surfaces on which loading was to be applied were also created through this module under the surface manager of the tool option. In addition, the field output request was used with the domain set to “composite layup.” The output variable of stress components and invariants, total strain components and Hashin failure criteria for both ply and matrix in tensile and compression were selected. This allowed the determination of the failure result at the visualization step.

2.4.2.5 Load module

With internal pressure and endcap considered for this study, a pressure of 8 MPa was applied on the internal surface of the composite vessel with the selection of "pressure" as the mechanical load to be assigned on the set and the surface created. Longitudinal stresses were applied at both edges of the vessel with a magnitude of -113.98 MPa (refer to Equation 5) to simulate close ends effects.

2.4.2.6 Boundary condition

The boundary condition of the designed models was created on both sides of the cylinder upon selection of the "displacement/ rotation" boundary condition. This boundary condition was restricted in the rotation direction UR1, UR2 and UR3. This exception was made on the displacement of U1, U2 and U3 to allow freedom along the longitudinal and hoop direction of the respective axis X, Y and Z.

2.4.2.7 Mesh Module

On the mesh module, the global seeds option allowed the possibility of modification of the default approximate global size, which was kept at a set value of 28 due to the long computation time of the program when set lower.

The element type was selected from the top mesh toolbar as "shell family," with all the element controls kept at default. The geometrical order was linear with full integration. The mesh part was selected, and the model meshed as per the seed. A total of 154 elements were generated.

2.4.2.8 Visualization

With job creation selected on the access tool bar, the design created through Abaqus software with all composite constituent properties and mechanical loading imparted to it, the submission option allowed for the generation of a visualization result. The Hashin result of criteria 1 can be visualized at 75% average as the default setting and compared to the Tsai Wu theorem ones.

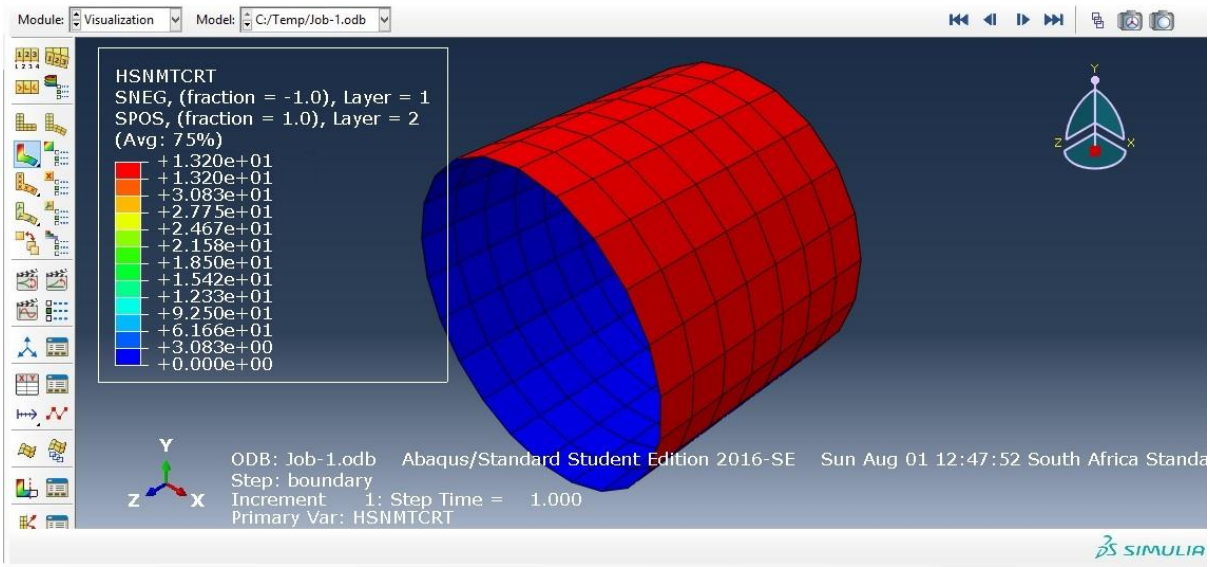

Figure 6: Visualization of overwrapping pressure vessel

3. Results and discussions

This chapter presents the results and discussions on the design of an improved composite pressure vessel composed of stainless-steel liner and carbon ply as influential factors to the integrity of the structure.

The effect of these influential factors and results generated from the methodology section, were represented in graphs and tables to emphasize on the sustainability of the composite structural integrity with aim of resistant to bursting failure. These analytical results were discussed and eventually verified through numerical approach of finite element analysis.

3.1 Analyses of ply thickness results

The results obtained from the analytical approach adopted in the ply thickness determination, were represented in Tables 6 and 7. These results ultimately generated the effects of ply incorporation over the metallic liner in the developing a sustainable composite pressure vessel resistant to failure with improved strength compared to a full metallic vessel.

On the other hand, a graphical representation of the ply thickness based on the hoop strength and the Tsai-Wu theorem was used to determine the maximum, minimum and or peak allowable value required in the analysis of range used for the combination and generation of a reliable improved composite pressure vessel.

3.1.1 Allowable ply thickness results

The analytical methodology adopted in the process of ply thickness determination led to the findings of the allowable ply size. Under the lease susceptibility failure, theorem referred to the Tsai Wu criteria, this required dimension used in the generation of improved pressure vessel sustainable to resist bursting failure, upon determination of the range detrimental to the integrity of the container. Therefore, as both profiles considered in this study had generated ply thickness in the positive and negative direction, the theorem mentioned earlier was also used to determine the sustainable direction of the optimal angle used. Hence, using the failure theorem gave the range of sustainability and guided the direction to adopt as Tables 6 and 7 have depicted the result of profiles 1 and 2, respectively, in a positive and negative orientation. A comparison of these results was, therefore, discussed in section 3.1.1.1 to have a better insight on these directions effect over the ply thickness and determine the suitable choice for optimization

Table 6: Ply thickness of profile 1

Part Number	Orientation (Degree)	Profile 1			
		Positive		Negative	
		Stainless steel liner (mm)	Ply (mm)	Stainless steel liner (mm)	Ply (mm)
1	55	3.35	0.1594	3.35	0.1594
2	55	3.908	0.2169	3.908	0.2169
3	55	4.467	0.2834	4.467	0.2834
4	55	5.025	0.3586	5.025	0.3586
5	55	5.583	0.4426	5.583	0.4426
6	55	6.142	0.5357	6.142	0.5357
7	55	6.7	0.6288	6.7	0.6288

Table 7: Ply thickness of profile 2

Part Number	Orientation (Degree)	Profile 2			
		Positive		Negative	
		Stainless steel liner (mm)	Ply (mm)	Stainless steel liner (mm)	Ply (mm)
1	55	6.7	0.6375	6.7	0.6375
2	55	7.817	0.8677	7.817	0.8676
3	55	8.933	1.1	8.933	1.1
4	55	10.05	1.4	10.05	1.4
5	55	11.167	1.8	11.167	1.8
6	55	12.283	2.1	12.283	2.1
7	55	13.4	2.3	13.4	2.33

3.1.1.1 Effects of orientation on ply thickness

Based upon the comparison of negative and positive angles of orientation on the first and second profiles, the ply thickness obtained exhibited equal values of liner variation recorded as shown in Tables 6 and 7. These results obtained for the optimal angle of 55º had no influential change over the ply thicknesses generated. Furthermore, direction of the ply had no effect on the determined thicknesses. This observation was also proven as shown in Figures 7 and 8, depicting the thicknesses of the generated ply with no change between the positive and negative directions of the two profiles. The liner thickness being the independent variable in this specific task, was found to influence the size of the ply.

Conversely, the use of ply direction as an influential factor could only be considered from a different aspect by taking the orientation angle of the ply as the dependent variable in the study. This approach emphasized the variation of angle only in value and not in sign. This result concurred with a similar study by Takalkar et al. (2016), who focused on the first ply failure

theorem with the intention of determining the ply thickness, using a variation of angle through sign and magnitude as well. It is evident that ply elongation was influenced by the angle's magnitude and not by the orientation sign, as illustrated in the findings of this study in Figures 7 and 8.

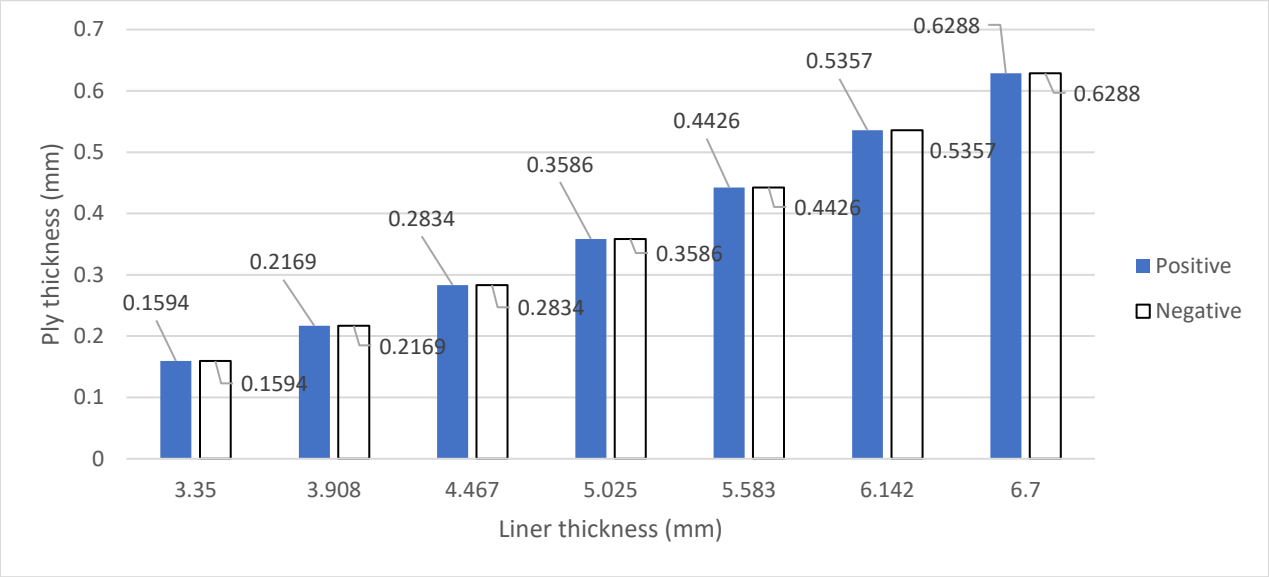

Figure 7: Profile 1 ply thickness for part profiles' liner with respect to the optimal angle direction (55º)

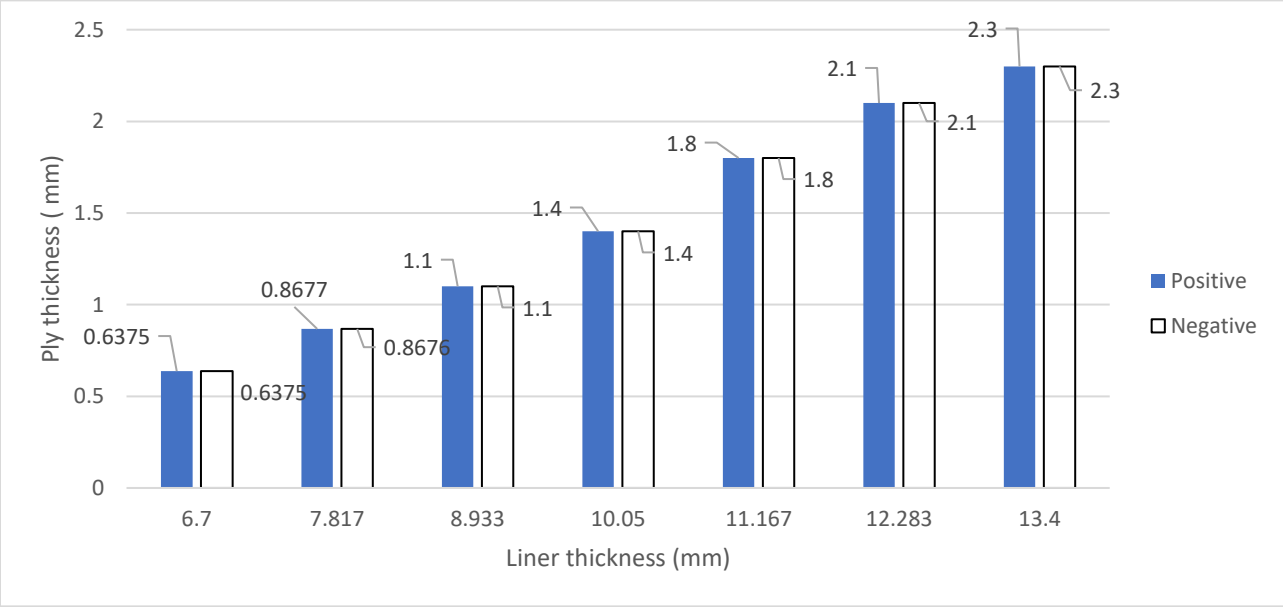

Figure 8: Profile 2 ply thickness for part profiles' liner with respect to the optimal angle direction (55º)

3.2 Identification of sustainable ply range

With the two profiles' generating ply thickness, a range of maximum and minimum level was needed to be determined so as to yield an improved composite pressure vessel through factor combinations (liner and ply thickness). Therefore, the best ply thickness was determined with the aim of strength optimization. The maximum and minimum value of ply thickness given by the Tsai Wu criteria should be the one closest to 1.

3.2.1 Sustainable ply thickness range

The Tsai Wu failure criteria illustrates the first ply failure of the determined ply thickness used to generate the range of plies with the required sustainability to develop an improved design process. From Figure 9, it is apparent that both profiles exhibited corresponding criteria on part profiles 1 to 7. The same observation was made on profile 2, which had dimensions twice the size of the first. This observation can be attributed to the fact that a corresponding increment had been considered between profiles with a double value of 1.117 mm considered in the second. Whereas, a value of 0.558 mm was considered in the first. Hence, with all dimensions doubled and the internal pressure kept constant at a value of 8 MPa, the propagation of stress throughout the structure was correspondingly applied on the composite yielding the same failure criteria between the models of the two profiles as shown in figure 9

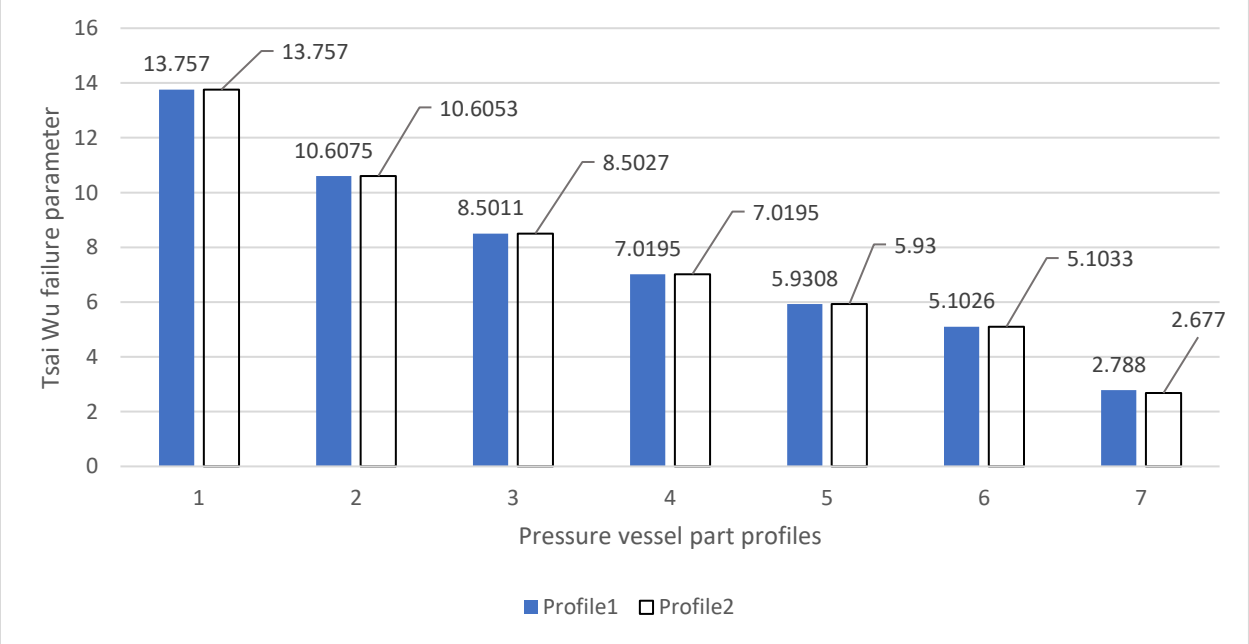

Figure 9: Sustainable range of ply thickness

Based upon the Tsai Wu failure criteria, the range of ply thickness exposing the vessel to less susceptibility to failure was observed in part profiles 5 and 6. These correspond to ply thickness of 0.4426 mm to 0.5357 mm on the first and 1.8 mm to 2.1 mm on the second. These thicknesses of the two profiles have been chosen because of failure criteria closer to stability on Tsai Wu parameter index of 1, that is 1-3 Stability, 3 - 6 Prompt to failure and $>$ 6 Failure (Farhood, 2017). The 7th part profile was not considered as a better option, because its corresponding liner thickness reached the maximum variation gap (between 3.35-6.7 mm and 6.7-13.4 mm).

From these results, it is clear that the required sustainability between ply thickness values of the 5^{th} and 6^{th} trials on both profiles exhibited similarity in failure, despite the double increment on all dimensions between the two profiles.

3.3 Validation of analytical results with numerical ones

By evaluation, constituent of composite pressure vessel being liner and ply thickness were both generated through analytical approach which was the reference method. Therefore, to have more credibility on the generated thickness to be used for the improved design of profiles 1 and 2, validation through numerical approach was done with result presented in the following section.

3.3.1 Validation of ply thickness results

Validation of the generated ply thicknesses was done through failure analysis to determine the level of degradation of all models of profiles 1 and 2 by observing the failure criteria of the designed composite pressure vessels.

As depicted in table 8, it was apparent that the generated failure criteria of various ply thickness, exhibited similarity with slight average divergence of 4 % between the two approaches (analytical and numerical) aiming for the sustainability of 1 respectively on the Tsai Wu and Hashin criteria.

The discrepancy between the two approaches can be explained from the fact that they have different accuracy levels as displayed in the Table 8 representing the error margin between the two methods with the analytical approach taken as reference.

Table 8: Error margin between analytical and numerical method on ply thickness validation

Profile 1							
Analytical Tsai-Wu failure criteria	13.7570	10.6075	8.5011	7.0195	5.9308	5.1026	1.9980
Numerical Hashin failure criteria	13.2000	10.1800	8.1610	6.7120	5.6930	4.8990	1.9000
% error margin	4.05%	4.03%	4.00%	4.38%	4.01%	3.99%	4.91%
Profile 2							
Analytical Tsai-Wu failure criteria	13.757	10.6053	8.5027	7.0195	5.9300	5.1033	1.9870
Numerical Hashin failure criteria	13.2100	10.1800	8.1630	6.7390	5.6930	4.8990	1.9000
% error margin	3.98%	4.01%	3.99%	3.99%	3.99%	4.00%	4.38%

4. Conclusions and recommendations

The conclusions and recommendations based on this study findings are as follows:

4.1 Conclusions

1. For the same ply orientation angle the direction of orientation has no effect on the resulting vessel strength.
2. Based on comparison of research profiles 1 and 2, the various thicknesses of the ply exhibited different effects but with similarity between Tsai Wu failure parameters as shown in figure 9.
3. A margin of error of $\leq 4\%$ was found between results generated by analytical and numerical approaches.
4. The parameter of first ply failure criterion closest to the Tsai Wu value of 1 were recorded on the 5^{th} and 6^{th} model of both profiles. Unlike in the 7^{th} model that had the maximum liner thickness with no improvement in vessel structural design.

4.2 Recommendations for future work

1. With conceptual design improvement being one of the industry's core functions, further study on the adaptation of shell over pressure vessels to reinforce structural integrity is required due to its broad potential application. The analytical and numerical approach have been used in this study to achieve this improved design. Further research can be directed to the experimental approach to have a broader view of this composite pressure vessel's strength improvement.

Authors' contributions

The manuscript was written through the contribution of all authors. All authors discussed the results, reviewed, and approved the final version of the manuscript.

Acknowledgment

This research work is supported by the Vaal University of Technology. The authors wish to thank the Department of Mechanical Engineering at the Vaal University of Technology for facilitating this work.

Conflict of Interest

The author(s) declare no potential conflicts of interest concerning the research, authorship, and publication of this article.

Funding

The author(s) received no financial support for the research, authorship, and publication of this article.

Data Availability Statements

The datasets generated and/or analyzed during the current study are available from the corresponding author on reasonable request.

References

Abrate, S., 1998. Impact on composite structures. *Cambridge University Press,* pp. 86-89.

Adali, S. & Verijenko, V., 1995. Optimization of multilayered composite pressure vessels using exact elasticity solution. *Composite Pressure Vessels* , pp. 203-312.

Alexander, C. S., Key, C. T. & Schumancher, S. C., 2013. Dynamic Response and Modeling of Carbon Fiber-epoxy Composite Suject to Shock Loading. *Journal of Applied Physics,* pp. 22-114.

Alexis, A. K., 1999. Composite Pressure Vessel with High Stiffness. *Elsevier science Ltd Composite structure,* Volume 48, pp. 119-127.

Assam, B.S., Muhammad, M.A. & Mokhtar, M.O.A., 2006.A theoretical and design analysis of the filament-wound. *Composite Pressure Vessels g* , Volume 40, pp. 73-86.

Cerit, M., 2019. Corrosion pit-induced stress concentration in sperical pressre vessel. *Thin-Walled Structures,,* Volume 50, p. 29.

Change, F. K. & Springer, G. S., 1986. The strengths of fiber reinforced composite bends. *Journal of Composite Mater,* pp. 30-45.

Choi, H. I., 2016. Low-velocity impact response analysis of composite pressure vessel considering stiffness change due to cyinder stress. *Composite Structures,* Volume 160, pp. 491-502.

Daniel, I. M. & Ishai, O., 2006. Engineering mechanics of composite materials. *Second Edition Oxford University Press,* pp. 34-67.

Eisenmann, J. R.& Elahi, M., 2007. Comparison of unidirectional and angle-ply lamination. *Continuous-fiber Composites Stiffness,* pp. 175-176.

Farhood NH, K. S., 2017. Burst pressure investigation of filament wound type IV composite pressure vessel. *American Institute of Physics Conference Proceedings,* pp. 56-68.

Frias , C. et al., 2010. Manufacturing and testing composite overwrapped pressure vessels with embedded sensors. *Mater des,* pp. 406-421.

Gentileau, B., Villalonga, F., Nony, H. & Galiano, H., 2015. A probabilistic damage behavior law for composite material dedicated to composite pressure vessel. *International journal of hydrogen energy ,* Volume 13193-13205, p. 40.

Gentilleau, B., Magneville, B. & Villalonga, S., 2011. Modeling, parameters identification and experimental validation of composite materials behavior law used in 700 bar type IV hydrogen high pressure storage vessel. *International Journal Hydrogen Energy,* pp. 456-478.

Graham, J., 1993. Preliminary Analysis Techniques for Ring and Stringer Stiffened Cylinder Shells. *NASA Report TM-108399,* p. 5.

Guiheneuf, V., Bouvier, M. & Jean-marie, A., 2018. Modeling and simulation of a composite highpressure vessel made of sustainable and renewable alternative fibers. *International Journal of Hydrogen Energy,* pp. 970-978.

Hannus, S. & Majak, J., 2003. Orientational design of anisotropic materials using the Hill and Tsai-Wu strength criteria. *Mechanics of composite Materials,* Volume 39, pp. 6-28.

Hashin, Z., 1980. Failure citeria for unidirectional fiber composite. *Jounal of Applied Mechanic,* pp. 329-334.

Hendlmeier, A; Marinovic, L; Al-Assafi, S; Stojcevski, F; Henderson, L C, 2019. Sizing effects on the interfacial shear strength of a carbon fiber reinforced two-componet thermoplastic polymer. *Composites Part A: Applied Science and Manufacturing,* p. 127.

Hereil, P. L., Mespoulet, J. & Plassard, F., 2015. Hypervelocity impact of aluminum projectiles against pressurized alumunum-composite vessel. *Procedia Engineering,* Volume 103, pp. 181-188.

Kam, T., Liu, Y. & Lee, F., 1997. First-ply failure strength of laminated composite pressure vessels. *Composite Structure,* pp. 65-70.

Kamal, K., Sayed,T. & Elbutch,A., 2016. Analytical and finite element modelling of pressure vessel for seawater reverse osmosis desalimation plant. *Desalimation,* Volume 397, pp. 126-139.

Kim, Y. M. et al., 2009. Overview of systems enginerring approaches for a large-scale seawater destination plan with a reverse osmosis network. *Desalination,* pp. 312-332.

Liao, B. B. & Jia, L. Y., 2018. Finite element analysis of dynamic responses of composite pressure vessels under low velocity impact by using a three-dimension laminated media model. *Thin-walled structures,* Volume 129, pp. 488-501.

Mian, H. H., Wang, G. & Dar, U. A., 2013. Optimization of composite material system and lay-up to achieve minimum weight pressure vessel. *Applications of Composite Mater,* pp. 873-889.

Mitrevski, T. et al., 1995. The effect of impactor shape on the impact response of composite laminates.. *Composite Structures,* pp. 169-177.

Nohan, R. & Yaprapragada, R., 2000. Composite Pressure Vessel. *Research in Engineerng and Technology,* pp. 2-18.

Rezakazemi, M. et al., 2011. CFD simulation of water removal from water/ethylene glycol mixtures by pervaporation. *Chenical Engineering Journal,* pp. 183-192.

Sonnen, M., Laval, C. & Seifert, A., 2004. Computerized calculation of composite laminates and structures. *Theory and Reality Material,* pp. 56-67.

Sulaiman, S., Borazjani, S. & Tang, S. H., 2013. Finite element analysis of filament-wound composite pressure vessel under internal pressure. *Material Science and Engineering ,* pp. 757-899.

Sun, X., Du, S. & Wang, G., 1999. Bursting problem of filament wound composite pressure vessels. *International Journal Pressure Vessels Piping,* pp. 55-59.

Taghavian , S. H., Zabihpoor, M. & Jam, J. E., 2010. Developemnt of new method for design of stiffened composite pressure vessel using lattice structures,. *science of engineering composite mater,* pp. 175-182.

Taghavian, S. H., Jam, J. E., Zabihpoor, M. & Yousefzadeh, M., 2014. Development of new method for design of stiffed composite pressure vessel using lattice structures. *Science engineering of composite mater,* pp. 459-468.

Takalkar, A. et al., 2016. Finite element Analysis of Composite Overwrapped Pressure Vessel for Hydrogen Storage. *Conference on Advances in Computing, Communications and Informatics,* pp. 21-24.

Turner, T. W. N. P. S., 2010. Development of high value moulding compounds from recycled carbon fibres. *Plast, Rubber Composite,* pp. 151-167.

Yaacoubi, S. et al., 2016. On the model acoustic emmission testing of composite structure. *Compos Struct,* pp. 446-52.

Yan, L. C. N. J. K., 2014. Flax fibre and its composites. *Composites Part B,* pp. 317-368.

Yarrapragada, R. K., 2012. Composite pressure vessels. *International journal of research in engneering and technology,* pp. 156-167.

Yashar, J., Hamed, S. P., Mohammadreza, H. R. & Mehdi, A. N., 2014. Ultrasonic stress evaluation through thickness of a stainless steel pressure vessel. *International Journal of Pressure Vessle and Piping* , Volume 123, pp. 111-120.

Zhang, W., Mian, H. H., Wang, G. & Dar, U. A., 1996. Buckling optimization of hybrid-fiber multilayer-sandwich cylindrical shells under external lateral pressure. *Composite Science & Technology,* pp. 1349-1353.

Zheng, J. Y., Liu, P. F. & Xu, P., 2009. Finite elemet analysis of busrt pressure of composite hydrogen storeage vessels. *Mater Design,* pp. 2295-2301.

Appendix A: Derivation of stainless steel thickness from Von-Mises theorem.

Form the x and y axis the stress of the axial and hoop nature is as follow:

$$\sigma_x = \frac{PD_i}{4h}$$

$$\sigma_y = \frac{PD_i}{2h}$$

From use of von-Mises formula for pressure vessel made of stainless steel given as follow:

$$\sigma_{max}{}^2 + \sigma_{min}{}^2 - \sigma_{max}\sigma_{min} = \left(\frac{Syt}{S}\right)^2$$

The σ_{max} and σ_{min} are principal stress generated form the axial and hoop stress as below

$$\sigma_{max} = \frac{\sigma_x + \sigma_y}{2} + \tau_{max}$$

$$\sigma_{min} = \frac{\sigma_x + \sigma_y}{2} - \tau_{max}$$

$$\tau_{max} = \sqrt{\left(\frac{\sigma_x - \sigma_y}{2}\right)^2 + \tau^2}\ , \boldsymbol{\tau} = 0$$

$$\left(\frac{\sigma_x + \sigma_y}{2} + \frac{\sigma_x - \sigma_y}{2}\right)^2 + \left(\frac{\sigma_x + \sigma_y}{2} - \frac{\sigma_x - \sigma_y}{2}\right)^2 - \left[\left(\frac{\sigma_x + \sigma_y}{2}\right)^2 - \left(\frac{\sigma_x - \sigma_y}{2}\right)^2\right] = \left(\frac{Syt}{S}\right)^2$$

$$\left(\frac{\sigma_x + \sigma_y}{2}\right)^2 + \frac{(\sigma_x + \sigma_y)(\sigma_x - \sigma_y)}{2} + \left(\frac{\sigma_x - \sigma_y}{2}\right)^2 + \left(\frac{\sigma_x + \sigma_y}{2}\right)^2 - \frac{(\sigma_x + \sigma_y)(\sigma_x + \sigma_y)}{2} + \left(\frac{\sigma_x + \sigma_y}{2}\right)^2 - \left(\frac{\sigma_x + \sigma_y}{2}\right)^2 + \left(\frac{\sigma_x - \sigma_y}{2}\right)^2 = \left(\frac{Syt}{S}\right)^2$$

$$\left(\frac{\sigma_x + \sigma_y}{2}\right)^2 + 3\left(\frac{\sigma_x - \sigma_y}{2}\right)^2 = \left(\frac{Syt}{S}\right)^2$$

From initial equations the axial and hoop stress can be replaced in the expression above and yield the thickness as follow:

$$\frac{\left(\frac{PD}{4h} + \frac{PD}{2h}\right)^2}{4} + 3\frac{\left(\frac{PD}{4h} - \frac{PD}{2h}\right)^2}{4} = \left(\frac{Syt}{S}\right)^2$$

$$\frac{\left(\frac{PD + 2PD}{4h}\right)^2 + 3\left(\frac{PD - 2PD}{4h}\right)^2}{4} = \left(\frac{Syt}{S}\right)^2$$

$$\frac{\left(\frac{3PD}{4h}\right)^2+3\left(\frac{-PD}{4h}\right)^2}{4}=\left(\frac{Syt}{S}\right)^2$$

$$\frac{\frac{9P^2D^2}{4h^2}+\frac{3P^2D^2}{4h^2}}{4}=\left(\frac{Syt}{S}\right)^2$$

$$\frac{12P^2D^2}{64h^2}=\left(\frac{Syt}{S}\right)^2$$

$$\frac{3P^2D^2}{16h^2}=\left(\frac{Syt}{S}\right)^2$$

$$\frac{\left(\sqrt{3}\right)^2P^2D^2}{4^2h^2}=\left(\frac{Syt}{S}\right)^2$$

$$\frac{\sqrt{3}PD}{4h}=\frac{Syt}{S}$$

$t=\frac{\sqrt{3}PDS}{4Syt}$ (Kamal, et al., 2016)

EXPLORING CORRELATION BETWEEN THE SOCIO-ECONOMIC STATUS OF A COMMUNITY AND MICROPLASTIC LOADING IN WASTEWATER EFFLUENT IN NAIROBI, KENYA

C. Bess[1], L. Gumbe[1], M. W. Okoth[2], G. Otieno[3].

[1]School of Chemical and Biological Systems Engineering, The Technical University of Kenya. P.O. Box 52428, 00200 Nairobi-Kenya.

[2]Department of Food Science, Nutrition and Technology, University of Nairobi, P. O. Box 29053, 00625, Nairobi, Kenya

[3]School of Chemistry, The Technical University of Kenya. P.O. Box 52428, 00200 Nairobi-Kenya.

Corresponding author: claudia.bess@tukenya.ac.ke

Abstract

The exponential growth in plastic waste may be attributed to an increase in consumerism and the increasing number of products made from plastic. According to the OECD 2022 report, over the last 20 years, a doubling in the number of plastic products produced annually has occurred. Modelling projections suggest that by 2060, a tripling in plastic production will occur, with sub-Saharan countries such as Kenya accounting for a large percentage of the increase (OECD, 2020). Concomitant with the increased production of plastics is accumulation of plastic waste, which persists in the environment. In particular, the environmental impact of microscopic sized plastics, microplastics, is a growing global concern. Given the chemical and physical nature of plastics, the life cycle management of microplastics has been recognized as an environmental challenge, contributing to among others, greenhouse gas emissions.as well as a source and a sink for chemical contaminants and therefore a pathway for environmental pollution and bioaccumulation of pollutants (Carpenter and Smith, 1972; Andrady, 2011). Identifying potential upstream sources of microplastic pollution is essential in determining mitigation strategies.

Hypothesizing that the microplastic loading from wastewater effluent may be correlated to the socio-economic status of the community from which the waste is discharged, wastewater samples discharged from three different socio-economic communities in Nairobi, Kenya, were collected and analyzed. Results showed that microplastic count in the higher socio-economic community was one-third that observed in the lower socio-economic community, middle and lower-middle income communities having a higher loading at 0.011 items/litre.m^2 and 0.024 items/litre.m^2 respectively, and high-income areas discharging 0.005 items/litre.m^2. Also, the analysis determined that the main chemical composition of microplastic were from polyvinyl chloride, polyethylene, polyethylene terephthalate and polyacrylamide material used in, among others, the manufacturing of household products such as plastic containers and toothbrushes as well as clothing.

Keywords: Plastic pollution, Microplastics, Environmental management, Nairobi.

1. Introduction and Study area

The production of multitudinous types of plastic materials for use in various industries is attributed to the properties of plastics as well as the economics thereof. Plastics are polymeric materials manufactured from synthetic, semi-synthetic or organic components, which are deemed essential for modern human life; and are used in the manufacturing of copious types of household, commercial and industrial goods. An estimated 95% of primary plastics produced is attributed to eight (8) synthetic polymers[1], with end-of-life management generally including recycling (approximately 10%), incineration (14%) and the remaining plastic waste being landfilled, dumped, or released into the natural environment (Geyer, 2020). Globally, approximately 22% of mismanaged plastic waste is attributed to Africa, and Kenya is purported to account for 0.5% (Meijer et al., 2021). Studies have confirmed the presence of particulate plastics measuring 5 mm or less in diameter (microplastics) (Carpenter and Smith, 1972; Wright et al., 2013; Law & Thompson, 2014; Cincinelli et al. 2017) in marine and freshwater environments (Cole et al., 2011; Wright et al., 2013; Free et al., 2014; Sanchez et al., 2014; Nel and Froneman, 2015; Biginagwa et al., 2016).

Whilst there is a direct correlation between the per capita consumption of plastics and the gross national product, on a volume basis, future plastics consumption is likely to increase more rapidly in developing countries where waste management practices present a challenge (OECD, 2022). Factors such as the low-technology processing operations, the large disparity in labour rates in developed countries versus developing countries as well as less stringent environmental regulations often resulting in lower operational costs, is expected to contribute to the proliferation of chemical industries in the developing regions, and therefore an increasing per capita consumption of plastic material.

In Kenya, waste management practices concomitant with often ineffectual waste management policies have resulted in plastic accumulation in the natural environment (OECD, 2022). An estimated 50% of the approximately 24 million single-use plastics utilised monthly in Kenya, ends up in the solid waste mainstream (Odhiambo et al., 2014). Additionally, Odhiambo et al. (2014) attribute the accumulation of plastic wastes in Nairobi City to ineffective solid waste management practices by both stakeholders and the general population as well as weak environmental management policies. Combined with a low solid waste collection ratio which results in indiscriminate dumping of waste, is a marked inequality in the geographical waste collection service distribution in Nairobi; with low-income areas which are located predominantly in the Nairobi River Basin (NRB) and where over 55% of the Nairobi residents live, having little or no waste collection service (Njoroge et al., 2014). Collectively, this gives rise to the high percentage of mismanaged plastic in the NRB.

Microplastic pollution

Anthropogenic factors such as poor wastewater, solid waste, and industrial waste management, along with poor urban planning and environmental degradation both within Nairobi City and its immediate environs, present as contributing factors for point and non-point sources of microplastic pollution of the Nairobi ecosystem. On average, plastic waste constitutes approximately 14% of

[1] The eight most used synthetic polymers include polyvinyl chloride polypropylene, high- and low-density polyethylene, polystyrene, polytetrafluoroethylene (Teflon), thermoplastic polyurethanes and nylon (nylon 6, nylon 6,6) (Geyer, 2020).

managed solid waste in Nairobi (Njoroge et al., 2014). With less than 50% of the households in Nairobi having access to solid waste management services (Njoroge et al., 2014), coupled with high population density in the NRB, according to United Nation Environment Programme (UNEP), some 83% of the plastic material used in Kenya is mismanaged (Paruta et al., 2020). The fraction of mismanaged plastic waste is significant with potential for dire negative impacts from microscopic sized particles arising from disintegration of macroscopic-sized plastic wastes or through direct discharge of microscopic-sized material, on aquatic and human health.

Additionally, microplastic pollution may arise from the discharge of microplastics into surface waters such as the Nairobi River. This can occur through effluent discharged from wastewater treatment plants and surface runoffs being discharged into river bodies. Studies have shown that despite a high retention of microplastics in some wastewater treatment facilities, between 90% and 95% removal after secondary treatment (Talvitie et al., 2015), wastewater treatment facilities may present as a point source of microplastics being released into the environment (Murphy et al., 2016). Whilst wastewater treatment plants can trap small plastic debris within oxidation ponds or sewage sludge, a large proportion of microplastics, will pass through such filtration systems (Browne et al., 2007; Fendall and Sewell, 2009; Eriksen et al., 2013; Gregory, 1996).

Factors influencing the extent of microplastic pollution include population size, proximal to water bodies, nearness to urban centres, water residence time, size of the water body, the waste management system in place, and amount of sewage discharged into the environment (Moore et al., 2011; Zbyszewski and Corcoran, 2011; Eriksen et al., 2013; Free et al., 2014). Inferred from Moore et al. (2011), income may be the most critical socio-economic factor which influences microplastic pollution with other contributing factors.

The Nairobi River is the main river in the Nairobi River Basin (NRB) which is an ecosystem crucial to the economic well-being and poverty alleviation for many of Nairobi residents, as well as the environmental sustainability of the region. A significant number of persons residing within the NRB rely directly and/or indirectly on commercial and subsistence agriculture as a basis of their livelihood, resulting in the quantity as well as quality of the water resource being of great importance. NRB is composed of over 1500 plant species, many of which are identified as medicinal plants as well as being a source of food and wood; faunal species which adds not only an aesthetic value but also economic value; fish species which are often used as food; in addition to agriculturally productive soils (Nyika, 2017). Further, the water resources of the NRB along with that from the Athi River are crucial for irrigation, industrial and municipal uses within the urban and municipal towns and the immediate environs (Nyika, 2017).

1.1 Study Area

Nairobi, the capital of Kenya, is the country's most populous city (KNBS, 2019). This *"Green City in the Sun"* lies over an area of 696 km^2 and continues to grow as rural residents migrate to the city, mainly to seek employment opportunities (KNBS, 2019). Given the area of Kenya's capital city and the estimated number of residents, the population density is approximately 6000 residents per square kilometre (KNBS, 2019). Approximately 60% of Nairobi's population live in informal settlements (Alder, 1995; Mitullah, 2003; Zulu et al., 2011). Additionally, some 18 percent of the population of Kenya lives in urban centres, and over 33 percent of the urban population is accounted for by the Nairobi Metropolitan Area (KNBS, 2019).

The sewerage system in Nairobi City consists primarily of two major treatment facilities - the Dandora Estate Sewage Treatment Work (DSTW), and the Kariobangi Sewerage Treatment Works (KSTW), supported with almost 165 km of trunk sewers (NCWSC, 2021). The Dandora sewage treatment system employs anaerobic ponds in the treatment of the waste, and currently treats approximately 80% of the wastewater generated in Nairobi (NCWSC, 2021). The wastewater reticulation system in Nairobi serves an area of approximately 210 km^2, which accounts for less than 50% of the total area covered by the water supply service area (NCWSC, 2021). Many of the existing sewers are combined sewers and are predominantly in the central business district and the immediate environs of Nairobi.

Wastewater samples were collected from selected sites in the Nairobi area. The sampling locations were selected based on the socio-economic status of communities as well as the reticulated sewerage system within Nairobi City. Three sampling communities identified were (Fig 1):

(i) Ngumo Estate: located in the northern region of Nairobi City. Ngumo Estate is predominantly a residential community. According to the Kenya National Bureau of Statistics: 2009 Kenya Population and Housing Census and Kenya Integrated Household Budget Survey, Ngumo Estate may be categorized as a medium to large sub-location with a population between 20,000 and 50,000, with approximately 30% of the population living below the poverty line. The 2019 Kenya population census indicates that the sub county in which Ngumo Estate is located has a population density of 16,150 number of persons per km^2.

Wastewater samples were collected along the NCWSC trunk sewer in Ngumo Estate. (Fig. 7). Samples were taken within the Golf Course Phase 1 and East Court complexes, as well as in the vicinity of the Mbagathi Road Primary School and the Miami Global Hotel.

(ii) Woodley Estate: A lower-medium income residential estate, Woodley Estate is located west of central Nairobi in Dagoretti sub-county. The sampling points were W1 and W2 (Fig. 7) within the Kangethe complex and its immediate environs; and

(iii) Upper Hill: located in central Nairobi. Upper Hill is described as a medium sub-location, with less than 10% of the population living below the poverty line (Kenya Bureau of Statistics (2009)). Predominantly a commercial hub, with medium to high-income residential complexes, Upper Hill is described as a centrally located middle-upper-level income community.

Wastewater samples were collected in two areas (UP1 and UP2) in the Upper Hill area along the NCWSC sewer main (Fig. 7). Sample site UP1 is located in a commercial district, where in addition to a number of hotels and business places, a residential housing complex discharges directly into the main sewer located along 4th Avenue, upstream of the collection point. Sample site UP2 is located along the outskirts of Upper Hill, where a number of housing complexes discharge into a main sewer line which runs along Upper Hill Road. Samples were collected upstream and downstream of the housing complexes (Fig. 7).

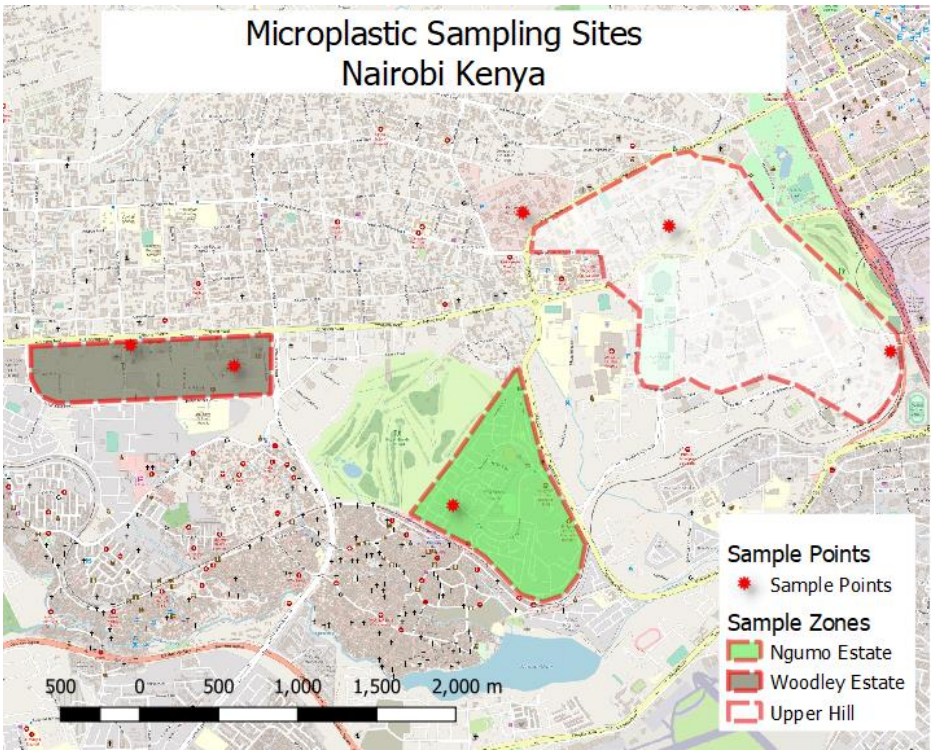

Fig. 7: Study Area

Effective mitigating strategies to combat microplastic pollution in the Nairobi River Basin can be best instituted if upstream point sources can be identified. It is hypothesized that wastewater is a significant contributor to microplastic pollution, and that the extent of pollution is directly linked to the socioeconomic status of the communities. In testing the hypothesis, wastewater samples from different socio-economic communities were collected and analysed.

2. MATERIALS AND METHODS

2.1 Conceptual Framework

It is postulated that the quantity and composition of microplastic discharged from a community is a function of (i) the community's socio-economic status as well as (ii) the time of day. To test the hypothesis, the quantity and quality of microplastics being discharged into the environment from wastewater samples were determined. Samples were collected at three estates, within Nairobi City, each of a different socio-economic status.

The study sought to establish the veracity of the hypothesis that microplastic discharged in wastewater effluent from households, $O_{HP,}$ is a function of the economic status, and the time of day. The relationship is of importance as wastewater discharged from estate (O_{HP}) is directly related to the microplastics loading to the wastewater treatment facility (I_{WP}) and by extension the output from the waste treatment facility (Fig 8).

Treated effluent from the Dandora wastewater treatment plants in Nairobi, is discharged directly into the Nairobi River and will therefore play a critical role in impacting the microplastic loading of the river.

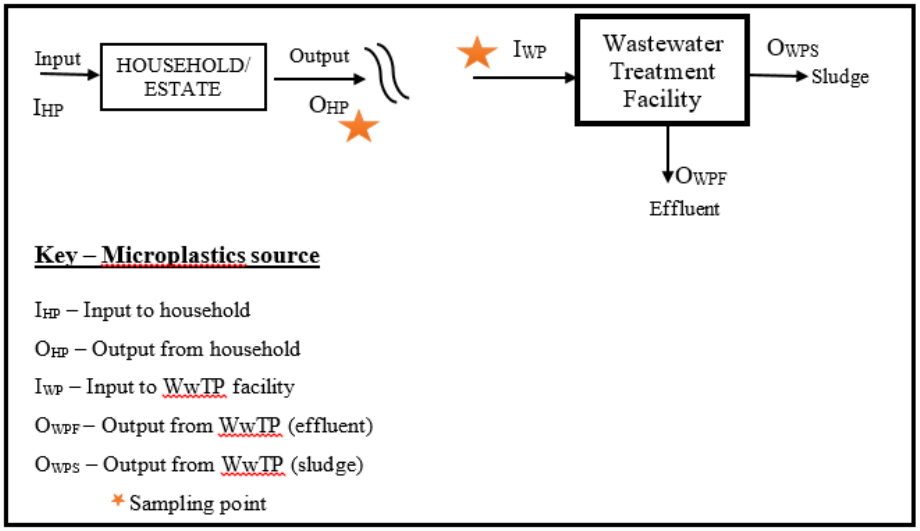

Fig 8**:** Schematic showing sampling regime.

$$O_{HP} = f(I_{HP}, economic\ status\ of\ community, time\ of\ day, population\ density)$$
$$I_{HP} = f(Income)$$
$$O_{HP} = f(I_{HP})$$
$$I_{WP} = \sum_{i=1}^{n} O_{HPi}$$
$$O_{WPS} = f(I_{HP}, Treament\ mode, flowrate)$$

2.2 Sampling methodology

Fig 9 is a framework outlining the concept employed in determining the correlation between microplastic loading in wastewater discharged from different socio-economic communities. Standardised procedures for collecting, fractionating, characterizing, and quantifying polymer particles; currently does not exist, and remains a significant obstacle in research on microplastic pollution. The conventional method of saturated salt separation generally results in an efficiency which varies between 80-100%, with a mean recovery rate of 40% based on the size microplastic (Fries *et al.*, 2013; Imhof *et al.*, 2013). Given budgetary and technological constraints, the salt saturation methodology was used in the separation of the microplastics.

The methodology used in the collection and extraction of microplastics was guided by the laboratory method defined in the NOAA Marine Debris Manual (Masura et al., 2015, Löder and Gerdts, 2015; Tagg et al., 2015). Considering the temporal and spatial distribution of microplastic pollutants in wastewater samples, for each sampling area, two sets of wastewater samples were collected for each sampling event, one sample at the inlet and the other sample outlet of a sewer main from the Nairobi City Water and Sewerage Company (NCWSC). Samples were collected at least twice from each sampling area. Additionally, samples were collected on separate dates and times, therefore, there was no replication of samples, thereby resulting in multiple sampling events. There are three identifiable steps for the extraction and processing of samples containing microplastics (Masura *et al.*, 2015 Simon et al., 2018):

1) Sieving and filtration - to remove macroscopic sized particles as well as large size debris which might be contained in the sample matrix,

2) Wet peroxide oxidation (WPO) - involves the removal of any organic material from the sample matrix (Masura, J., et al., 2015; Löder and Gerdts, 2015; Thompson et al., 2004; Browne et al., 2010; Ng and Obbard, 2006); followed by density separation (Thompson et al., 2004; Browne et al., 2010; Ng and Obbard, 2006) and
3) Sorting/identification of microplastics - the application of analytical techniques to quantify the amount of microplastics contained within the sample matrix, as well as to identify the composition of the microplastic.

Quantification and characterisation of the microplastics were undertaken using optical microscopy and FT-IR analysis respectively.

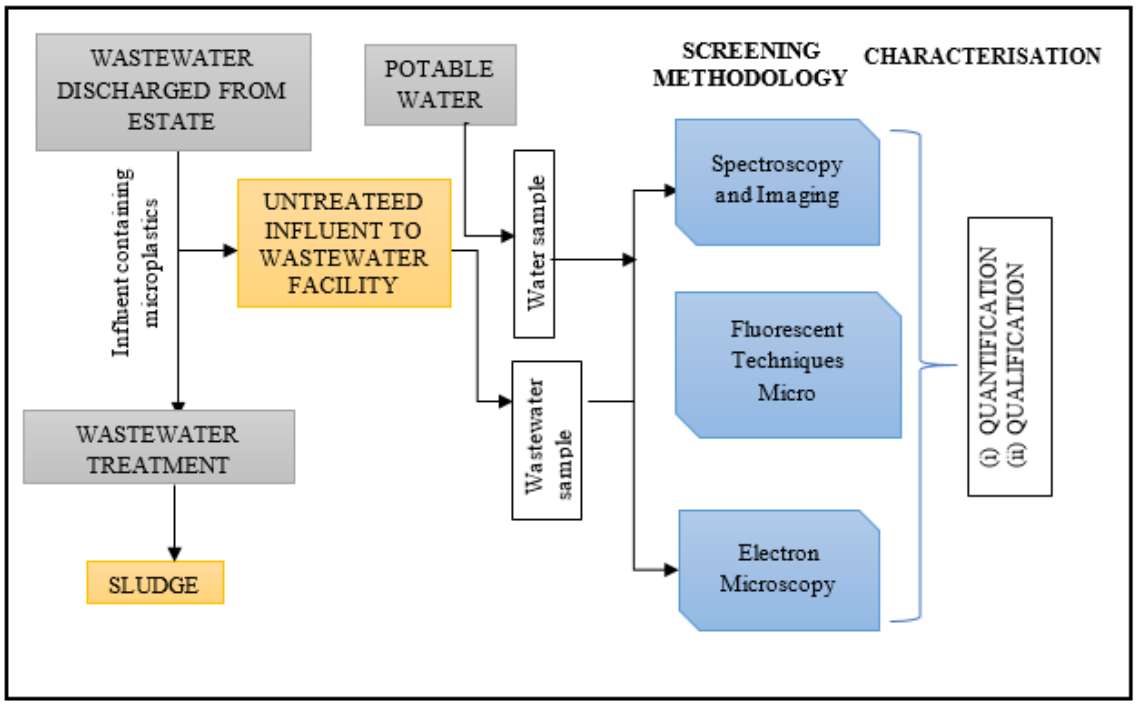

Fig 9: Multi-tier framework for the sampling and analysis of microplastics from water and wastewater samples

2.2.1 Sample Collection

Raw Wastewater

Given the experimental set-up and the available access to the Nairobi wastewater reticulation system, raw wastewater samples were collected in clear 5L glass bottles. Glass bottles were used to reduce contamination of the sample. Where possible, the wastewater samples were collected at manholes at which continuous flow existed, to reduce sampling errors which might arise from the concentrating of plastics. Samples were collected during the dry weather period – which was defined as a period where 3 mm or less precipitation for 48 hours before and during sampling had occurred. Additionally, given the temporal distribution of wastewater flow which may impact the concentration of microplastics contained within the sample, samples were collected in the mornings and afternoons, which is in keeping with attempts to take representative samples; and where possible, samples were collected at locations of highly turbulent flow in order to ensure

good mixing. A total of 20L of wastewater sample was collected for each sample location for each sample event.

Potable Water

To establish if the potable water being supplied to households is a contributing factor to microplastic count in the wastewater samples collected, potable water samples were collected at the major intake main water line supplying the respective community. In keeping with the quality guide lines, water samples were collected in glass bottles to minimize any contamination.

2.2.2 Analysis of extracted microparticles

The separated microparticle samples were quantitatively and qualitatively analysed. Analysis of the microparticles involved the use of optical microscopy and Fourier-transform infrared spectroscopy (FT-IR). The Optika Vision Lite microscope was used in the quantitative analysis of the samples, and a nonprobability sample method used in determining the sample size obtained from the filter paper being examined under the optical microscope to obtain the microplastic count. The equipment used for qualitative analysis was a FT-IR spectrometer - model WQF-520.

3. RESULTS AND DISCUSSION

3.1 Results

Microscopic and spectroscopic techniques were employed in the analysis of the microparticles separated from the water and samples. Images obtained using the Optical Microscope confirmed the presence of microparticle (Plate 1 – Plate 4), with an average microparticle count of 1130 microparticles/litre of wastewater effluent. From the study the average microparticle count for the Upper Hill region was 1074 microparticles/litre, 95% CI [239,1910], Ngumo Estate 910 microparticles/litre, 95% CI [-611, 2430] and Woodley Estate 1395 microparticles/litre, 95% CI [-693, 3483] (Fig. 10).

The microparticle count in the lower-middle income community was one-third greater than that in the high-income community and middle-income community. However, when the drainage area is taken into consideration (Fig. 11), with a microparticle count of $5x10^{-4}$ items/litre.m^2, the upper income area had significantly less microparticles discharged its raw wastewater in comparison with the 24 x 10^{-4} items/litre.m^2 observed in the lower-middle income community.

Analysis of potable water from the respective communities also showed the presence of microparticles. On average, there were 172 items per litre of potable water.

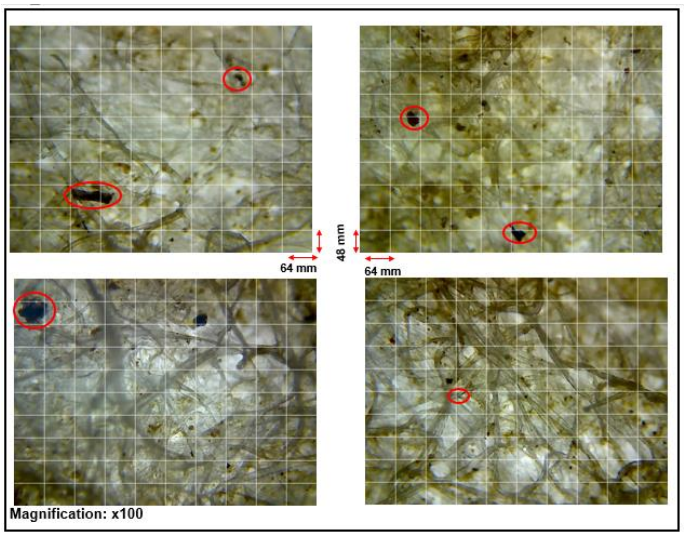

Plate 1: Microscopic image of wastewater sample showing microscopic particles. Upper Hill – December 2021.

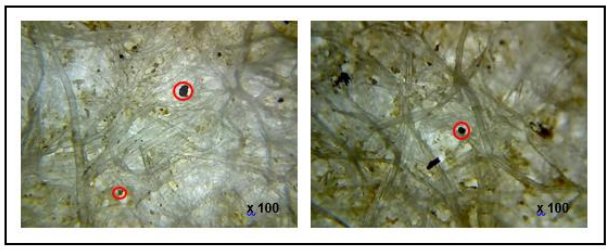

Plate 2: Microscopic image of particles identified in wastewater sample collected at Woodley Estate - November 2021.

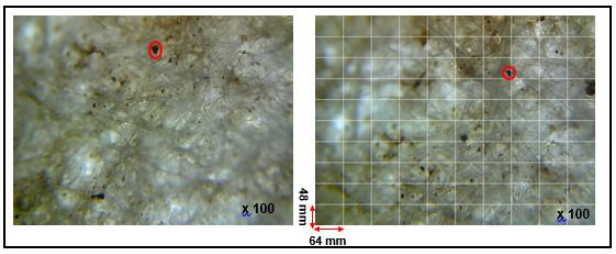

Plate 3: Microscopic image of particles identified in wastewater samples collected in Ngumo Estate –December 2021.

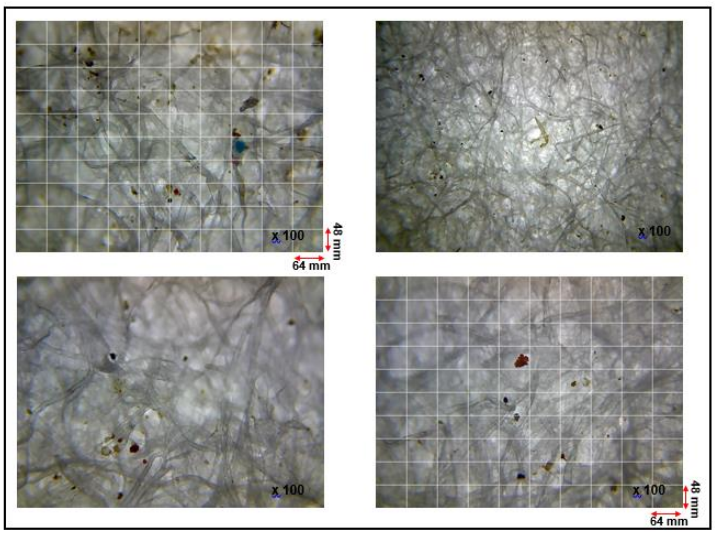

Plate 4: Microscopic images of microparticles in identified in water samples.

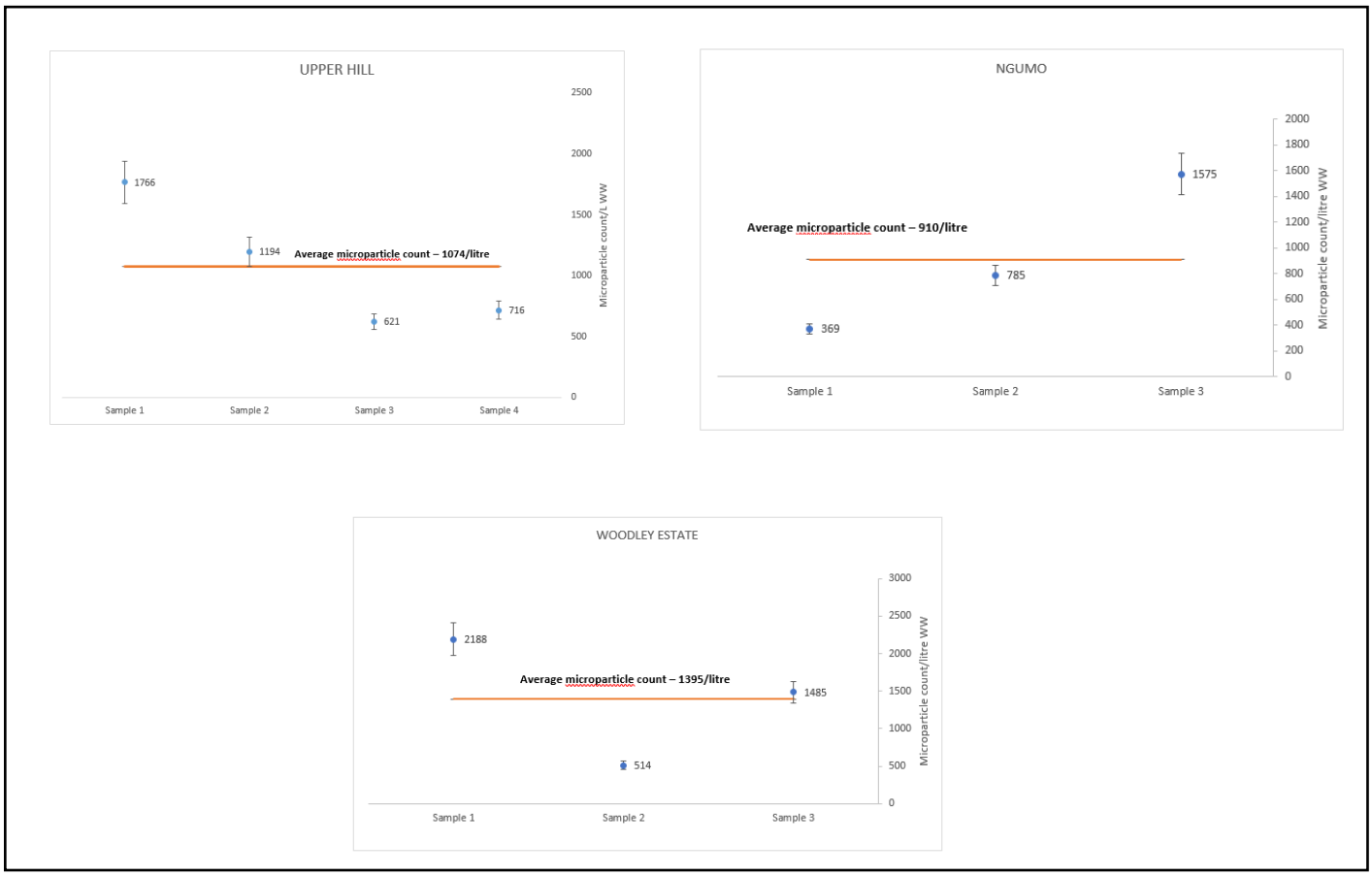

Fig. 10: Microparticle count for different socio-economic communities in Nairobi, Kenya.

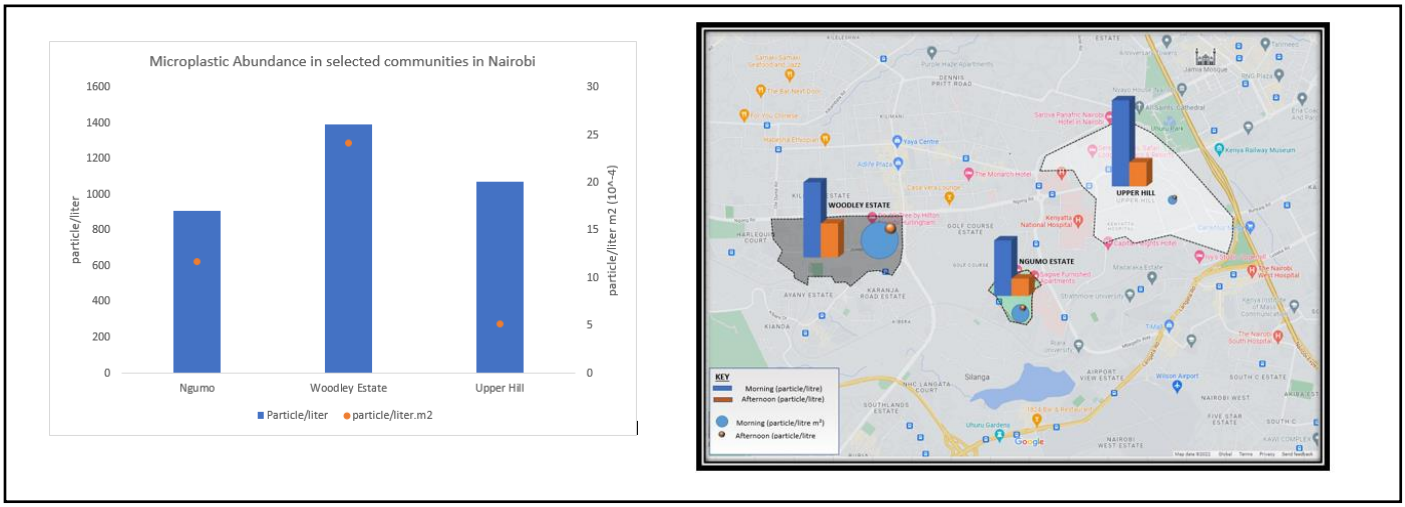

Fig. 11: Collation of microparticle count and socio-economic status and time of discharge in wastewater samples of communities in Nairobi, Kenya.

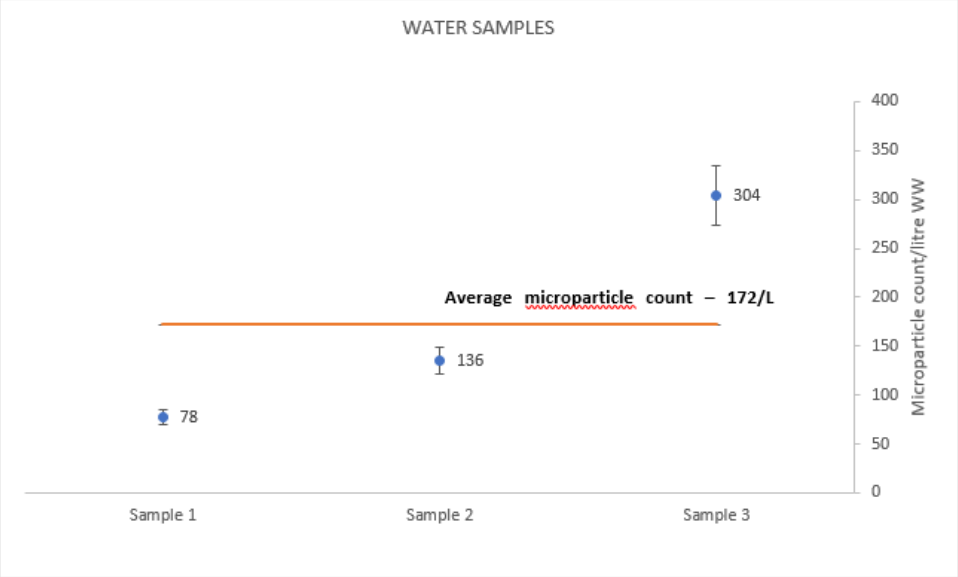

Fig. 12: Average microparticle count in water samples.

The microplastic count in the wastewater samples analysed was greater for the samples collected in the morning than that collected in the afternoon (Table 6).

Table 6**:** Microplastic count for different socio-economic communities based on time of day.

Sample Location/ Time of day	**UPPER HILL**		**NGUMO**		**WOODLEY ESTATE**	
UNIT	Particle /litre	Particle /litre m^2	Particle/litre	Particle /litre m^2	Particle /litre	Particle /litre m^2
Morning	1480	0.72	1180	1.52	1836	3.18
Afternoon	669	0.32	369	0.48	514	0.89

Identification of microparticles

The FT-IR spectra for the extracts obtained from the wastewater and water samples collected from the respective communities were recorded by averaging 20 scans with 4 cm^{-1} resolution. FT-IR spectroscopy enables the identification of the functional groups of the different types of plastics (Mansur et al. (2008), Larkin, 2011; Workman, 2001) (Fig.13-
Fig. 16).

A comparative analysis of the spectra generated with those found in literature was undertaken (D'Amelia et al. 2016, Baumhardt-Neto & Paoli, 1993; Rajakumar et al., 2009). The group frequencies of the infrared spectra observed from the samples were predominantly in the mid-infrared spectrum of 4000 – 400 cm^{-1}. Generally, the samples showed broad shoulder appearing at

around 3450 cm^{-1} which may be attributed to non-hydrogen-bonded N–H bonds. C-H stretching at 3100 – 3000 cm^{-1}, typical of benzene ring absorptions are observed, overtone and combination bands at 2000–1650 cm^{-1}, ring stretching at 1600–1550 cm^{-1}, ring stretching at 1500–1450 cm^{-1}, C–H in-plane bending at 1300–1000 cm^{-1}, and C–H out-of-plane bending at 900–600 cm^{-1}.

Upper Hill

From the IR spectrum recorded for the samples collected in Upper Hill (Fig.13), absorbance bands are located at 487 cm^{-1}, 3362 cm^{-1} and 3891 cm^{-1}, as well as at 1610 cm^{-1} which may be attributed to C-H bending, and N-H stretching. Additionally, a peak is observed at 1113 cm^{-1} which is indicative of the C-O stretching of the COH/C-O-C functional group. Peaks are also observed at 466 cm^{-1}, 3362 cm^{-1}, 3450 cm^{-1} and 3382 cm^{-1}.

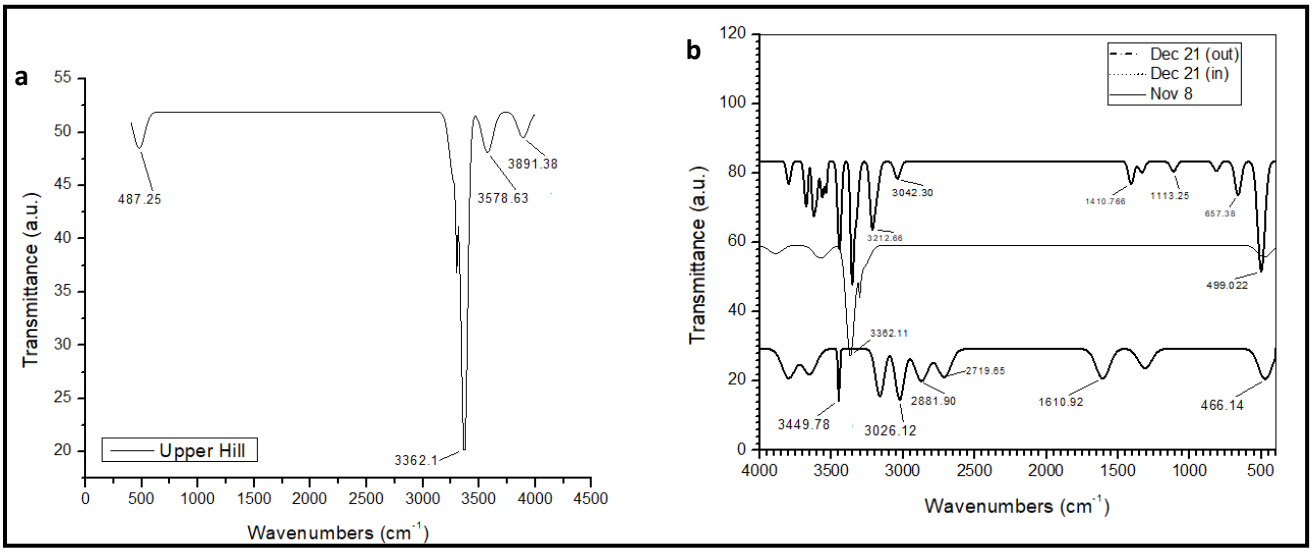

Fig.13**:** IR spectra: FT-IR (KBr) analysis of particulate matter obtained from wastewater samples - Upper Hill.

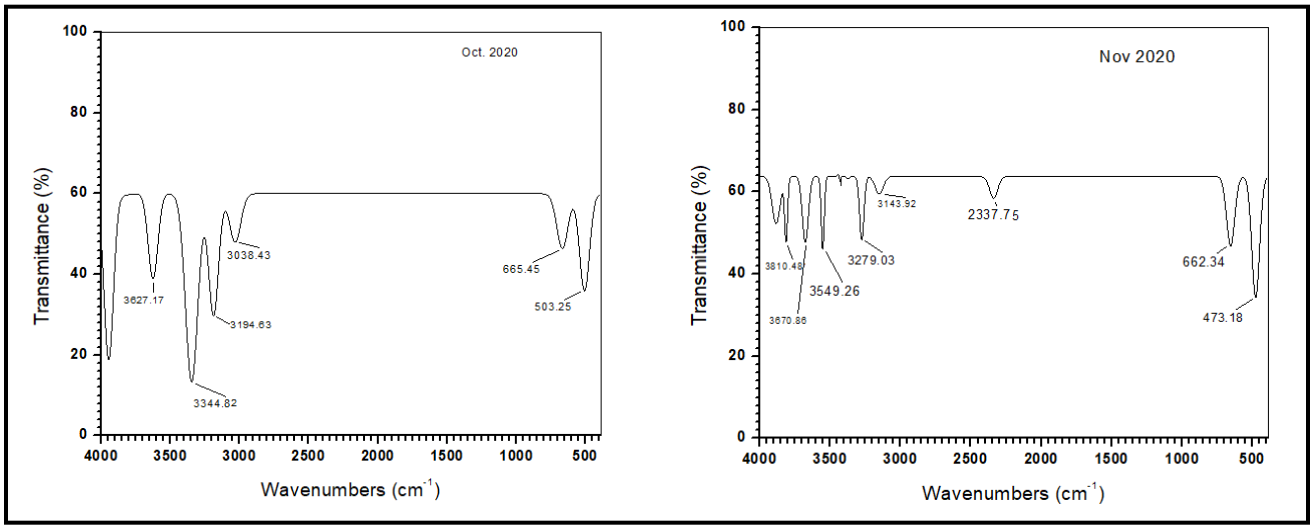

Fig.14**:** IR spectra: FT-IR (KBr) analysis of particulate matter obtained from wastewater samples – Ngumo Estate.

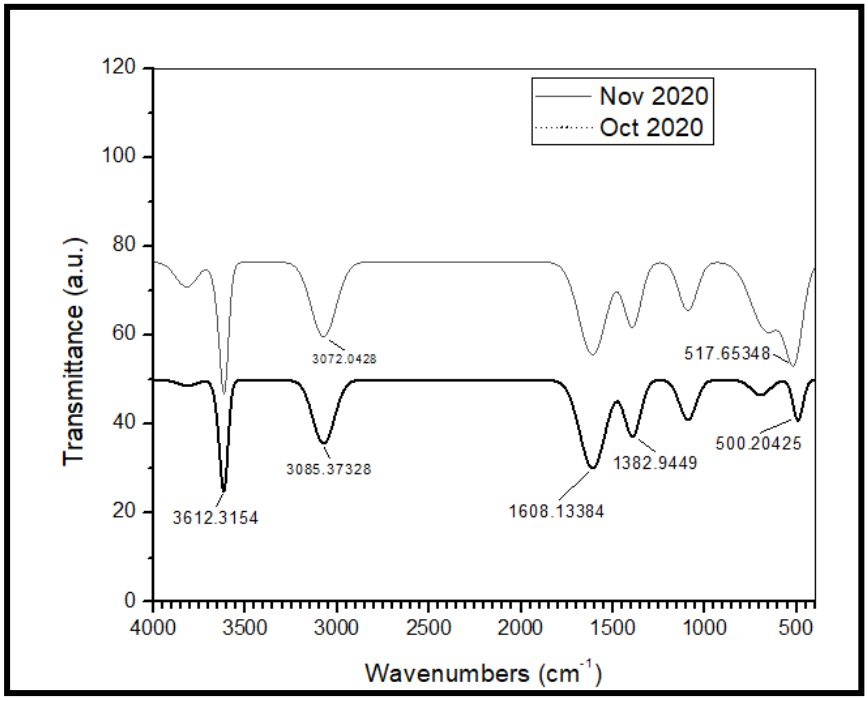

Fig.15**:** IR spectra of the particles obtained from the wastewater samples based on FT-IR (KBr) analysis – Woodley Estate

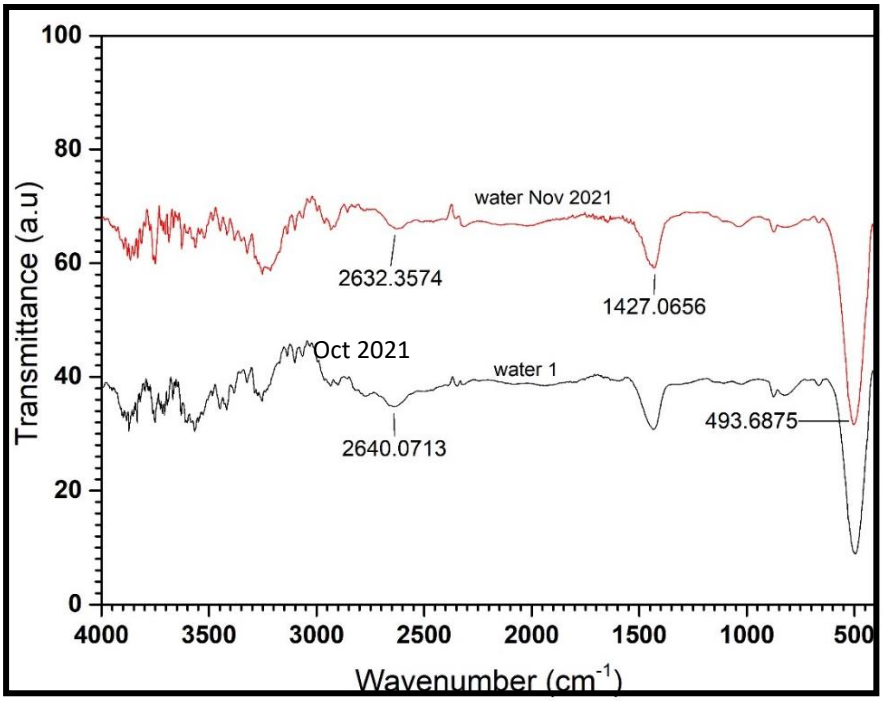

Fig. 16**:** FTIR Spectra - Potable water sample

Peaks at 3362 cm^{-1} would suggest that the microparticles extracted may contain a hydroxyl stretch as is found in polymers such as polyvinyl alcohol and polyacrylamide. Polyvinyl alcohol is used in the food packaging industry, laundry detergent, disinfectants, cleaning

chemicals, papermaking, as a thickener and emulsion stabilizer in polyvinyl acetate adhesive formulations as well as in a variety of coatings, and 3D printing. Polyacrylamide is a synthetic polymer, commonly used as a flocculant in water and wastewater treatment, and friction reducer in both enhanced oil recovery and high-volume hydraulic fracturing. Additionally, polyacrylamides are used in the agriculture sector to enable erosion control and decrease soil sealing through the binding of soil particles; in the food processing industry as well as in consumer products such as cosmetics as a stabilizer.

Peaks observed at 3675 cm^{-1}, 3450 cm^{-1} and 3891 cm^{-1} are similar to those observed in poly (vinyl butyral) polymers which are resins used for binding. Similarly, peaks observed in microparticles obtained from samples taken at Ngumo Estate (Figure 4 8), where spectral bands at 3810 cm^{-1}, 3549cm^{-1} and 3670 cm^{-1}.

Ngumo Estate

Fig. 8 shows spectral bands at 3143 cm^{-1}, 3038 cm^{-1} and 2338 cm^{-1}, which may be attributed to aliphatic symmetric and asymmetric C-H stretching. Also, there were absorbance bands at 3279 cm^{-1} and 3344cm^{-1}, which may be due to N-H stretching.

Woodley Estate

The IR spectra generated from the particles extracted from the wastewater samples collected at Woodley Estate (Fig.15) show spectral bands at around 3612 cm^{-1} which seems to indicate the NH2 stretch; 1650 cm^{-1} as well as about 1625 cm^{-1} which is characteristic of C=O stretching and NH2 bending respectively. The absorbance band identified at 1382 cm^{-1} is characteristic of the symmetric methyl bending as well as the spectral band which was observed at 518 cm^{-1}.

3.2 Discussion

The versatility of plastics has resulted in its ubiquitous use in everyday life, and as a consequence, an exponential growth in plastic wastes, resulting in the challenge of identifying feasible end-of-life management options. The results of this research indicates the presence of microplastic particles as a possible constituent of the microparticles found in wastewater effluent discharged from selected communities in Nairobi, Kenya. Investigation of water and wastewater samples in selected communities in Nairobi, showed on average, 1130 microparticles /litre of wastewater effluent and approximately 170 microparticles/litre of water samples. This research showed that plastics used in the manufacturing of clothing and containers were present in the wastewater samples discharged from households, synthetic polymer used in water treatment, as well as polymers used for packaging material were also found in the samples.

The microparticle count in wastewater samples collected from the three different socio-economic communities, seems to concur that there might be a correlation between the amount of microparticles discharged in wastewater and the economic status of a community (Fig. 11). The microparticle count per square meter in Woodley Estate and Ngumo Estate is 0.0024 and 0.0011 item/litre respectively. Both communities have a similar population density, however, the microparticle count in the middle income was half that in the amount observed in the lower-middle income community. The lower income area, with 24 $x10^{-4}$ items/litre.m^2, exhibited a microplastic count five times greater than the high-income area.

FT-IR imaging suggests that some of the microparticles obtained from the wastewater samples show similar spectral characteristics of polyvinyl chloride, polyethylene (PE) and polyethylene terephthalate (PET). PE and PET are both used extensively in the manufacturing of clothing and containers for liquids, from nondrinking bottles, lids/caps, and dairy packaging. According to Paruta et al. (2020), these polymers are amongst some of the most commonly leaked plastics into the environment.

The microparticle loading also seems to be related to the time of day (Table 1 and Fig. 11). Samples collected in the mid-afternoon seem to have a microparticle count of approximately one-third the count observed for the midmorning samplings. This could be related to the activities which are undertaken at the given time of day in the respective communities. It is postulated that activities such as laundering, showers and other activities which might contribute to the microparticle count in the wastewater, would have occurred earlier in the day.

4. CONCLUSION

Factors such as the low-technology processing operations, the large disparity in labour rates in developed countries versus developing countries as well as less stringent environmental regulations often resulting in lower operational costs, is expected to contribute to the proliferation of chemical industries in the developing regions, and therefore an increasing per capita consumption of plastic material(OECD, 2022a).

From the study it can be surmised that households present a pathway for microplastics loading to wastewater treatment facilities and by extension to the environment. Microplastics are discharged in the wastewater effluent from residential and commercial facilities into the Nairobi sewerage system, with middle and lower-middle income communities having a higher loading at 0.011 items/litre.m^2 and 0.024 items/litre.m^2 respectively, and high-income areas discharging 0.005 items/litre.m^2; and the use of FT-IR analysis confirmed that amongst the microparticles observed using microscopic images, polymeric particles, polymeric particles such as PVC, PE, PET and polyacrylamide were present.

Data Availability Statement: All relevant data are within the paper.

Funding Statement: The authors received no specific funding for this work.

Competing interests: Claudia Bess, Lawrence Gumbe and Geoffrey Otieno are employed at the Technical University of Kenya and Michael Okoth is employed at the University of Nairobi. The authors declare that no competing interests exist.

Author Contribution statement: Claudia Bess, Lawrence Gumbe, Michael Okoth and Geoffrey Otieno contributed to the design and implementation of the review work, the analysis of the results and the writing of the manuscript.

REFERENCES

Alder, G. (1995). Tackling poverty in Nairobi's informal settlements: developing an institutional strategy. *Environment and Urbanization, 7*(2), 85-107.

Andrady, A. (2003). *Plastics and the Environment.* Hoboken, New Jersey: John Wiley & Sons, Inc.

Andrady, A. L. (2015). *Plastics and Environmental Sustainability.* Hoboken, New Jersey: John Wiley & Sons, Inc,.

Baumhardt-Neto, R., & De Paoli, M.-A. (1993). Mechanical degradation of polypropylene: Effect of UV irradiation. *Polymer Degradation and Stability, 40*(1), 59-64. Retrieved from https://doi.org/10.1016/0141-3910(93)90191-K

Biginagwa, F. J., Mayoma, B. S., Shashoua, Y., Syberg, K., & Khan, F. R. (2016). First evidence of microplastics in the African Great Lakes: Recovery from Lake Victoria Nile perch and Nile tilapia:. *Journal of Great Lakes, 42*(1), 146-149.

Browne, M. A., Galloway, T. S., & Thompson, R. C. (2007). Microplastic – an emerging contaminant of potential concern? *Integrated Environmental Assessment and Management, 3*, 559-561. doi:10.1002/ieam.5630030412

Browne, M. A., Galloway, T. S., & Thompson, R. C. (2010). Spatial patterns of plastic debris along estuarine shorelines. *Environmental Science & Technology, 44*, 3404-3409. doi:10.1021/es903784e

Browne, M., Crump, P., Niven, S., Teuten, E., Tonkin, A., Galloway, T., & Thompson, R. (2011). Accumulation of microplastic on shorelines worldwide: sources and sinks. *Environmental Science & Technology*(45), 9175-9179.

Browne, M., Niven, S., Galloway, T., Rowland, S., & Thompson, R. (2013). Thompson, R.C., 2013. Microplastic moves pollutants and additives to worms, reducing functions linked to health and biodiversity. *Current Biology, 23*(23), 2388-2392.

Carpenter, E., & Smith Jr, K. (1972). Plastics on the Sargasso Sea surface. *Science, 175*, 1240-1241.

Cincinelli, A., Scopetani, C., Chelazzi, D., Lombardini, E., Martellini, T., Katsoyiannis, A., . . . Corsolini, S. (2017, May). Microplastic in the surface waters of the Ross Sea

(Antarctica): Occurrence, distribution and characterization by FTIR. *Chemosphere, 175*, 391-400. doi:10.1016/j.chemosphere.2017.02.024

Cole, M., Lindeque, P., Halsband, C., & Galloway, T. (2011). Microplastics as contaminants in the marine environment: a review. *Marine Pollution Bulletin, 62*, 2588-2597. Retrieved from http://dx.doi.org/10.1016/j.marpolbul.2011.09.025.

D'Amelia, R. P., Gentile, S., Nirode, W. F., & Huang, L. (2016). Quantitative Analysis of Copolymers and Blends of Polyvinyl Acetate (PVAc) Using Fourier Transform Infreared Spectroscopy (FTIR) and Elemental Analysis (EA). *World Journal of Chemical Education, 4*(2), 25-31. doi:10.12691/wjce-4-2-1

Eriksen, M., Lebreton, L. C., Carson, H. S., Thiel, M., Moore, C. J., Borerro, J. C., . . . Reisser, J. (2014). Plastic Pollution in the World's Oceans: More than 5 Trillion Plastic Pieces Weighing over 250,000 Tons Afloat at Sea. *PLoS ONE, 9*(12).

Eriksen, M., Mason, S., Wilson, S. B., Zellers, A., Edwards, W., Farley, H., & Amato, S. (2013). Microplastic pollution in the surface waters of the Laurentian Great Lakes. *Marine Pollution Bulletin, 77*(1-2), 177-182.

Fendall, L. S., & Sewell, M. A. (2009). Contributing to marine pollution by washing your face: Microplastics in facial cleansers. *Marine Pollution Bulletin, 58*, 1225-1228. doi:10.1016/j.marpolbul.2009.04.025

Free, C., Jensen, O., Mason, S., Erikson, M., Williamson, N., & Boldgiv, B. (2014). High-levels of microplastic pollution in a large, remote, mountain lake. *Marine Pollution Bulletin, 85*(1), 156-163.

Fries, E., Dekiff, J. H., Willmeyer, J., Nuelle, M.-T., Ebert, M., & Remy, D. (2013, Oct). Identification of polymer types and additives in marine microplastic particles using pyrolysis-GC/MS and scanning electron microscopy. *Environmental science, Processes & Impacts, 15*(10), 1949-56. doi:10.1039/c3em00214d

Geyer, R. (2020). Chapter 2 - Production, use, and fate of synthetic polymers. (T. M. Letcher, Ed.) *Plastic Waste and Recycling*, 13-32.

Geyer, R., Jambeck, J. R., & Law, K. L. (2017). Production use, and fate of all plastics ever made. *Science Advances, 3*(7), e1700782. doi:10.1126/sciadv.1700782

Gregory, M. (1978). Accumulation and distribution of virgin plastic granules on New Zealand beaches. *New Zealand Journal of Marine and Freshwater Research, 12*(4), 399-414.

Gregory, M. (1996). Plastic 'Scrubbers' in Hand Cleansers: a further (and minor) source for marine pollution identified. *Marine Pollution Bulletin, 32*(12), 867-871.

Hill, L. E. (1978, December). Social and Economics: One Perspective:. *Review of Social Economy*.

Imhof, H., Ivleva, N., Schmid, J., Niessner, R., & Laforsch, C. (2013). Contamination of beach sediments of a subalpine lake with microplastic particles. *Curr. Biology, 23*(19), R867-R868. Retrieved from http://dx.doi.org/10.1016/j.cub.2013.09.001

KNBS. (2019). *Volume IV: Distribution of Population by Socio-Economic Characteristics.* Retrieved from http://www.knbs.or.ke/?wpdmpro=2019-kenya-population-and-housing-census-volume-iv-distribution-of-population-by-socio-economic-characteristics>

Larkin, P. (2011). *Infrared and Raman Spectroscopy: Principles and Spectral Interpretations.* Waltham, MA: Elsevier.

Law, K., & Thompson, R. (2014). Oceans. Microplastic in the seas. *Science, 345*(6193), 144-145. doi:10.1126/science.1254065

Mansur, H. S., Sadahira, C. M., Souza, A. N., & Mansur, A. (2008). FTIR spectroscopy characterization of poly(vinyl alchol) hydrogel with different hydrolysis degree and chemically crosslinked with glutaraldehyde. *Material Science and Engineering C, 28*(4), 539-548. doi:10.1016/j.msec.2007.10.088

Masura, J., Baker, J., Foster, G., Arthur, C., & Herring, C. (2015). *Laboratory methods for the analysis of microplastics in marine environment: recommendations for quanitfying synthetic particles in waters and sediments.* Silver Spring, MD (USA): NOAA Technical Memorandum NOS-OR&R-48.

Meijer, L. J., van Emmerik, T., van der Ent, R., Schmidt, C., & Lebreton, L. (2021). More than 1000 rivers account for 80% of global riverine plastic emiisions into the oceans. *Science Advances, 7*(18). doi:10.1126/sciadv.aaz5803

Mitullah, W. (2003). Street trade in Kenya: The contribution of research in policy dialogue and response. doi:10.3362/9781780446325.013

Moore, C. (2008). Synthetic polymers in the marine environment: a rapidly increasing, long-term threat. *Environmental Research, 108*(2), 131-139.

Moore, C., Lattin, G., & Zellers, A. (2011). Quantity and type of plastic debris flowing from two urban rivers to coastal waters and beaches of Southern California. *Journal of Integrated Coastal Zone Management, 11*(1), 65-73.

Murphy, F., Ewins, C., Carbonnier, F., & Quinn, B. (2016). Wastewater treatment works (WwTW) as a source of microplastics in the aquatic environment. *Environment Science & Technology, 50*, 5800-5808.

Nairobi City Water and Sewerage Company [NCWSC]. (2021). *NCWSC*. Retrieved February 14, 2022, from https://www.nairobiwater.co.ke/

Ng, K., & Obdard, J. (2006). Prevalence of microplastics in Singapore's coastal marine environment. *Marine Pollution Bulletin, 52*(7), 761-767.

Njoroge, B., Kimani, M., & Ndunge, D. (2014). Review of Municipal Solid Waste Management: A Case Study of Nairobi, Kenya. *International Journal of Engineering and Science, 4*(2), 16-20.

Nyika, J. (2017). Situational analysis of Nairobi River Basin (NRB). *Water Practice & Technology, 12*(3).

Odhiambo, O. R., Musalagani, A. C., Lyanda, N. J., & Ruth, S. J. (2014, April). The Plastic Waste Menace in kenya: A Nairobi City Situation. *International Journal of Current Research, 6*(4), 6175-6179.

OECD. (2022a). *Global Plastics Outlook: Economic Drivers, Environmental Impacts and Policy Options.* Paris: OECD Publishing.

OECD. (2022). *Global Plastics Outlook: Policy Scenarios to 2060.* Paris: OECD Publishing. Retrieved from .oecd-ilibrary.org/: https://www.oecd-ilibrary.org/

Paruta, P., Bouchet, A., Boucher, J., Dubois, L., Manyara, P., Sorrentino, L., . . . Magaud, V. (2020). *Final Report for Kenya [PowerPoint slides]. IUCN, UNEP, Life Cycle Initiative.* Ministry of Environment and Forestry, NEMA. IUCN, UNEP.

Rajakumar, K., Sarasvathy, V., Chelvan, A., Chitra, R., & Vijayakumar, C. (2009). Natural riddel

Sanchez, W., Bender, C., & Porcher, J. (2014). Wild gudgeons (Gobio gobio) from French rivers are contaminated by microplastics: preliminary study and first evidence. *Environmental Research, 128*, 98-100.

Simon, M., van Alst, N., & Vollersten, J. (2018). Quantification of microplastic mass and removal rates at wastewater treatment plants applying Focal Plane Array (FPA)-based Fourier Transform Infrared (FT-IR) imaging. *Water Research*, 1-9.

Tagg, A. S., Sapp, M., Harrison, J. P., & Ojeda, J. J. (2015). Identification and Quantification of Microplastics in Wastewater Using Focal Plane Array-Based Reflectance Micro-FT-IR-Imaging. *Analytical Chemistry*, 6032-6040.

Talvitie, J., Heinonen, M., Paakkonen, J.-P., Vahtera, E., Mikola, A., Setala, O., & Vahala, R. (2015). Do wastewater treatment plants act as a potential point source of microplastics? Preliminary study in the coastal Gulf of Finland, Baltic Sea. *Water Science and Technology, 72*(9), 1495-504. doi:10.2166/wst.2015.360.

Thompson, R. C., Olsen, Y., Mitchell, R. P., Davis, A., Rowland, S., John, A., . . . Russell, A. (2004). Lost at sea: whereis all the plastic? *Science, 310*, 1117.

UNEP. (2014). *Valuing Plastics: The Business Case for Measuring, Managing and Disclosing Plastic Use in the Consumer Goods Industry.* United Nations Environment Programme (UNEP).

UNEP. (2018). *Single-use Plastics: A Roadmap for Sustainability (Rev2).* Retrieved from https://wedocs.unep.org/20.500.11822/25496.

Workman, J. (2001). *Handbook of Organic Compounds NIR, IR, Raman, and UV-Vis Spectra Featuring Polymers and Surfactants, 3 Volume Set: Methods and Interpretations, UV-Vis*

Wright, S. L., Thompson, R. C., & Galloway, T. S. (2013). *Environmental Pollution, 178*, 483-492.

Zbyszewski, M., & Corcoran, P. (2011). Distribution and Degradation of Fresh Water Plastic Particles Along the Beaches of Lake Huron, Canada. *Water, Air, & Soil Pollution, 20*, 365-372. doi:10.1007/s11270-011-0760-6

Zulu, E. M., Beguy, D., Ezech, A. C., Bocquier, P., Madise, N. J., Cleland, J., & Falkingham, J. (2011). Overview of migration, poverty and health dynamics in Nairobi City's slum settlements. *Journal of Urban Health: Bulletin of the New York Academy of Medicine, 88*. doi:10.1007/s11524-011-9595-0

Editorial Committee

Editorial Board

INSTRUCTIONS TO CONTRIBUTORS

The editorial staff of the AJERI requests contributors of articles for publication to observe the following editorial policy and guidelines accessible at https://www.iekenya.org/ in order to improve communication and to facilitate the editorial process.

Criteria for Article Selection

Priority in the selection of articles for publication is that the articles:

a. Are written in the English language
b. Are relevant to the application relevant of engineering and technology research and Innovation
c. Have not been previously published elsewhere, or, if previously published are supported by a copyright permission
d. Deals with theoretical, practical and adoptable innovations applicable to engineering and technology
e. Have a 150 to 250 words abstract, preceding the main body of the article
f. The abstract should be followed by a list of 4 to 8 "key Words"
g. Manuscript should be single-spaced under 4,000 words (approximately equivalent to 5-6 pages of A4-size paper)
h. Are supported by authentic sources, references or bibliography

Rejected/Accepted Articles

a. As a rule, articles that are not chosen for AJERI publication are not returned unless writer (s) asks for their return and are covered with adequate postage stamps. At the earliest time possible, the writer (s) is advised whether the article is rejected or accepted.
b. When an article is accepted and requires revision/modification, the details will be indicated in the return reply from the AJERI Editor, in which case such revision/modification must be completed and returned to AJERI within three months from the date of receipt from the Editorial Staff.
c. Complementary copies: Following the publishing, three successive issues are sent to the author(s)

Procedure for Submission

a. Articles for publication must be sent to AJERI on the following address:

The Editor

African Journal of Engineering Research and Innovation

P.O Box 41346- 00100

City Square Nairobi Kenya

Tel: +254 (20) 2729326, 0721 729363, (020) 2716922

E-mail: editor@iekenya.org

b. The article must bear the writer (s) name, title/designation, office/organization, nationality and complete mailing address. In addition, contributors with e-mail addresses are requested to forward the same to the Editor for faster communication.

For any queries, authors are requested to contact by mail (editor@iekenya.org).

PUBLISHER

The *Institution of Engineers of Kenya*

P.O Box 41346- 00100

City Square Nairobi Kenya

Tel: +254 (20) 2729326, 0721 729363, (020) 2716922

Email: editor@iekenya.org

Website: www.iekenya.org

CONTENTS **Pages**